GeoArabia, vol. 13, no. 4, 2008, p. 113-160
Gulf PetroLink, Bahrain

Application of Thomeer Hyperbolas to decode the pore systems, facies and reservoir properties of the Upper Jurassic Arab D Limestone, Ghawar field, Saudi Arabia: A "Rosetta Stone" approach

Edward A. Clerke, Harry W. Mueller III, Eugene Craig Phillips, Ramsin Y. Eyvazzadeh, David H. Jones, Raghu Ramamoorthy and Ashok Srivastava

ABSTRACT

We investigated the basic geological and petrophysical properties of the multimodal pore systems in the Arab D limestone facies in Ghawar field, Saudi Arabia. The study used more than 500 mercury injection capillary pressure (MICP) data, which were type-curve matched using Thomeer Hyperbolas. The new MICP sample data were drawn from 10 cored wells that transect the Ghawar field from north to south and from a previous fieldwide study with 125 MICP samples. These 500 samples have a very rich statistical foundation in that they were selected using only random decimation within each of the facies from more than 3,500 core plugs all with assigned facies. In addition to MICP data and facies, a former, smaller sample set had both facies and Dunham texture codes. A new view of these pore systems emerged, that is built upon the intrinsic, fundamental and separate maximum pore-throat diameter modal elements named *porositons*. Porositons are stable, recurring and intrinsic modes in the maximum pore-throat diameter of the carbonate pore systems. Analytical results derived from the MICP data showed that the pore systems of the Arab D limestones can be classified based on porositons. The benefits of this new classification are demonstrated by considering in detail the relationships to geological facies, well-log responses, permeability modeling and simple nuclear magnetic resonance (NMR) well-log response. By analogy to the decoding of the Egyptian hieroglyphics using the Rosetta Stone, the use of porositons enables strong connections to be made between the geological facies, petrophysical and reservoir-flow properties of these complex carbonate rocks. The relationships between the new pore systems categories and the facies were thoroughly tested using north-south field trends.

INTRODUCTION

Understanding pore systems is essential for modeling the properties and performance of hydrocarbon reservoirs. Pore systems provide the primary control on hydrocarbon distribution during reservoir charging. They control the interaction of the rock with fluids through wettability modification, and fundamentally control the hydrocarbon storage and recovery through the properties of porosity, permeability, relative permeability and microscopic-displacement efficiency. Pore systems can be examined in detail with core material and perhaps linked to well-log responses, but to fill the inter-well volumes of reservoir models with pore system properties, they must also be linked to predictive geological parameters. Thompson et al., (1987) in a portentous review of the pore geometrical problems of sedimentary rocks, noted "Prediction of rock properties, such as the transport properties of fluids in the pore space, and the elastic properties of the grain space, requires a set of statistics that embody the relevant physics"; and "More generally, the statistical description of pore geometry awaits definition of relevant statistics. This approach could ultimately tie the geology of rock formation to their reservoir properties, a tie with important consequences for oil exploration and production."

Multiple and complex pore systems are commonly encountered in carbonate reservoirs. Studies of the Arab D limestones in Ghawar field, Saudi Arabia (Figure 1), have demonstrated the presence and approximate volumes of multiple-porosity types as two-dimensional petrographic information (Cantrell and Hagerty, 1999, 2003; Hagerty and Cantrell, 1990 unpublished report). In this paper, we extract three-dimensional pore geometrical statistics that embody the relevant physics using results from Thomeer Hyperbola (Thomeer, 1960) analysis of mercury injection capillary pressure

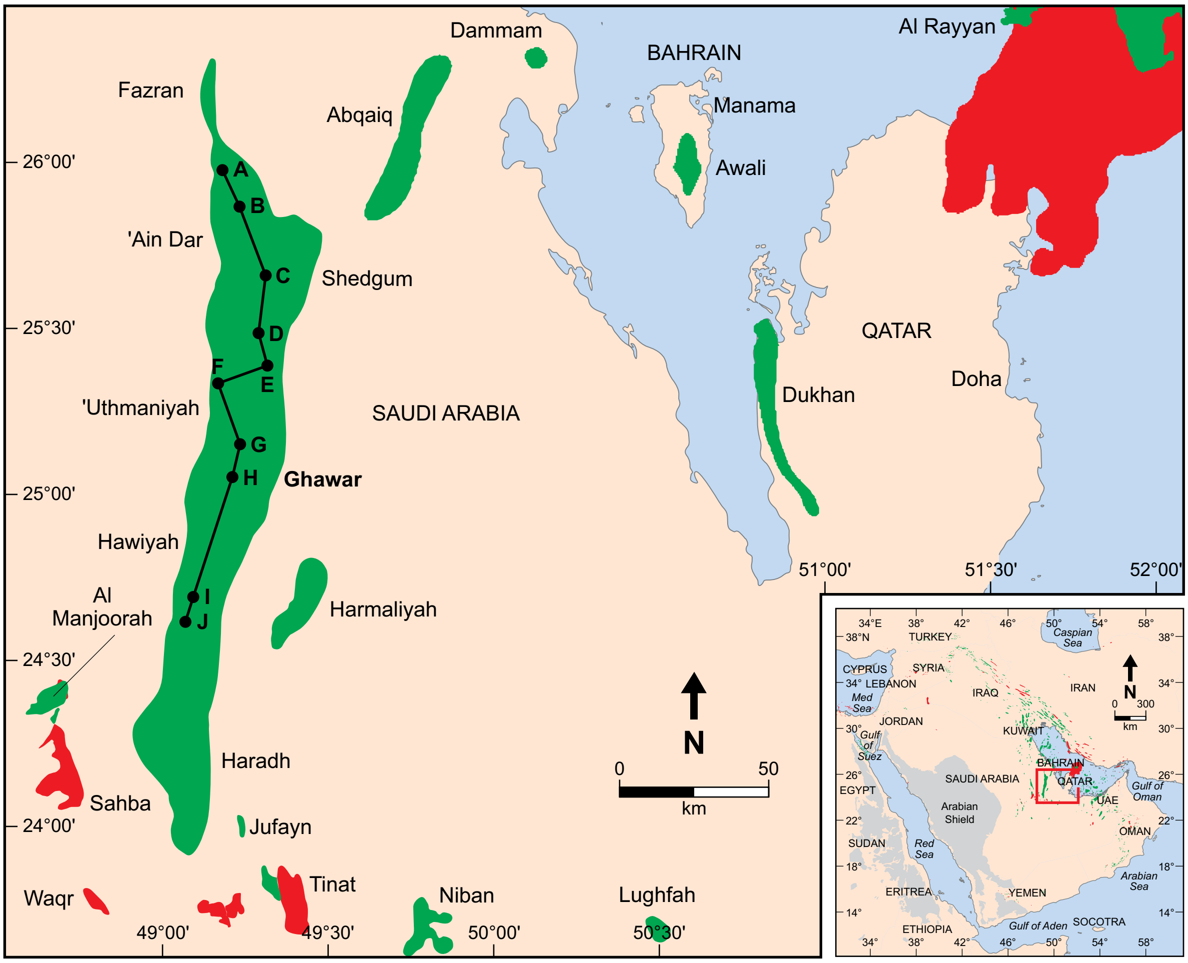

Figure 1: The Arab D limestone was sampled in ten cored wells located along a NS-transect of Ghawar field. The mercury injection capillary pressure (MICP) data base was selected using random decimation from an inventory of over 3,500 core plugs with assigned facies.

data (MICP; see Appendix 1 for a review of Thomeer analysis and comparison to similar techniques, e.g. Leverett J Function), conventional core analysis data (porosity and permeability) and qualitative analysis of nuclear magnetic resonance (NMR).

The aspects of the pore system we extract are:

(1) Pore-subsystem volume, which has a counterpart in the size-differentiated, point-count data;

(2) Pore-subsystem geometrical factor, which has a counterpart in the sorting coefficient or size-distribution width of the size-differentiated point-count data;

(3) Maximum diameter of the pore-throat that controls the pore subsystem. This is only determined by Thomeer analysis of MICP data, and only has a weakly defined petrographic counterpart. This diameter value, however, plays a fundamental role in a new pore-system classification scheme, allows the pore-subsystems to be related to height above free-water level in the reservoir (effectiveness) and controls the permeability.

The results that emerge from our analysis intersect several petroleum reservoir disciplines and, more explicitly, allow us to relate their subsurface languages. Our approach is similar to the translation-triangle applied to the decoding of Egyptian hieroglyphs using the Rosetta Stone. This paper focuses on the subsurface languages involving Arab D static reservoir properties: depositional facies, well-log responses and the pore systems. Other translations involve the dynamic properties of permeability, relative permeability and microscopic-displacement efficiency and speak to a petrophysical and reservoir engineering audience. These have been published in the engineering literature (Clerke, 2007).

The paper begins with some general information about the Ghawar field and previous geological studies of Arab D facies and carbonate microporosity. Our analysis is focused on limestones and does not include dolomitic facies, nor do we consider the important role of fracture porosity and permeability. We then introduce the statistics of the maximum pore-throat diameter to characterize the multimodal Arab D limestone facies. We discuss density-neutron measurements, porosity and permeability as related to multimodal limestone pore systems. Using only basics of NMR signal analysis, we demonstrate an alignment of the behavior of maximum pore-throat diameter and NMR-detected pore-body diameters. We explore relationships between facies and porositons, and the calculation of permeability. Finally, we conclude that these new investigations create many new paths for improvements in the evaluation of complex carbonate reservoirs.

ACRONYMS, ABBREVIATIONS, TERMS AND DEFINITIONS

B_v Volume of mercury injected into a porous rock sample during the mercury injection experiment, expressed as a fraction of the total sample bulk volume (see Appendix 1).

$d_{throat,max}$ Diameter (microns) of the largest pore-throat in a sample containing multiple pore systems (Thomeer Hyperbolas) i.e. the largest of the largest.

Dunham textures: Carbonate fabric textural classification system separating grains and muds (Dunham, 1962).

G Pore geometrical factor, related to the uniformity of the pore-throat diameters (low G) or non-uniformity (high G) of the pore-throats.

MICP Mercury injection capillary pressure.

Mode Region or subdivision of a uniform space as defined by the relevant physics and or physical parameters. In this paper the pore system of the Arab D limestone was found to be multimodal (i.e pore-system modality) and its modality to be monomodal, bimodal, or trimodal.

NMR Nuclear magnetic resonance.

P_d Minimum entry pressure or the maximum pore-throat diameter for a system of pores and throats that are characterized by one Thomeer Hyperbola.

$P_{d.f}$ the minimum entry pressure for a sample containing multiple pore systems (Thomeer Hyperbolas), i.e. the minimum of the minimums.

Pore subsystem: A continuum of pore-throats and pore space characterized by one Thomeer Hyberbola and one maximum pore-throat diameter; the latter of which is a member of a Porositon.

Porobodon: A postulated mode in the NMR pore body spectrum that may be directly related to a Porositon**.**

Porositon: A distinct and separable frequency distribution of maximum pore-throat diameters, P_d, which has a Gaussian distribution in the Log(P_d) domain, i.e. a mode in the maximum pore-throat diameter space. In this paper the porosity of the Arab D limestone is characterized by the M Porositon (macroporosity) and Types 1, 2 and 3 Porositons (microporosity).

Thomeer Hyperbola: See Appendix 1 (Figures A1 and A2). The hyperbola is characterized by (1) P_d, the minimum entry pressure or the maximum pore-throat diameter; (2) the pore geometrical factor, G; and (3) B^{∞}, the pore volume in that particular Thomeer hyperbola.

PREVIOUS STUDIES OF CARBONATE POROSITY SYSTEMS

The super-giant Ghawar oil field of Saudi Arabia is a N-trending anticline that is 230 km long and approximately 30 km wide (Figure 1). The main reservoir is the carbonate part of the D Member of the Upper Jurassic Arab Formation (Powers, 1968). The Arab-D Member is the oldest of four carbonate – evaporite cycles (from bottom to top, Arab-D, Arab-C, Arab-B, and Arab-A with the overlying Hith Anhydrite), each stratigraphically comprising a lower carbonate unit and an upper evaporite unit of which the evaporite intervals dominated by anhydrite. The D Member carbonate consists of several scales of shallowing-upward cycles dominated by burrowed mudstones and wackestones in its lower part and transitioning to skeletal packstones and grainstones and, ultimately, ooid grainstones in the upper part.

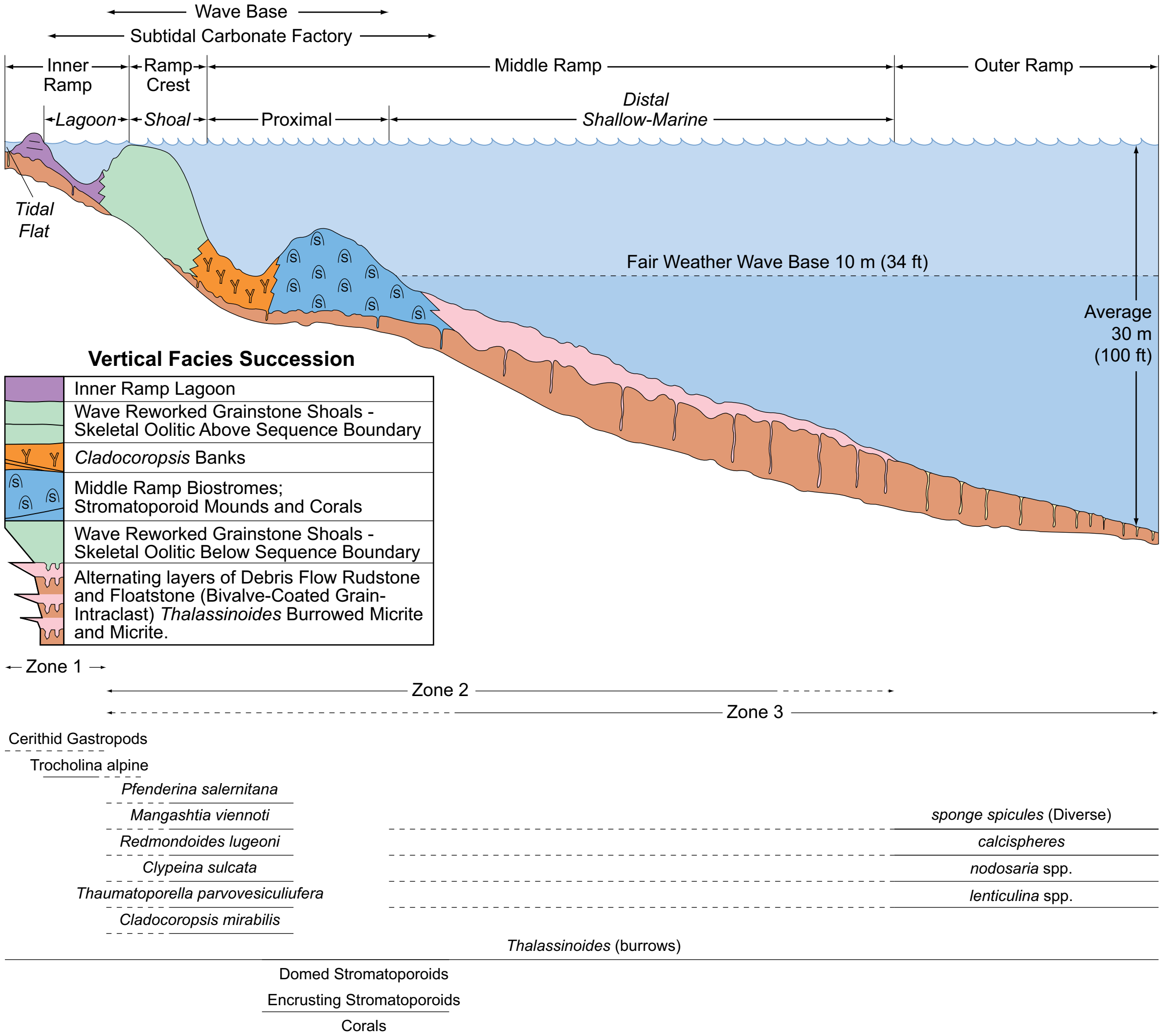

Figure 2: A single depositional cycle of the Arab D sediments that clearly identifies the main facies (Simplified after Lindsay et al., 2006). Readily identified facies within this cycle are the *Cladocoropsis*, Stromatoporoid-Red Algae-Coral, Bivalve-Coated Grain-Intraclasts (debris-flow deposits), Micrite and *Thalassinoides* Burrowed Micrite. Shoal deposits are associated with massive sands and oolitic (Skeletal Oolitic) facies in two positions in the total Arab D sedimentary column. When multiple depositional cycles are considered within the Ghawar Arab D section and sequence stratigraphy, a common simplified vertical facies succession emerges as the one shown on the lower left.

Many articles have been written on the super-giant Ghawar field, its geology and the performance of the Arab D Reservoir (e.g. Powers, 1968; Mitchell et al., 1988; Al-Husseini, 1997; Stenger et al., 2003; Figure 2 after Lindsay et al., 2006), but few have integrated its pore systems with the geology and reservoir performance. Moreover, although thousands of well logs, production surveys, cores and extensive production histories are available as data to characterize the Arab D Reservoir performance, the fundamental understanding of porosity and permeability and prediction of permeability remains a challenge.

With reference to the Ghawar field, Cantrell and Hagerty (1999, 2003) documented observations on the common presence of microporosity in the Arab Formation. They concluded: "Microporosity occurs throughout the Arab Formation of Saudi Arabia, and affects the log response, fluid-flow properties and ultimate recovery of hydrocarbons in these reservoirs." Their qualitative microporosity observations from petrographic data, were supported by displays of the pore-throat histograms from a sample subset on which MICP data were available (Figure 3, from Cantrell and Hagerty, 1999).

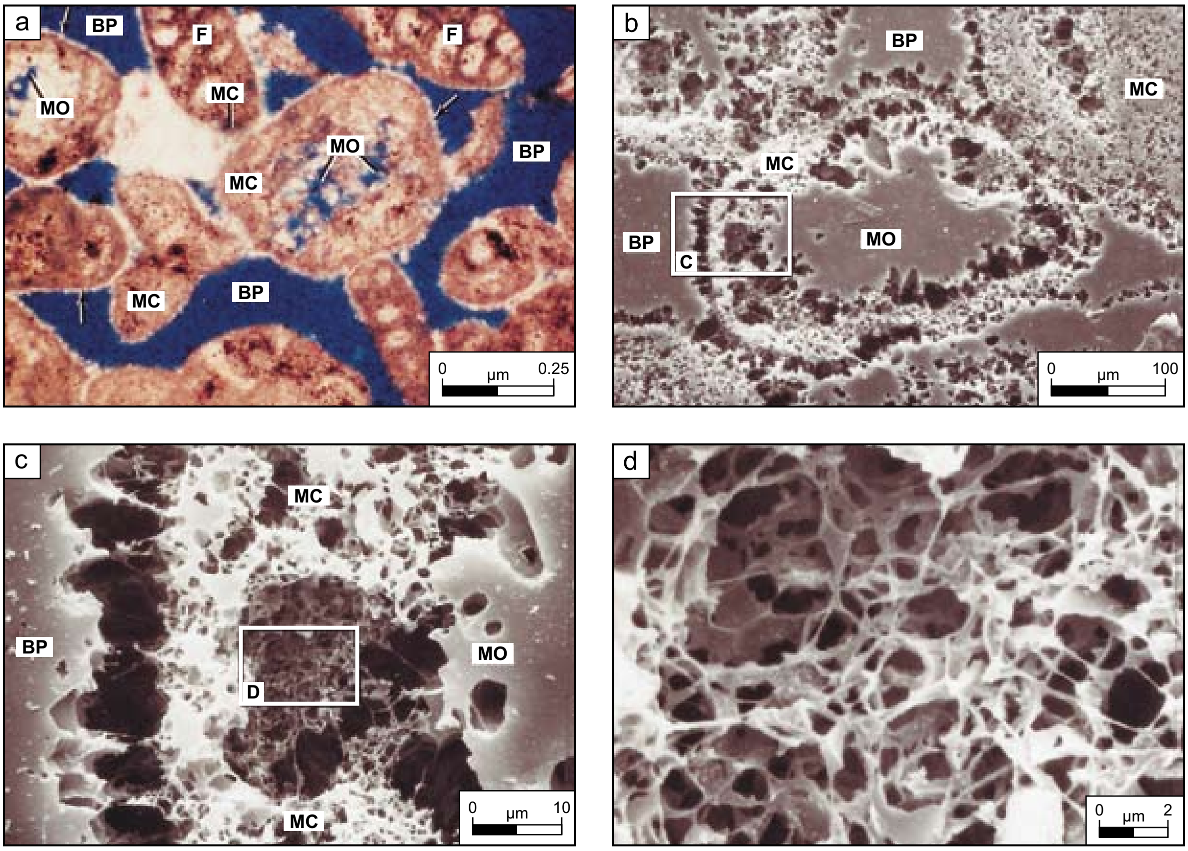

Figure 3: Microporosity petrographic images in Arab Formation carbonates (Cantrell and Hagerty, 1999). Porosity is filled by blue dye in the upper left image. The succeeding images are pore casts of increasingly higher magnification after removal of the carbonate matrix by acid. Image (a) shows abundant interparticle macroporosity (dark blue) as well as microporosity. The successive pore cast images of increasing magnification (b), (c), (d) show that the intraparticle microporosity is well-connected.

Early work on the presence of microporosity in carbonates by Herling (1968), contrasted the difference between carbonate and clastic sedimentary rocks. He noted, "The good correlation between specific surfaces calculated from grain-size distribution and measured with BET method (adsorption isotherm method of Brunauer et al., 1938) for quartz sands and powdered quartz is no longer valid for calcareous sands and silts." Pittman (1971) discussed one type of microporosity in carbonates as resulting from boring and perforating actions performed by blue-green algae into carbonate grains. A similar observation was made by Bathurst (1966) for skeletal sand grains of the Bimini lagoon.

Cantrell and Hagerty (2003) found four types of microporosity in the Arab D using an operational definition of microporosity as pores approximately 10 microns in diameter or less. Their four types of microporosity are: (1) microporous grains, (2) microporous matrix, (3) microporous fibrous to bladed cements, and (4) microporous equant cements, with microporous grains being the most volumetrically significant microporosity type. These authors stated, "Scanning Electron Microscope examination of pore casts and fractured rock surfaces reveals that a variety of skeletal and non-skeletal grain types are microporous. The microporosity–forming process transforms different grain types into grains that are similar with respect to their internal fabrics. Microporosity thus consists of a network of highly interconnected, uniform-sized straight tubular to laminar pore-throats that intersect with less elongate, more equant pores."

Mitchell et al. (1988) characterized the Arab D carbonates in terms of five limestone facies plus Dolomite: Skeletal-Oolitic, *Cladocoropsis*, Stromatoporoid–Red Algae–Coral, Bivalve-Coated Grain-Intraclast and Micrite. These facies represent a classification that utilizes fauna, assemblages of Dunham (1962) textures, major and minor grain types, sedimentary structures, pore types and diagenetic modification. A key result that emerges is that these facies subdivide the MICP data set by pore-system properties more clearly than other available facies descriptors. This establishes an important and previously nonexistent link between the depositional geology-facies and the pore systems, and hence the static and dynamic properties of the reservoir.

Clerke (2004) modified the limestone facies of Mitchell et al. (1988) and arrived at six facies (Figure 2, Appendix 2). In particular, he divided the skeletal-oolitic facies into those above and below an important sequence boundary identified in core descriptions by C.R. Handford (T. Keith, personal communication, 2001). His modification also separates-out the burrowed-micritic facies. In the present study, the Clerke (2004) classification is used unless otherwise indicated.

MODES AND POROSITONS: MAXIMUM PORE-THROAT DIAMETER STATISTICS

Thompson et al. (1987) discussed the many studies of pore networks "composed of pipes of widely varying sizes, which are distributed randomly along the links of the network"; and noted, "there are no experimental data to contradict the assumption of random distribution of pores." The data we have collected and present is likely the first and the most comprehensive data to show a deeper and non-random structure in the pore network parameters of the Arab D limestone.

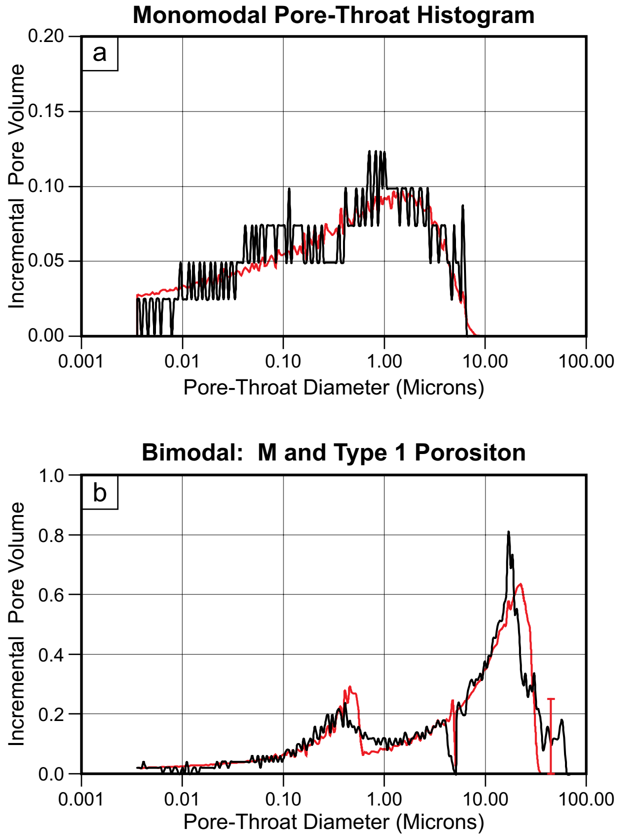

Figure 4: Histograms of pore-throat diameter from Arab D limestone MICP data along with the pore-throat diameter histogram from the Thomeer Hyperbolas (red) and closure correction (red bar); (a) pore-throat diameter histogram for a monomodal pore system; (b) pore-throat diameter histogram for a bimodal pore system.

Two data sets were used in the present study. The first consisted of 125 mercury injection capillary pressure (MICP) samples characterized by the textures of Dunham (1962) and the facies of Mitchell et al. (1988). This data set was compiled by Hagerty and Cantrell (1990, unpublished report) and quantitatively analyzed (Clerke, 2003, 2004; Clerke and Martin, 2004). It is dominated by packstone (Dunham, 1962), but otherwise contains a fairly uniform selection of other Dunham (1962) textures. The collection is also fairly uniform by facies except for undersampling of the *Cladocoropsis* facies.

Thomeer Hyperbolas (Thomeer, 1960) were fitted to this first MICP data set using computerized spreadsheets (Appendix 1; Clerke and Martin, 2004). This analysis first yields the number of Thomeer Hyperbolas – used here as equivalent to 'pore system' – required to fit the MICP data from each sample. We call this integer the *pore system modality*. Thirty-five percent of the samples required a single hyperbola (Figure 4a), 62% required two Thomeer Hyperbolas (Figure 4b) and 3% required three hyperbolas. To limit trivial occurrences of multiple pore-systems in one sample, we added to the Thomeer MICP-fitting process, the requirement that a volume of at least one unit of porosity be present for a significant second or a third pore system.

Table 1 shows the occurrence of the pore-system modality (number of Thomeer Hyperbolas required for each sample) for the Dunham (1962) textures. Key results are that mudstone is dominantly monomodal, while grainstones and mudlean packstones are dominantly bimodal; packstone and wackestone showed no definitive pore system modality. Table 2 shows the occurrence of the pore-system modality for the Mitchell et al. (1988) facies. Stromatoporoid-Red Algae-Coral and

Cladocoropsis are almost always bimodal. Note also the presence of 60–40 or 70–30 splits for Skeletal-Oolitic, Micrite, Dolomite and Bivalve-Coated Grain-Intraclast. Table 3 shows the pore-system modality when the Skeletal-Oolitic facies are distinguished into above-and-below the sequence boundary (Figure 2; Clerke, 2004) and the value of this split will be evident later when microporosity types are defined.

The second data set (Rosetta Stone Data) used 10 cored and described wells with full conventional well-log suites in a NS-transect across the Ghawar field (Figure 1). All of the core plugs (approximately 3,500) from these 10 wells were cataloged by the facies of Mitchell et al. (1988). Then seven to nine samples from each facies per well were selected at random to give 90 samples per facies, thus resulting in a uniform sample density for each facies. MICP experiments and analysis was conducted on these samples and the resulting data set was combined with the 125 samples of Hagerty and Cantrell (1990, unpublished report) as listed in Appendix 3.

The Thomeer Hyperbola analysis was then applied to the combined MICP data (Appendices 1 and 3) using computerized spreadsheets (Clerke and Martin, 2004). Thomeer parameter, P_d, when plotted on a logarithmic axis [Log(P_d) domain] showed the most significant variation, and it was considered the controlling parameter for classification. We observed four distinct and separable modes (Figure 5) and fitted each with a Gaussian distribution, termed a Porositon.

Pore-size ranges and microporosity have been assigned many names and size scales (Choquette and Pray, 1970; Pittman, 1971; Cantrell and Hagerty, 1999). In contrast, Figure 5 shows that maximum pore-throat sizes of the pore systems have a few natural and distinct modes (four) and hence self-define its size-based classification. The Thomeer Hyperbola curve-matching tool is the only one which allows the microporosity volume and its largest controlling pore-throat to be quantified separately from other pore volumes.

POROSITON CLASSIFICATION

The four modes in the distribution of the maximum pore-throat diameters (Figure 5) correspond to one macroporosity (M Porositon) and three microporosity types (Type 1, 2 and 3 Porositons). The position of the four porositons is a property of the porous medium and not determined by *ad hoc* criteria. The term

Table 1

Dunham Textures	Number of Pore Systems (%)		
	1	2	3
Grainstone	6.0	88.0	6.0
Mudlean Packstone	4.0	96.0	0.0
Packstone	37.0	58.0	5.0
Wackestone	50.0	50.0	0.0
Mudstone	100.0	0.0	0.0

The 125 MICP data of Hagerty and Cantrell (1990, unpublished report), coded with multiple descriptive terms, were used to compare pore system modality to the Dunham (1962) textures. Grainstone and mud-lean packstone are dominantly bimodal. Packstone and wackestone can be either monomodal or bimodal but mudstone is monomodal. This is important information for translating geological descriptions into quantitative pore system models.

Table 2

Facies (Mitchell et al., 1988)	Number of Pore Systems (%)		
	1	2	3
Skeletal Oolitic	32.0	63.0	5.0
Cladocoropsis	0.0	100.0	0.0
Stromatoporoid-Red Algae-Coral	11.0	84.0	5.0
Bivalve-Coated Grain-Intraclast	28.0	69.0	3.0
Micrite	71.0	29.0	0.0
Dolomite	67.0	33.0	0.0

The 125 MICP data of Hagerty and Cantrell (1990, unpublished report), coded with multiple descriptive terms, were used to compare pore system modality to the facies of Mitchell et al. (1988). The Cladocoropsis and Stromatoporoid–Red Algae-Coral are commonly bimodal. Other facies are a mixture of bimodals and monomodals at roughly 70-30% and 30-70% proportions. The number of trimodal pore systems is few and below statistical significance for the small MICP data set but it is shown for completeness.

Table 3

Facies (This Study)	Number of Pore Systems (%)		
	1	2	3
Skeletal Oolitic Above Sequence Boundary	35.0	61.0	4.0
Cladocoropsis	0.0	100.0	0.0
Stromatoporoid-Red Algae-Coral	11.0	84.0	5.0
Skeletal Oolitic Below Sequence Boundary	27.0	67.0	6.0
Bivalve-Coated Grain-Intraclast	28.0	69.0	3.0
Micrite	71.0	29.0	0.0

The 125 MICP data of Hagerty and Cantrell (1990, unpublished report), coded with multiple descriptive terms, were updated to split the Skeletal Oolitic facies into two subunits, above-and-below the sequence boundary (Clerke, 2004). No net improvement results from the statistical breakout at this stage, but later figures will show that the microporosity type in the Skeletal Oolitic facies are different when split.

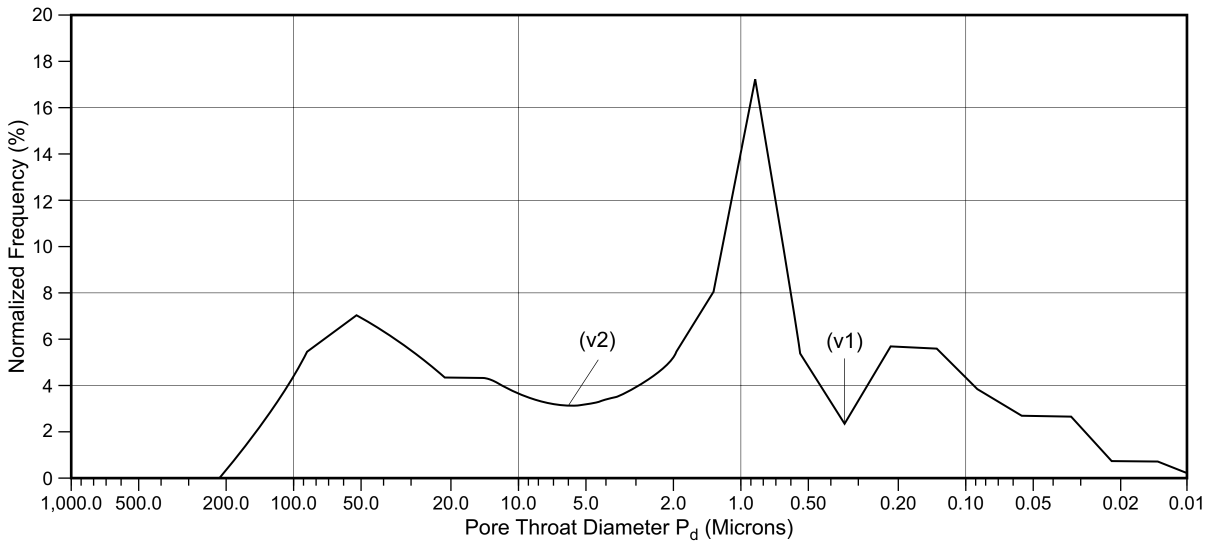

Figure 5a: Histogram of P_d values (converted to maximum pore-throat diameter [microns]) used for all Thomeer Hyperbolas is shown here. 860 hyperbolas were required to fit 454 samples from 10 wells. The data shows four distinct and separate modes, a broad mode on the left of large pore-throat diameters, a narrow and highly populated second mode at about 1 micron, and two less-frequent successive modes near 0.2 microns and 0.04 microns. The valley at 2% and 0.35 microns is very distinct (v1). Another less distinct valley is at about 6 microns (v2). The non-uniform spectrum suggests that maximum pore-throat diameters are related to an underlying discrete process. An alternate presentation of this data when weighted by the bin average porosity is shown in Figure 24, the valleys are still strongly present.

"microporosity" is used here in the sense of Swanson, (1985). "Micropores in reservoir rocks are defined as pores whose dimensions are significantly smaller than those contributing to the rock's permeability". Later sections of this paper and other publications (Clerke, 2007; Buiting and Clerke, in preparation) support this naming convention by demonstrating the lack of contribution of the micropores to the measureable permeability when the M Porositon occurs, i.e. macroporosity.

Results from the fitting of the data to Gaussian distributions are shown in Table 4. The distribution parameters for the four porositons are: mean, width (standard deviation) and the best Log(P_d) cutoff parameter separating the distributions. Notice from Table 4 that the bulk of the porosity on the average is carried in the M Porositon (17.1 pu) followed by the Type 1 Porositon (5.57 pu) and finally by Types 2 and 3 (2.22 pu) Porositons. The computed Thomeer permeability for the mean values is shown (see Appendix 1 for permeability calculation). The mean Thomeer pore geometrical factor, G, ranges from 0.51 to 0.13, with the highest values (widest distribution and poorest sorting) in the M Porositon (0.51 $\pm$ 0.19). The characterization of carbonate "heterogeneity" is captured by the width of the M Porositon and by the amount of multimodality present in the pore systems.

Core Plug Porosity and Permeability, and Multimodality

In core plugs the pore systems of the Arab D limestone matrix are commonly bimodal and composed of a single instance of macroporosity and some amount and type of microporosity from one of three possible types (Clerke, 2004, 2007; Clerke and Mueller, 2006; Buiting, 2007; Buiting and Clerke, in preparation). We examined the trend of total plug porosity in the limestone samples as compared to the pore system modality. Figure 6 shows the modality of the maximum pore-throat diameter data with a red curve representing the rolling-window average of the data versus porosity. The data indicate that bimodality is common when the porosity exceeds 7 pu. Trimodal pore systems start to occur, along with bimodals, in the porosity range from 12 to 24 pu, and above 24 pu the systems are mostly bimodal. In Figure 7, the maximum pore-throat diameter modality is compared to core plug permeability data using the rolling average (red line). Two distinct ranges occur: (1) from 0.01 to 10 mD, which is both monomodal and bimodal in nearly equal proportions; and (2) above 10 mD, bimodality dominates with occasional trimodality.

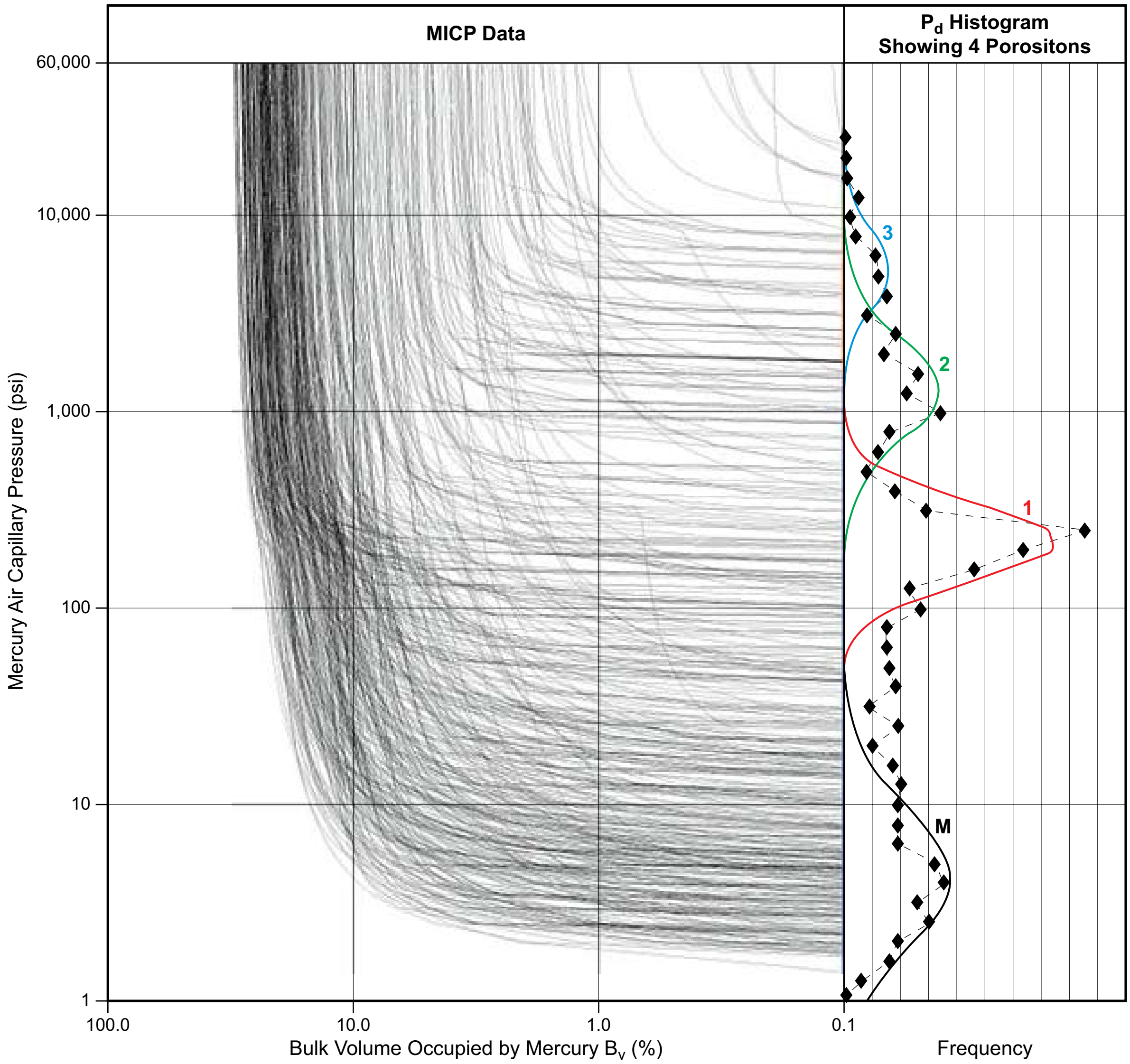

Figure 5b: Histogram of Figure 5a is shown (on the right) along with all of the graphical MICP data (on the left) after closure correction and Thomeer Hyperbola matching. Shown on the right is the frequency of occurrence of all P_d values for all Thomeer pore subsytems required (diamond shaped points connected with a faint dashed black line). This frequency is not simply the density of the number of lines to the left of the histogram because many of the pore systems exist primarily as subcomponents of a bimodal or trimodal capillary pressure curve. This is most strongly the case for Type 1 microporosity as it most commonly occurs as a second pore system in the M–1 configuration. The colored lines on the frequency histogram are the four fitted Gaussian distributions [porositons: M (black), 1 (red), 2 (green), 3 (blue)]. The Gaussian parameter values are compiled in Table 4. The conformance of the four Gaussian distributions to the experimental data is excellent (correlation R^2 of 0.85) except between about 40 and 90 psi where a plateau occurs.

Density-Neutron-Derived Porosity and Multimodality

In Figure 8, the plug maximum pore-throat diameter modality versus porosity data of Figure 6 is superimposed on the conventional density-neutron well-log crossplot using multi-well Arab D log data. The combination of density-neutron logs in a known limestone matrix might show some subtle evidence of maximum pore-throat diameter modality. The deviation of the data trend from the limestone line, as porosity increases, may be related to the increasing presence of dual-porosity systems through unknown effects such as flushing phenomena and/or flushed-zone, residual-oil saturation. Porosity, determined from these two porosity tools (density-neutron), appears to only

Table 4

Ghawar Arab D Limestone Porositon Parameters						
Gaussian Model	**Thomeer Parameters**					
	Log (P_d)	P_d (psi, Hg/air)	Pore-Throat Diameter (microns)	B_v (Porosity Unit)	G	Thomeer Permeability (mD)
Porositon M						
Mean	0.57	3.67	58.27	17.10	0.51	202.6
One Standard Deviation	0.53			8.36	0.19	
Porositon Separator Value	1.67	46.3	4.62			
Porositon 1						
Mean	2.31	204.0	1.05	5.57	0.15	0.036
One Standard Deviation	0.28			3.18	0.13	
Porositon Separator Value	2.79	617.0	0.35			
Porositon 2						
Mean	3.12	1,318.0	0.16	2.22	0.15	0.00014
One Standard Deviation	0.26			0.87	0.13	
Porositon Separator Value	3.40	2,512.0	0.09			
Porositon 3						
Mean	3.73	5,370.0	0.04	2.22	0.15	0.00001
One Standard Deviation	0.20			0.87	0.13	
Porositon Separator Value	4.78	60,000.0	0.00			

Gaussian distribution parameters for the four porositons fit to the histogram (see Figure 5) of the full data set of Log(P_d) values (Appendix 3, this study). The parameters are the mean and standard deviation for each Gaussian distribution (see Figure 5). Values of P_d are in psi (Hg/air) or the equivalent Maximum Pore-Throat diameter in microns. The parameters of the fit of a Gaussian distribution to B_v and G are also displayed. A Thomeer permeability has been calculated using the mean Gaussian parameters for each porositon. Also shown is a separating value (cutoff) for each porositon.

weakly indicate the modality of the pore system. Hence, we observe that these "conventional" petrophysical data sets at most give minimal indication of multimodality. The characterization of multimodal pore systems in reservoir limestones will require new methods for full evaluation by well logs. Re-interpretation of existing (density-neutron) well-log suites even with core data and powerful reprocessing (e.g. neural nets and self-organizing maps) likely cannot begin to address this aspect of the evaluation.

Porositon Combinations

The porositon combination naming scheme for multimodal pore systems follows the MICP access order, i.e. it follows the order of increasing pressure or decreasing largest controlling pore-throat, i.e. M, 1, 2, 3. Hence a MICP trimodal pore systems can be described by the increasing P_d series: M–1–2, but not 2–M–1.

The major porositon combinations still exhibit order when viewed on the traditional porosity-permeability crossplot (Figure 9) shown here with an overlay of constant P_d using equation A3. Hard trends and clear clusters are not present but there are still definite patterns. The M–1 bimodals with their various proportions of macro- and microporosity occupy a large area in the upper right corner of the plot. Moving to the left and reducing porosity but retaining high permeability, we find the M–1–2 and M–2 pore systems with the additional presence of micrite associated micropores (2, 3). Trending down to the left from the M–1 cluster the Type 1 monomodals are intersected, then Type 1–2 and 1–3 bimodals and then at very low porosities and permeabilities, Type 2 and 3 monomodals associated with micrite.

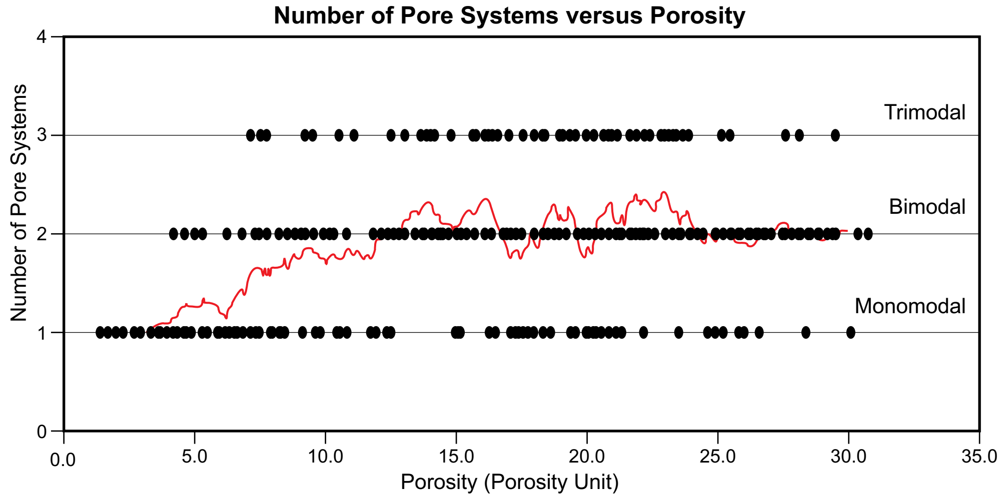

Figure 6: Maximum pore-throat diameter modality versus total porosity and a rolling average (red; average of the up-and-down rolling averages) indicates that bimodals are common above 7 pu, trimodal pore systems start to occur with the bimodals in the porosity range from 12 to 24 pu; above 24 pu the systems are with very minor exceptions, bimodal.

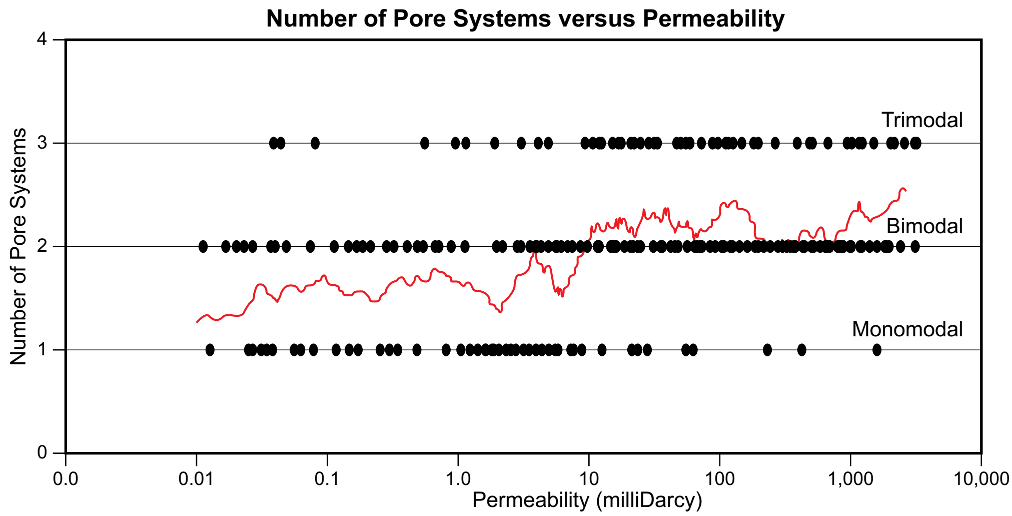

Figure 7: Maximum pore-throat diameter modality – permeability data and a rolling average (red; average of the up-and-down rolling averages) shows two distinct ranges: (1) from 0.01 to 10 mD, which is both monomodal and bimodal in nearly equal proportions; and (2) above 10 mD, bimodality dominates with occasional trimodality.

The results from Table 4 and the porositon combinations were used to build average porositon combination capillary pressure curves with uncertainties (Clerke, 2004). The measured capillary pressure curve data have been disassembled using the superposition capability of the Thomeer hyperbolas (see Appendix 1) followed by the porositon classification. The average capillary pressure curve for each porositon combination can similarly be reassembled using the averages and standard deviations of each porositon's Thomeer parameters and a forward superposition of the Thomeer hyperbolas. Figures 10 and 11 demonstrate the forward-modeled mercury capillary pressure curves for the major porositon combinations.

Facies and Porositon Combinations

In this section we examine the Arab D limestone pore systems and facies in terms of combinations of the four basic porositons. Two common combinations of macroporosity and the microporosity types are shown in pore-throat diameter histogram view (Figure 12). In the 125 sample data set of Hagerty and Cantrell (1990, unpublished report), we observed that the sequence boundary represents

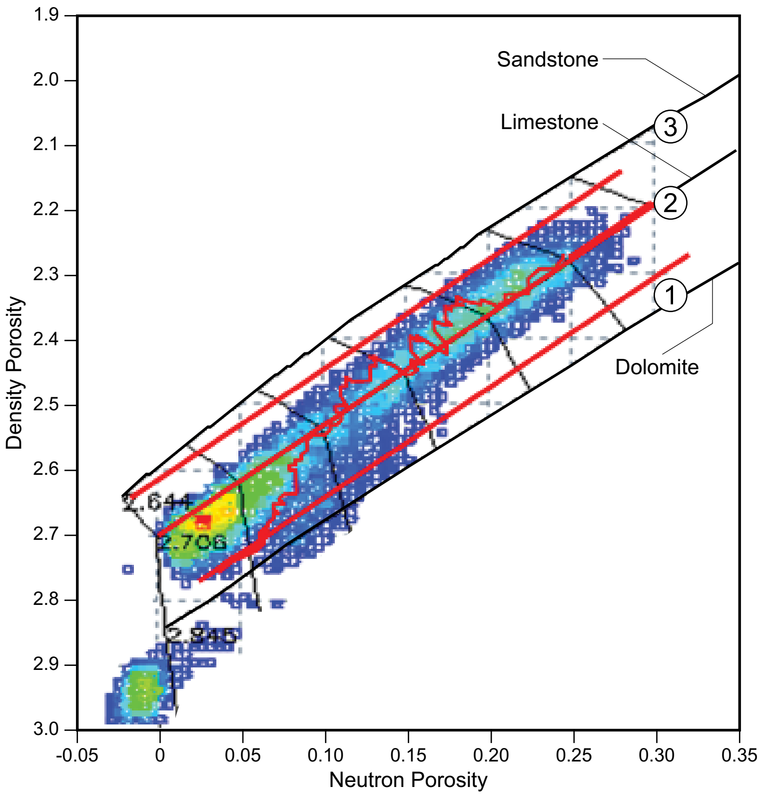

Figure 8: Maximum pore-throat diameter modality of Figure 6 is shown superimposed on a conventional density-neutron well-log crossplot using multi-well Arab D log data. The matrix porosity increases along the lithology trends from the lower left to the upper right. The tie lines (upper left to lower right) are lines of constant matrix porosity. The superimposed red lines from Figure 6 indicate porosity modality. Even with two porosity tools (density-neutron), porosity modality – if present at all – is only weakly manifested.

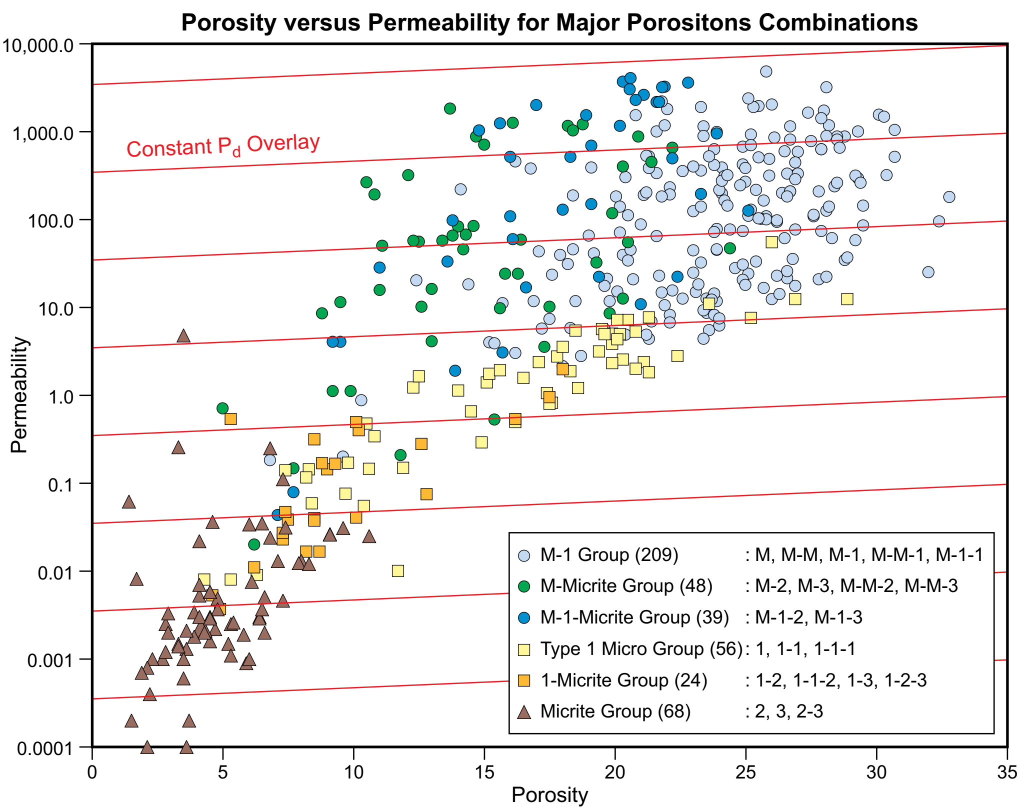

Figure 9: Petrophysical Rock Types (PRT) based on porositon combinations are shown on a conventional core data Permeability–Porosity crossplot. The six major PRTs still show order despite being based on a completely different classification scheme. An overlaying second red grid shows constant P_d (largest pore-throat diameter) as given by equation A3.

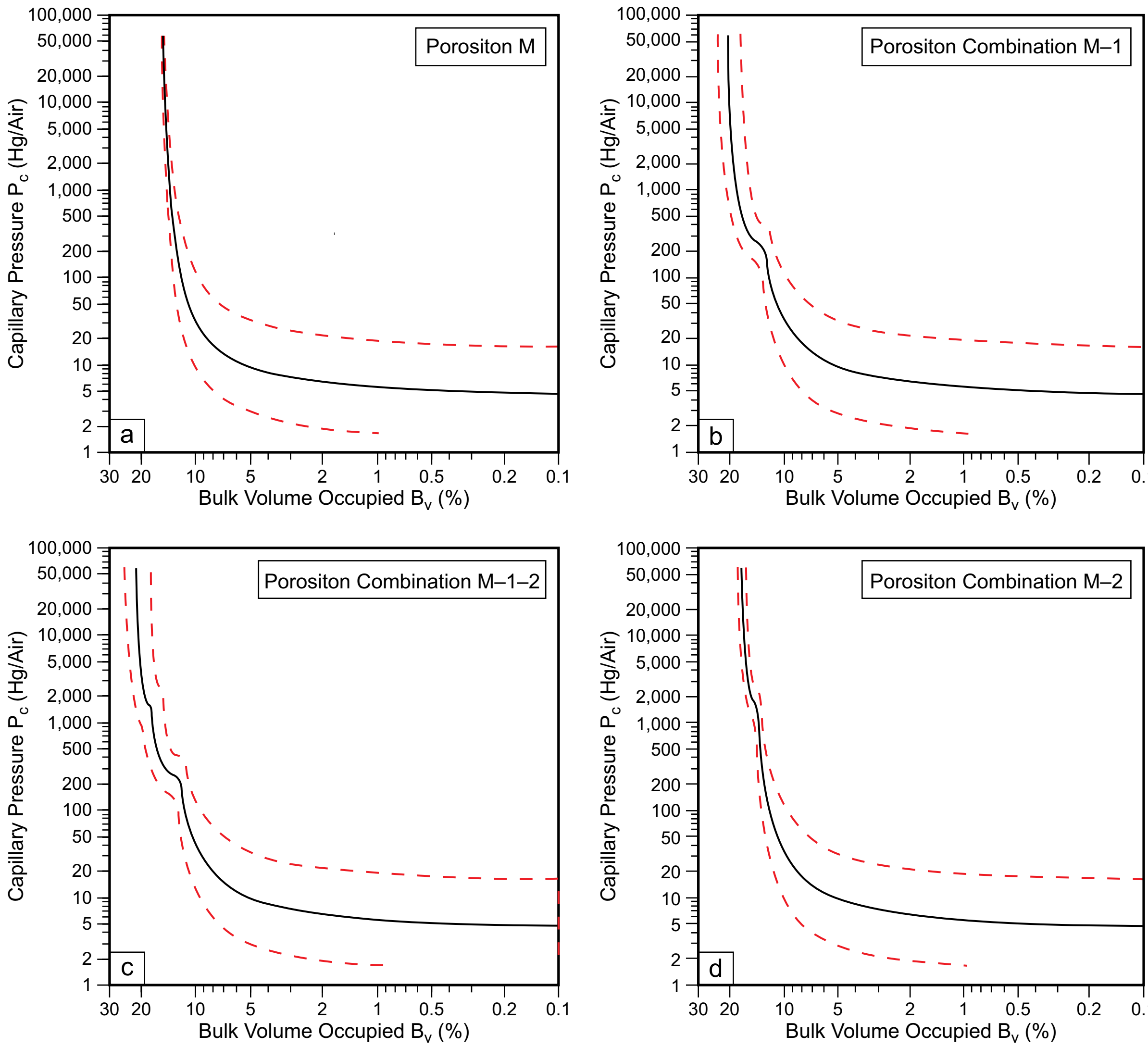

Figure 10: Forward modeled average capillary pressure curve with one standard deviation, using data from Table 4: (a) M Porositon, (b) Porositon combination M–1, (c) Porositon combination M–1–2, and (d) Porositon combination M–2.

a distinct facies break that is associated with the microporosity Types 1 and 2 (Table 5). The Skeletal Oolitic facies above-and-below the sequence boundary have completely different microporosity types (Figure 3). Above the sequence boundary, Skeletal Oolitic, *Cladocoropsis* and Stromatoporoid-Red Algae-Coral facies share the common occurrence of the Type 1 Porositon. The strong correlation of the microporosity types against the facies (Table 5) is in stark contrast with the weak correlation with Dunham (1962) textures (Figure 13). It is seen that grainstones can either contain Type 1 or 2 microporosity as can Mud-lean Packstone and Packstone. Wackestones contain only Type 2 microporosity. Thus facies descriptors (Clerke, 2004) contain the most petrophysical pore system information.

Figure 14 shows the nine significant porositon combinations with the occupancy frequency coded by the facies. These values are obtained after using a noise threshold cutoff of 5.2%, e.g. M, M–1, M–1–2, M–2, 1, 1–2, 1–3, 2, 3. The project's experimental design included multiple independent facies assignment cross-checks for all core plugs and thereby generated an internal facies error threshold of 5.2%.

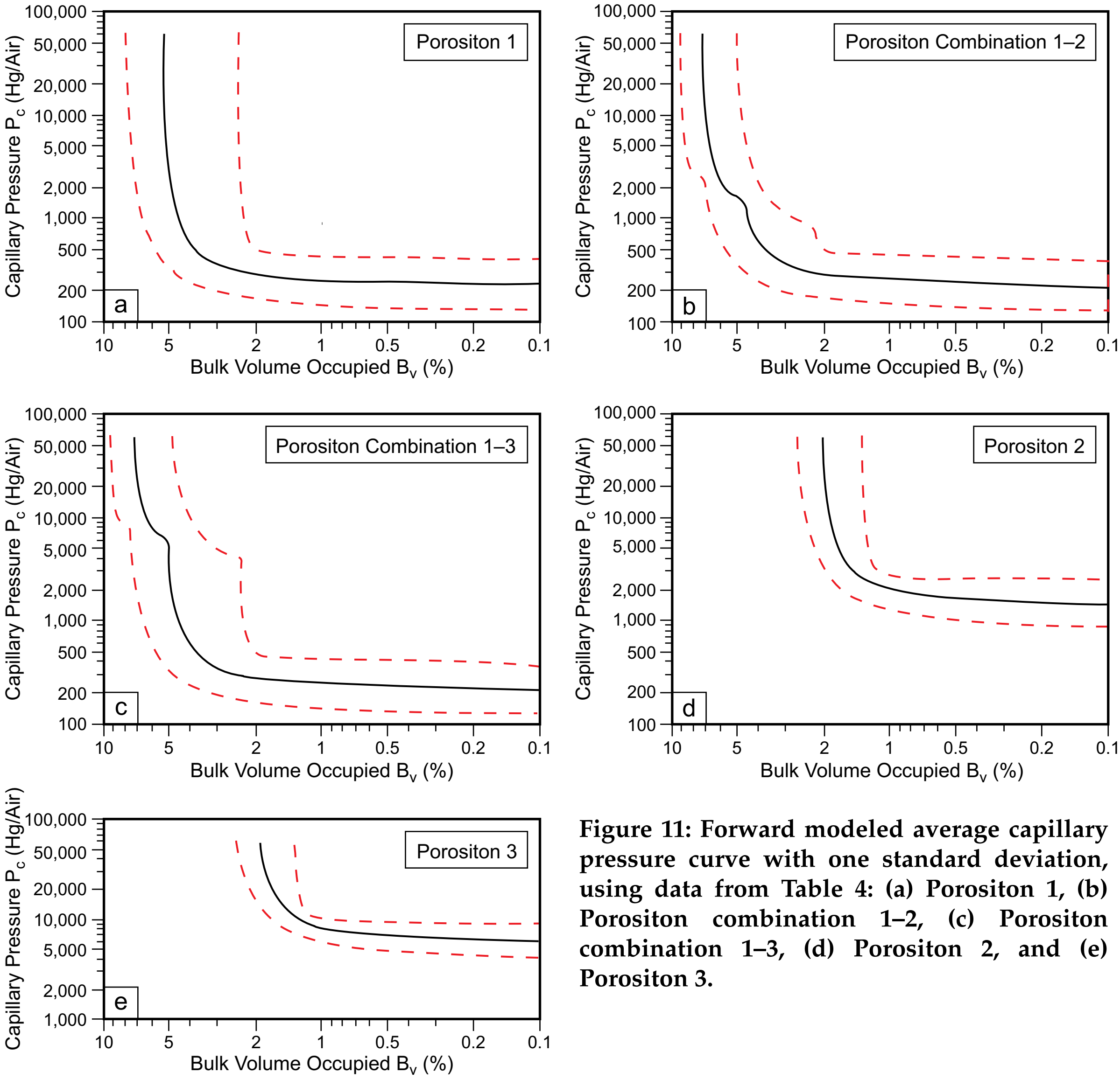

Figure 11: Forward modeled average capillary pressure curve with one standard deviation, using data from Table 4: (a) Porositon 1, (b) Porositon combination 1–2, (c) Porositon combination 1–3, (d) Porositon 2, and (e) Porositon 3.

Table 5

Dunham Textures	Microporosity Type (%)	
	1	2
Skeletal Oolitic Above Sequence Boundary	100.0	0.0
Cladocoropsis	100.0	0.0
Stromatoporoid-Red Algae-Coral	88.0	6.0
Skeletal Oolitic Below Sequence Boundary	10.0	90.0
Bivalve-Coated Grain-Intraclast	0.0	91.0
Micrite	too few samples	n.a.

The Skeletal Oolitic above-the-sequence boundary, Stromatoporoid-Red Algae-Coral and Cladocoropsis facies are very commonly bimodal and contain almost exclusively Type 1 microporosity. Skeletal Oolitic below-the-sequence boundary and Bivalve-Coated Grains-Intraclasts facies are bimodal and contain mostly Type 2 microporosity. The matrix elements do not sum to 100 for each facies because of the presence of an unclassified microporosity type, which is represented by only a few samples in the 125 MICP data set of Hagerty and Cantrell (1990, unpublished report). The third type of microporosity is isolated in the more voluminous data base from this study (Appendix 3).

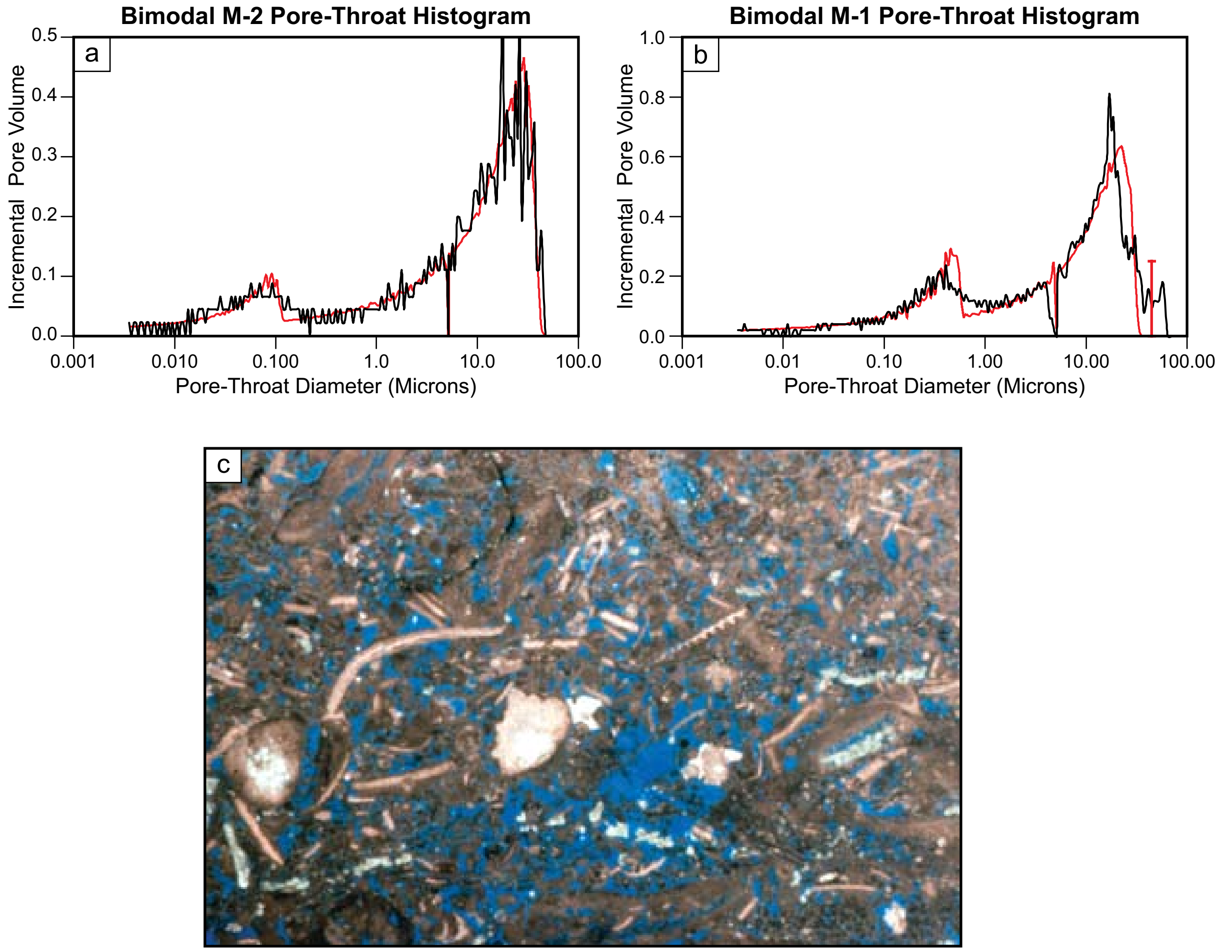

Figure 12: Pore-throat diameter histograms from Arab D limestone MICP data along with the pore-throat diameter histogram from the Thomeer Hyperbolas (red) and closure correction (red bar); (a) Bimodal pore system M–2; (b) Bimodal pore system M–1. Type 1 microporosity is associated with intraparticle microporosity as shown in Figure 3. Type 2 microporosity is associated with the presence of micrite. (c) Thin-section photomicrograph of an Arab D limestone sample exhibiting the M–2 porositon combination. The sample has abundant large pores and a large amount of micropores in the pervasive micrite.

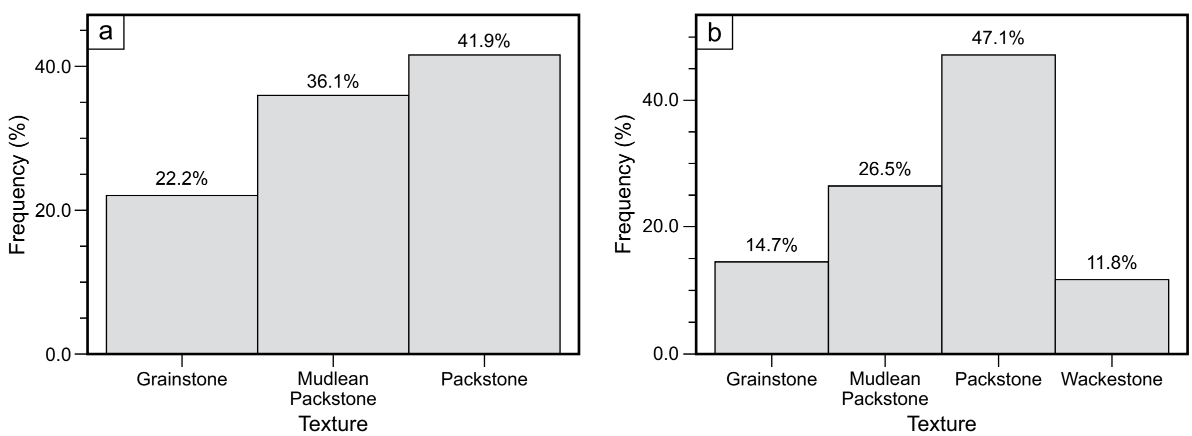

Figure 13: Data set of 125 MICP of Hagerty and Cantrell (1990, unpublished report) for Dunham (1962) textures showing frequency of occurrence: (a) Type 1 microporosity (intraparticle, 36 events); (b) Type 2 microporosity (Micritic, 34 events).

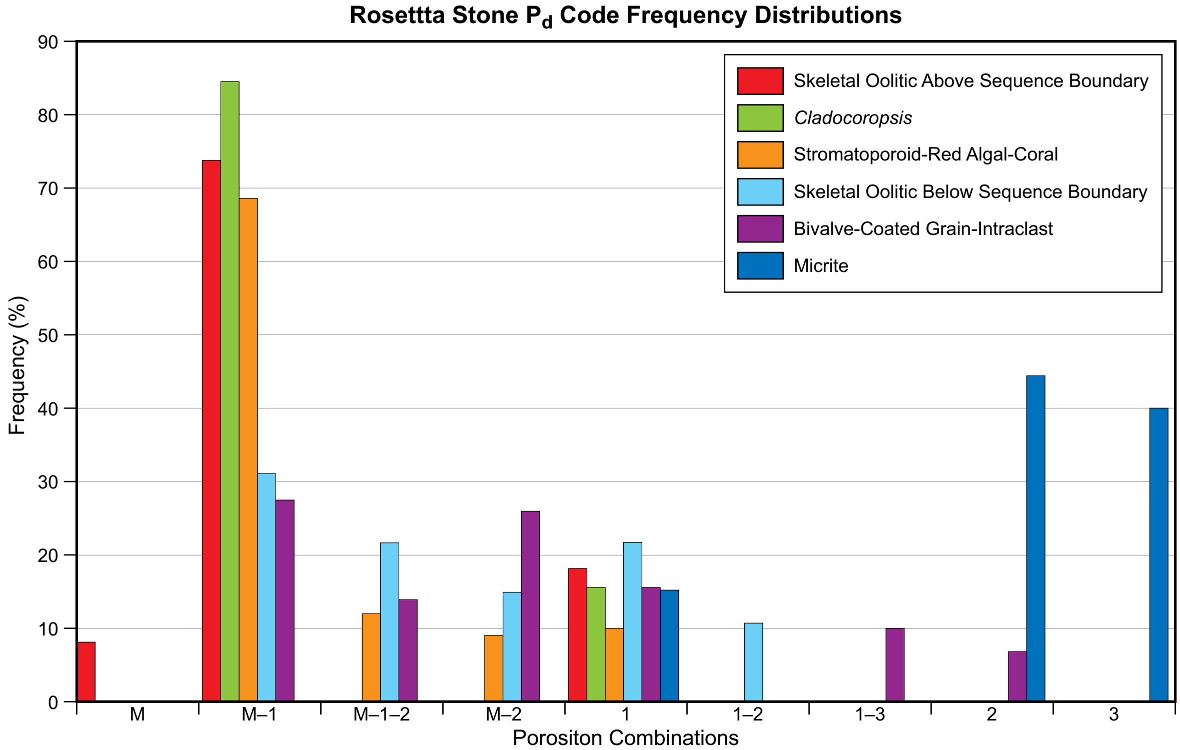

Figure 14: Six facies (modified by Clerke, 2004) are presented in terms of the nine major porositon combinations after being baseline-adjusted and renormalized for errors and noise at 5.2%. The Skeletal Oolitic above-the-sequence boundary, *Cladocoropsis* and Stromatoporoid–Red Algae-Coral facies are dominated by the M–1 porositon combination. Skeletal Oolitic below-the-sequence boundary and Bivalve-Coated Grains-Intraclasts have a large component of the M–1 porositon combination. Micrite is dominated by Type 2 and 3 Porositons.

Three of the facies tend to occur in the upper part of the reservoir interval (Skeletal Oolitic above-the-sequence boundary, *Cladocoropsis* and Stromatoporoid–Red Algae-Coral) and for these, only four porositon combinations are required with M–1 being dominant (Figure 14). Note that the monomodal, M, occurs only in the Skeletal Oolitic above-the-sequence boundary, and that the presence of Type 2 microporosity (Micrite associated) in the M–1–2 and M–2 is associated only with Stromatoporoid–Red Algae-Coral. An image of an M–1–2 Stromatoporoid–Red Algae-Coral trimodal core plug (Ahr et al., 2005) is shown (Figure 15) along with its MICP data and Thomeer fit, and the corresponding pore-throat presentation of the data and its fit.

For the facies occurring below-the-sequence boundary, a much more complicated situation occurs. The Skeletal Oolitic and Bivalve-Coated Grains-Intraclasts facies require five and six, respectively, of the nine porositon combinations (Figure 14). Similar in terms of their M–1 content, Bivalve-Coated Grains-Intraclasts contains 1–3 and 2, which do not occur in the skeletal oolitic facies, but which contains 1–2 not found in Bivalve-Coated Grains-Intraclasts. The Micrite facies is clearly dominated by Type 2 and Type 3 Porositons; 45% and 40% respectively, with a 15% presence of Type 1 Porositon (Figure 14). The intraclast content of the Bivalve-Coated Grains-Intraclasts facies presumably accounts for this presence of micritic pore systems.

Ghawar Field Trends by Facies and Porositon

The Rosetta Stone study was designed to give both field level and well-level statistical results. At the well level, the sample set allows a study of the north to south variation in the maximum pore-throat diameters by facies and by variation within the range of maximum pore-throat diameters defined in each porositon.

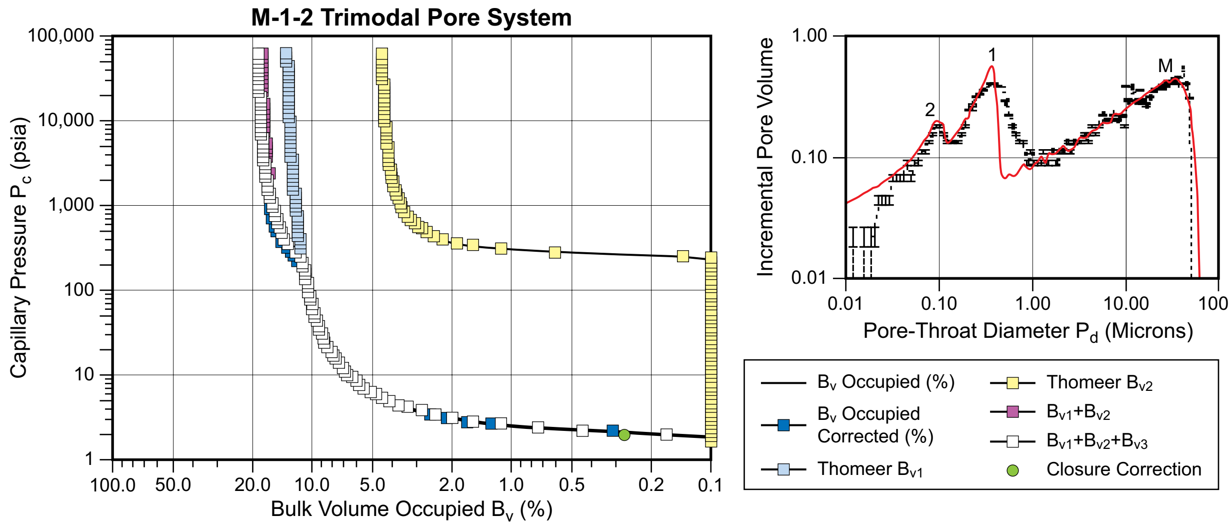

Figure 15: A Stromatoporoid-Red Algae-Coral M-1-2 trimodal pore system with core plug photograph (lower left). MICP data fit required three Thomeer hyperbolas (upper left); dark blue squares are the closure corrected data; white squares are the sum of the three Thomeer Hyperbolas; light blue squares (B_{v1}) show the M-porositon hyperbola; yellow squares (B_{v2}) show the second (Type 1) pore system before it is added to the first; red squares show the sum of the first two pore systems. The corresponding pore-throat diagram (upper right; data in black, Thomeer pore-throat diameter histogram in red) shows the three components. The third pore system is visible to the far left in the pore-throat diagram (copyright Schlumberger, Ltd.; reproduced with permission).

In Figure 16, the mean of the logarithm of the entry pressure Log(P_d) for each of the 10 Ghawar wells is shown for each of the facies. The data show a steady decrease in the Log(P_d) for Micrite microporosity from north to south, or a coarsening of the maximum pore-throat diameter, though all of these pore-throats are small. In contrast, the Log(P_d) steadily increases, fining from north to south for the other five facies, which are controlled by the M Porositon. Essentially, the largest pore-throats get smaller to the south. The picture is considerably different when viewed from the porositon perspective (Figure 17). The NS porositon trends are essentially flat except for the M Porositon, where Log(P_d) again shows an increase to the south. Hence the Type 1 to 3 Porositons appear to be uniform over the whole field.

When superimposing the Micrite facies trend over the porositon trends (Figure 18), we can reconcile these observations. Micrite is composed of Porositons Types 1 to 3, but dominated by Types 2 and 3. Hence the NS-trend for Micrite can only be explained by its enrichment with Type 2 and/or Type 1 compared to Type 3 porositons to the South. This indicates that the Micrite facies, being a varying mixture of the three microporositons cannot be used as a field-wide uniform petrophysical calibrator for well-log normalization. However, the Porositons 1, 2 or 3 can be used for fieldwide calibration and normalization.

PERMEABILITY IN THE MULTIMODAL ARAB D LIMESTONE

Thomeer (1983) found an empirical equation for air permeability based on the three Thomeer parameters (Appendix 1, equation A3). We used his equation to compute permeability for all the samples using only parameters from the first pore system, hence neglecting the smaller pore-throat modes. In a sample comprised of multiple Thomeer Hyperbolas (pore systems) written in decreasing order of maximum pore-throat diameter, e.g. M–1–2, the first pore system is M. We compared the calculated and measured values for the monomodal (require one Thomeer Hyperbola) samples and the bimodal (require two Thomeer Hyperbolas) samples (Figure 19). The good match implies that the permeability of the Arab D limestones is dominated by the properties of the first, commonly M

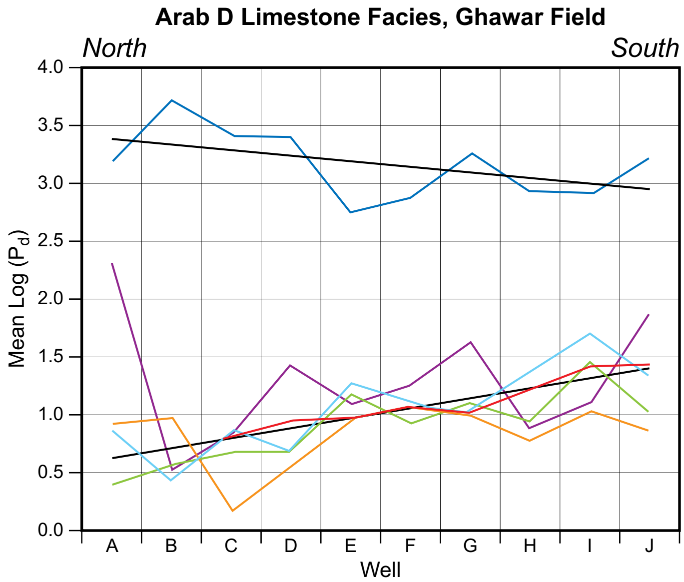

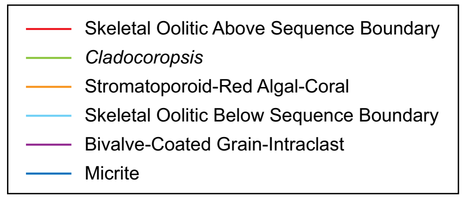

Figure 16: Ghawar field wells showing the trends in the mean of Log(P_d), the logarithm of the maximum entry pressure of the first pore system, by facies. Micrite maximum pore-throat diameters increase to the south while the maximum pore-throats of the other facies decrease southwards.

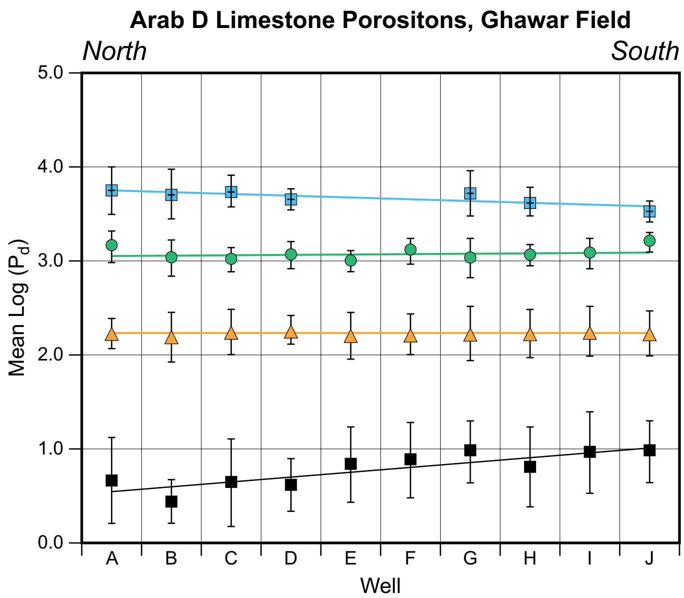

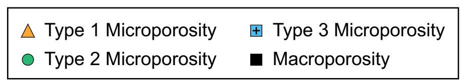

Figure 17: The NS-trend in the mean of Log(P_d) is inversely related to the maximum pore-throat diameter, by porositon. The trends are essentially flat for the three microporositons and continue to show a pore-throat diameter decreasing [i.e. increasing Log(P_d)] trend in the macroporositon.

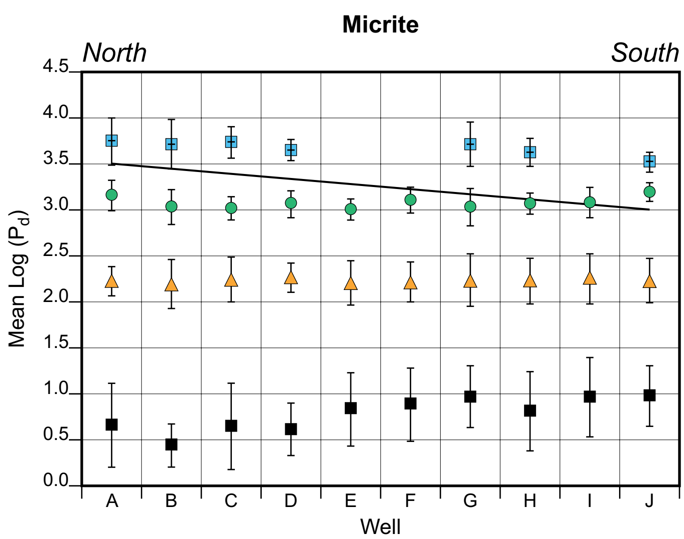

Figure 18: North to South porositon trend in the Ghawar field with the Micrite trend superimposed. This Micrite trend can emerge only if the mixing proportions of the 1 and 2 Porositons increase relative to Porositon 3 to the south. This implies that the Micrite facies properties are variable across the field and the facies itself does not represent a pure or stable petrophysical endpoint.

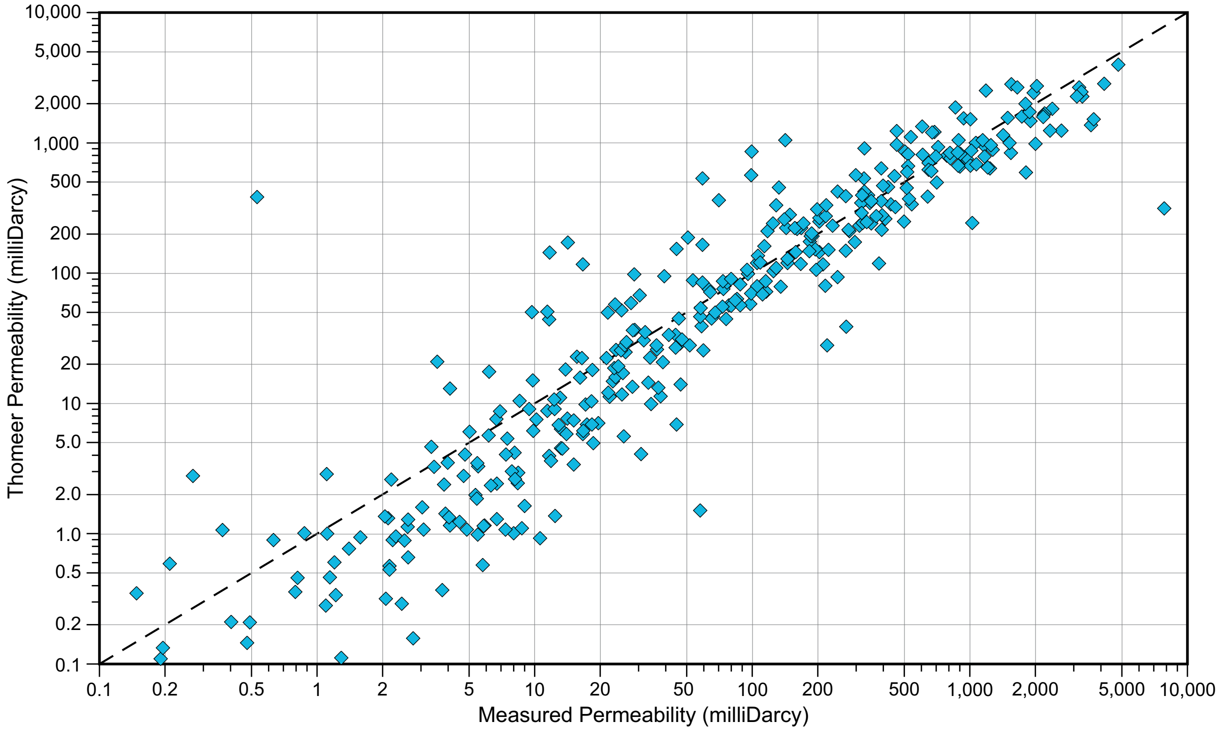

Figure 19: The Thomeer permeability can be computed for all samples with MICP Thomeer parameters. Thomeer gave no instructions as to the contribution to permeability from a multiple-pore system. In this case, the permeability is computed using only parameters from the pore system with the largest maximum pore-throat diameter. The agreement with measured values is excellent (even on a linear scale) over the wide range 0.1 mD to nearly 10 Darcies using logarithmic axes. Detailed investigations showed that the deviation from the trend could not be accounted for by invoking the contribution of the second pore systems of bimodals, which are common in rocks with permeability over 10 mD (see Figure 7).

porositon. Detailed comparisons between monomodal and bimodal sample data showed no detectable permeability contribution that could be attributed to the neglected smaller modes. This observation starts to explain the poor results that would arise from a conventional total porosity-permeability approach (Delfiner, 2007) to the data as shown in Figure 9 where at 25 pu, the permeability ranges from 10 to 3,000 mD.

Having isolated the M Porositon as controlling the measurable permeability, we investigated the explicit dependence of the permeability on each of the three M Thomeer parameters (Clerke, 2007). The major control on permeability (Figure 20) is the Thomeer parameter, $P_{d,f}$, the diameter of the largest pore-throat in the first (ordered by decreasing maximum pore-throat diameter) pore system, which is found by the equation between capillary pressure and capillary diameter:

$$P_c = 0.58 \times [\,(\sigma\cos\theta)/d\,] \qquad (1)$$

Using values for the Mercury-Air experiment interfacial tension and contact angle ($\sigma\cos\theta$), the mercury air pressure in psi; the diameter of the maximum pore-throat (capillary diameter) in microns is:

$$d_{\text{throat,max}}\ (\text{microns}) = 214/P_{d,f} \qquad (2)$$

The first displacement pressure is directly related to the maximum pore-throat diameter, which is the maximum pore-throat diameter of the first porositon when ranked by decreasing maximum pore-throat diameter.

The correlation R^2 between permeability and $P_{d,f}$ is 0.65. Of the three Thomeer parameters, the most important for permeability is clearly $P_{d,f}$, or the maximum pore-throat diameter or the largest pore-throat diameter of the first (usually the Macro) pore system. The next best correlation is found between

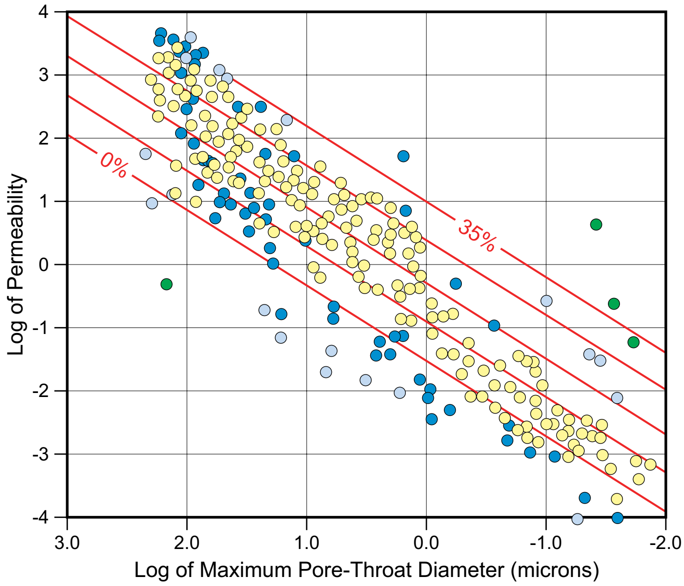

Figure 20: The large and high-quality data set (this study, Appendix 3) enable a detailed investigation of the sample permeability against the Thomeer parameters and their combinations. These demonstrate that permeability is most strongly controlled by Maximum Pore-Throat Diameter value. The correlation with Maximum Pore-Throat diameter is good and can be further improved by adding a second parameter, the total porosity is shown here (partially obscured 3-D porosity axis present as the red grid for porosities increasing into the page from 0 to 35%). Yellow points are within one standard deviation of a 2-D surface fit. Dark blue points are within two standard deviations.

permeability and the total sample porosity, i.e. $R^2 = 0.55$, but other Thomeer parameters could also be used with only slight decrease of the correlation. We choose to continue with the total sample porosity because of the ease with which it is determined from well logs.

Using these results, we propose a new, simple two-term permeability model, which has potential for well-site implementation using properly processed well-log data (Figure 21 and 22):

Log (Measured Permeability) =
[a] + [b] x [Log (maximum pore-throat diameter)] + [c] x [Porosity (%)] (3)
a = -1.544, b = 1.206, c = 0.0727

The measured-versus-predicted plot for the proposed two-term model has a correlation coefficient R^2 of 89%. The measured-versus-predicted plot for the proposed two-term model shows excellent results over seven orders of magnitude in permeability (Figure 22). This model has many similarities to the approach of Lucia (1995) who also proposed a pore space-permeability classification based on two variables: the particle size and the interparticle porosity for non-vuggy rocks. This approach has been further developed to include the behavior of the imbibition oil relative permeability in multimodal M–1 pore systems (Clerke, 2007).

NMR DETECTION OF PORE BODY MODALITY

After correcting NMR log data for reservoir and borehole fluid and fluid-surface interaction effects, petrophysicsts can derive some information about the pore system or its attributes (e.g. permeability or saturation). Here we deploy a different strategy. We use the knowledge gained from studying the pore systems and pore-throats from our MICP studies of the Arab D limestone and investigate whether they are present in the NMR log data. Although we have not yet performed a rigorous correction for every fluid effect, our initial investigation focused on the conformance of the two data sets at every point of contact. This is supported by information that the Arab D Reservoir apparently has only minimal difference between the NMR properties of the two reservoir fluids at reservoir conditions (R. Akkurt, personal communication, 2007).

The pore system modality detected within the MICP data records the distinct occurrence of multiple-pore systems, each with a range of possibilities for the maximum-pore-throat diameter (see Figure 5b). The use of the words "pore bodies" and "pore-throats" tend to give rise to the concept that the pores themselves are constructed from discrete objects such as connecting tubes and spheres. This is often a useful approximation. In reality, a pore-throat is a critical pore body section whose radius and position limits access to the remainder of the pore body or bodies. The position and size of these pore-throats is governed by many factors such as the arrangement of the grains, grain sizes, sorting, angularity, configuration and cementation.

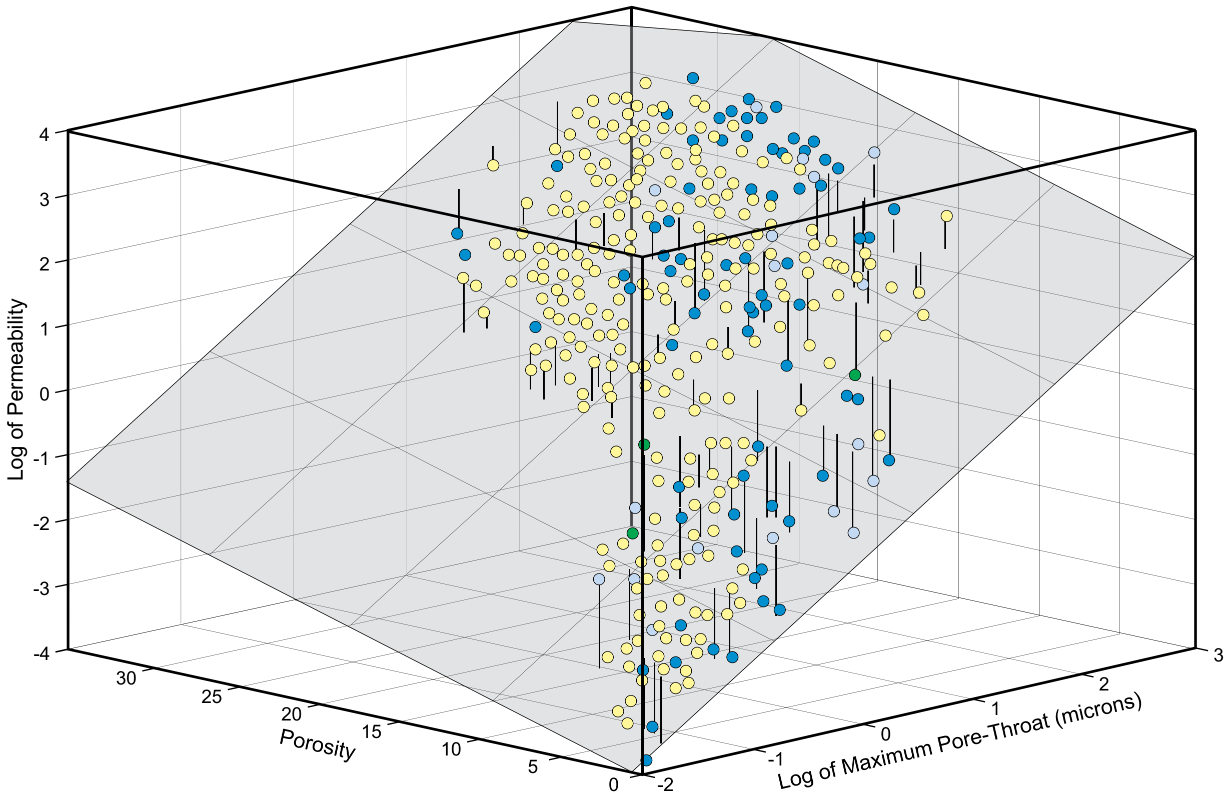

Figure 21: A three-dimensional view of a two-dimensional surface fit (Equation 3) to computed permeability from total porosity and Maximum Pore-Throat diameter in TableCurve3D™. Points shown are as in Figures 9 and 20.

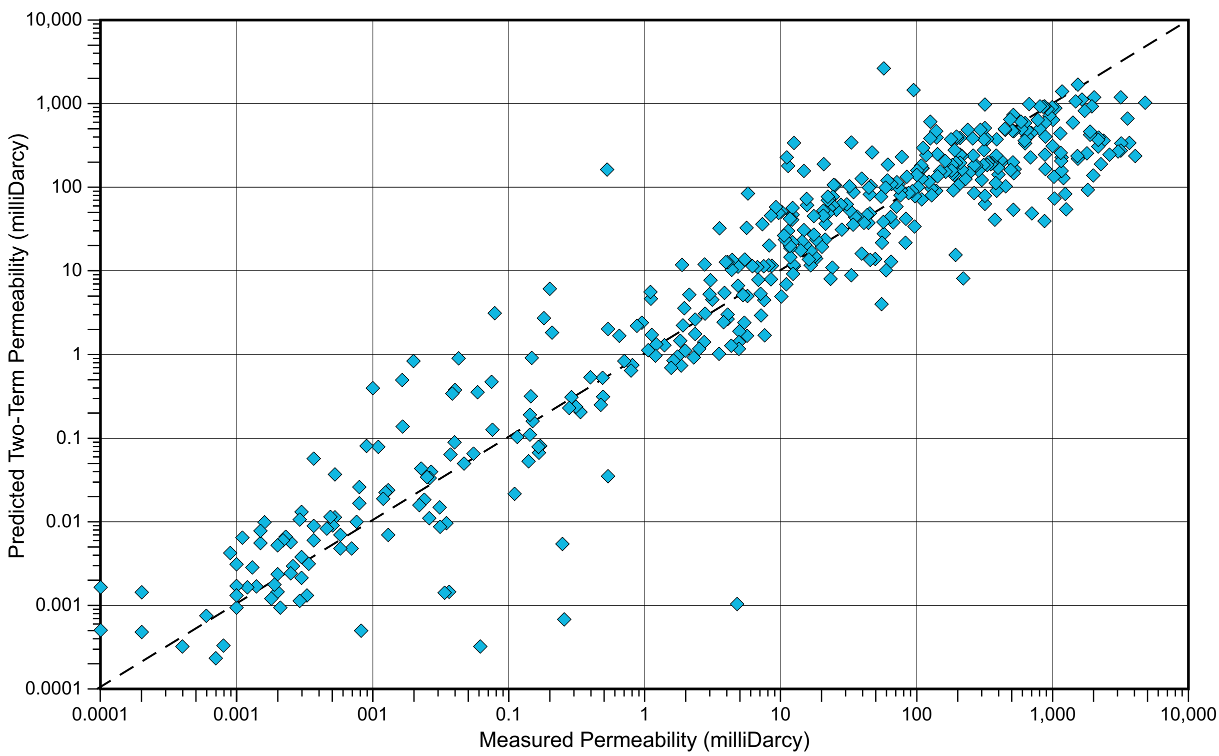

Figure 22: The permeability predicted using the two-term permeability equation versus measured permeability for the data set of this study (Appendix 3).

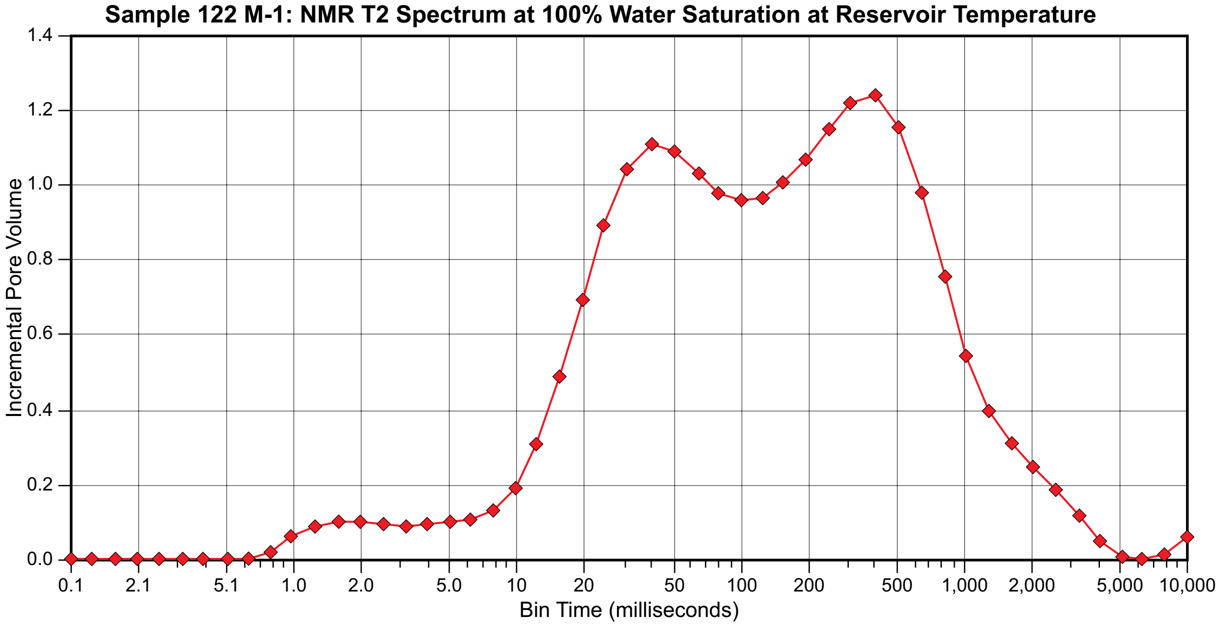

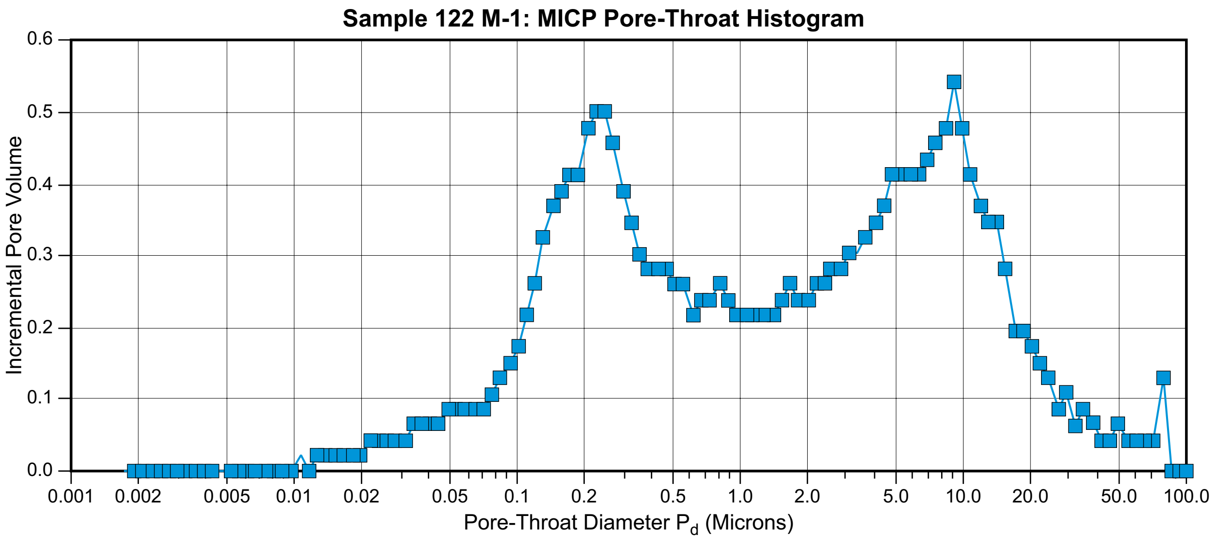

Figure 23a: The NMR T2 spectrum of an M–1 core plug at 100% water saturation and at reservoir temperature (upper half) and the MICP pore-throat histogram for the same core plug (lower half). Bimodality is evident in both instances.

If pore-throats show multimodality in the MICP data, it is an attractive leap to conjecture that there may also be pore-body multimodality, termed "porobodons". That is, the modes in the core plug MICP maximum pore-throat diameter spectrum might have counterparts in the NMR pore-body spectrum. The pore-throat and pore-body data are shown in Figure 23a for an M–1 pore system core plug where laboratory NMR measurements have been performed at 100% water saturation at reservoir temperature after which MICP data were acquired from the core plug.

At reservoir conditions and with reservoir fluids, the pore-body modality from an NMR well log in the Arab-D is displayed versus total porosity in Figure 23b. A pore-body modality indicator is easily computed by recognizing that it is equivalent to half the number of inflection points in the NMR signal. Alternatively, a threshold crossing-counter technique can also be applied. The NMR data from even one well is many times more abundant than the more than 500 MICP samples and it also represents a completely different scale of investigation. Yet the two plots (Figures 6 and 23b) are extremely similar, which tends to support the attractive 'porositon-porobodon' conjecture.

To further examine the "porositon-porobodon" conjecture, we anticipated its form by computing the histogram of the largest controlling pore-throats (Figure 5a) weighted with the average porosity of the histogram bin (Figure 24). Figure 24 shows a first estimate of what an NMR spectrum from the Arab D limestones might resemble if the porositons and porobodons do have the conjectured correspondence.

The porosity-weighted, pore-throat histogram is a basic estimate because the NMR device responds to the amount of porosity governed by a characteristic hydrogen spin-decay time rather than a pore-throat diameter bin. In Figure 24, we see that the M Porositon (to the left of 4.6 microns pore-throats) is heavily weighted by its abundant pore volume. The common Type 1 microporosity (from 4.6 microns to 0.35 microns pore-throats) is weighted by a smaller bin porosity; porosity Types 2 and 3 (less than 0.35 micron pore-throats) are now even lower. An NMR pore-body spectrum might look similar to this if the correspondence to porositons is correct. The x-axis values in terms of milliseconds of NMR hydrogen spin-decay times can only be estimated. The very large pore-throats (and associated pore bodies) will have long, many-second decay times. The Type 2 and Type 3 microporosity will have very fast NMR decay times (few milliseconds). For comparison, an actual NMR pore body spectrum for the Arab D is shown in Figure 25. There is indeed a distinct similarity between what we have estimated (Figure 24) and what is obtained (Figure 25). At each of these three points of contact between the two data sets; single core plug, modality versus porosity, porositon modeled spectral shape, the data are very similar.

The evidence is encouraging that the maximum pore-throat modality seen in core plug MICP is also present in the much larger rock volumes investigated by the NMR well logs. Even after upscaling, the porositons may have equivalent porobodons. This is a fruitful path for future investigations.

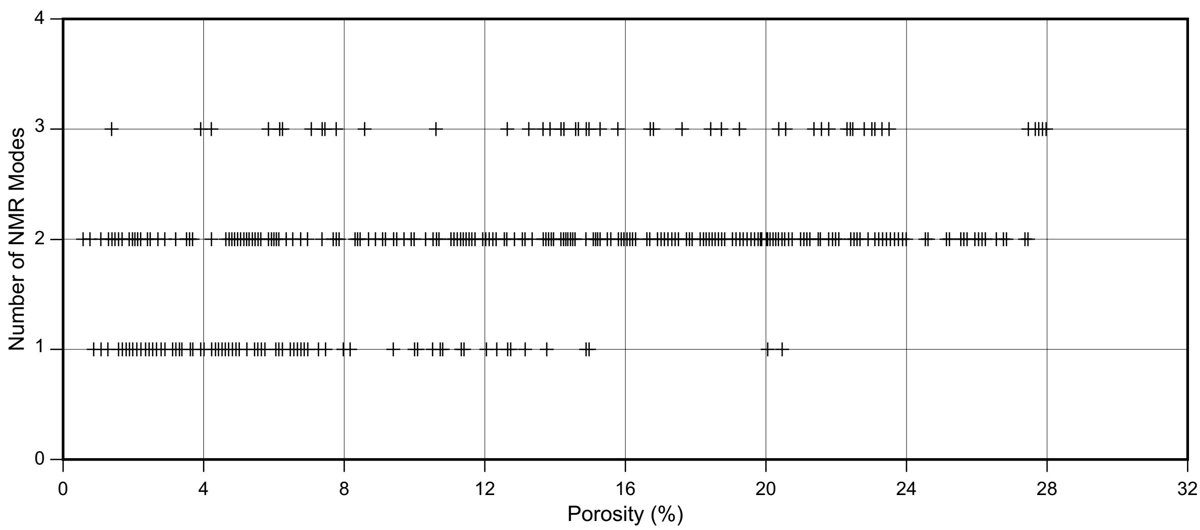

Figure 23b: The well-log NMR pore body modality from one Arab D well plotted versus porosity without a color frequency z-axis, but with occupancy indicated by the density of the black points. The pore-body modality is easily computed by tracking the number of inflection points or threshold crossings and then dividing by two. The data compare qualitatively and semi-quantitatively well with the data set of Figure 6, especially considering the disparate data sets.

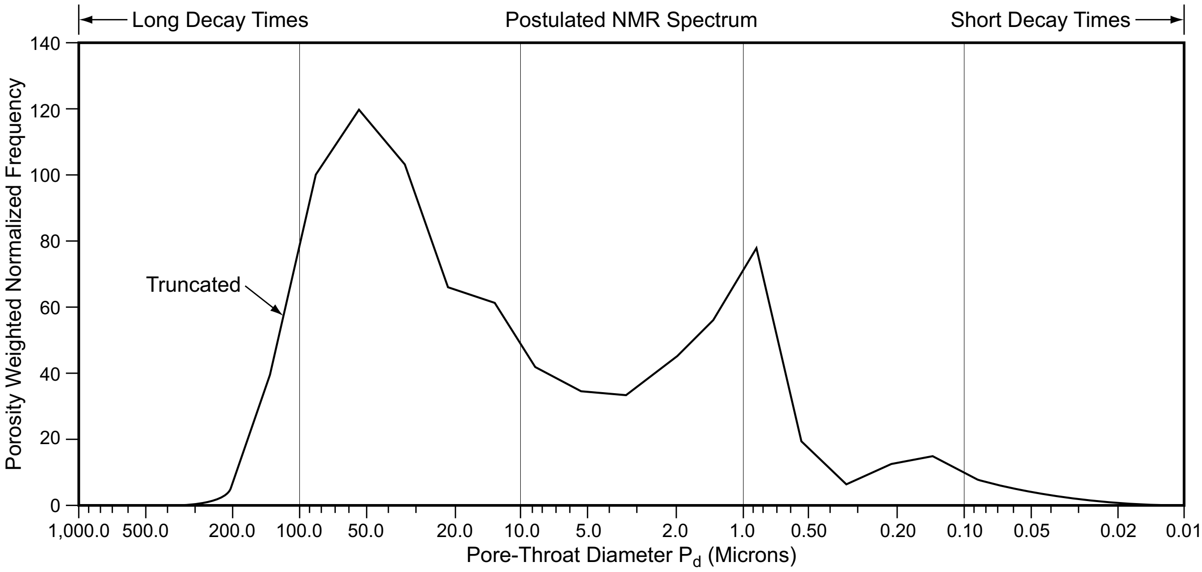

Figure 24: The frequency histogram of the maximum pore-throat diameters (Figure 5) is here weighted by the average pore volume associated with each bin of pore-throat diameters for the 860 Thomeer Hyperbolas used to type-curve match 454 MICP samples (this study, Appendix 3). The M Porositon pore-throats, which were a low broad-band in Figure 5 are now weighted by their abundant pore volume. The Type 1 pore-throats are associated with a smaller pore volume and an even smaller pore volume with Type 2 and 3 micropores. For the average values of the pore volumes of the porositons see Table 4. Large pore bodies should correspond with long NMR decay times and small pore bodies with short NMR decay times.

CONCLUSIONS

Mercury injection capillary pressure (MICP) data from the Arab D limestones in Ghawar field (Appendix 3) were analyzed using Thomeer Hyperbolas (Appendix 1). The analysis identified four discrete modes of maximum pore-throat diameter values termed *porositons*; the largest of these is macroporosity (M Porositon) followed by three types of microporosity (Porositons 1, 2 and 3). Modality is a new and important indicator for carbonate reservoir characterization because it demonstrates that the presumably continuous maximum pore-throat diameter axis can be well-represented using only four discrete modes.

The pore systems of the Arab D limestone (Appendix 2) have been described as combinations of these porositons, with 70% of the samples showing bimodal or trimodal behavior. Three of the six facies have nearly identical porositon combinations, leaving four "porositon combination effective" facies. The best reservoir quality shows a common M–1 bimodal pore system, with the M Porositon carrying the measurable permeability. The M–1 matrix pore system acts as a dual porosity – single measureable permeability system.

The number of modes in each of the facies and the type of microporosity are new and important geological and petrophysical attributes that are not accessible with conventional well logs but accessible through MICP analysis. A fruitful approach to NMR well logs processing is to extract pore-body modality (porobodons) that are related to the porositons. The *conjectured* porositon-porobodon correspondence suggests that a very similar behavior in terms of mode number, position and occupancy is present in the NMR signal, and early evidence is given to support this. This paper suggests that NMR data might be used to support facies identification.

Additionally, the dominant presence of multimodal pore systems in the best reservoir intervals of these carbonates requires that the static and dynamic property models be fully generalized for multimodal pore systems. We have demonstrated one generalization for permeability; showing that only attributes of the M (Macro) Porositon are significant. The generalization to imbibition oil relative permeability in multimodal M–1 pore systems has been published elsewhere (Clerke, 2007).

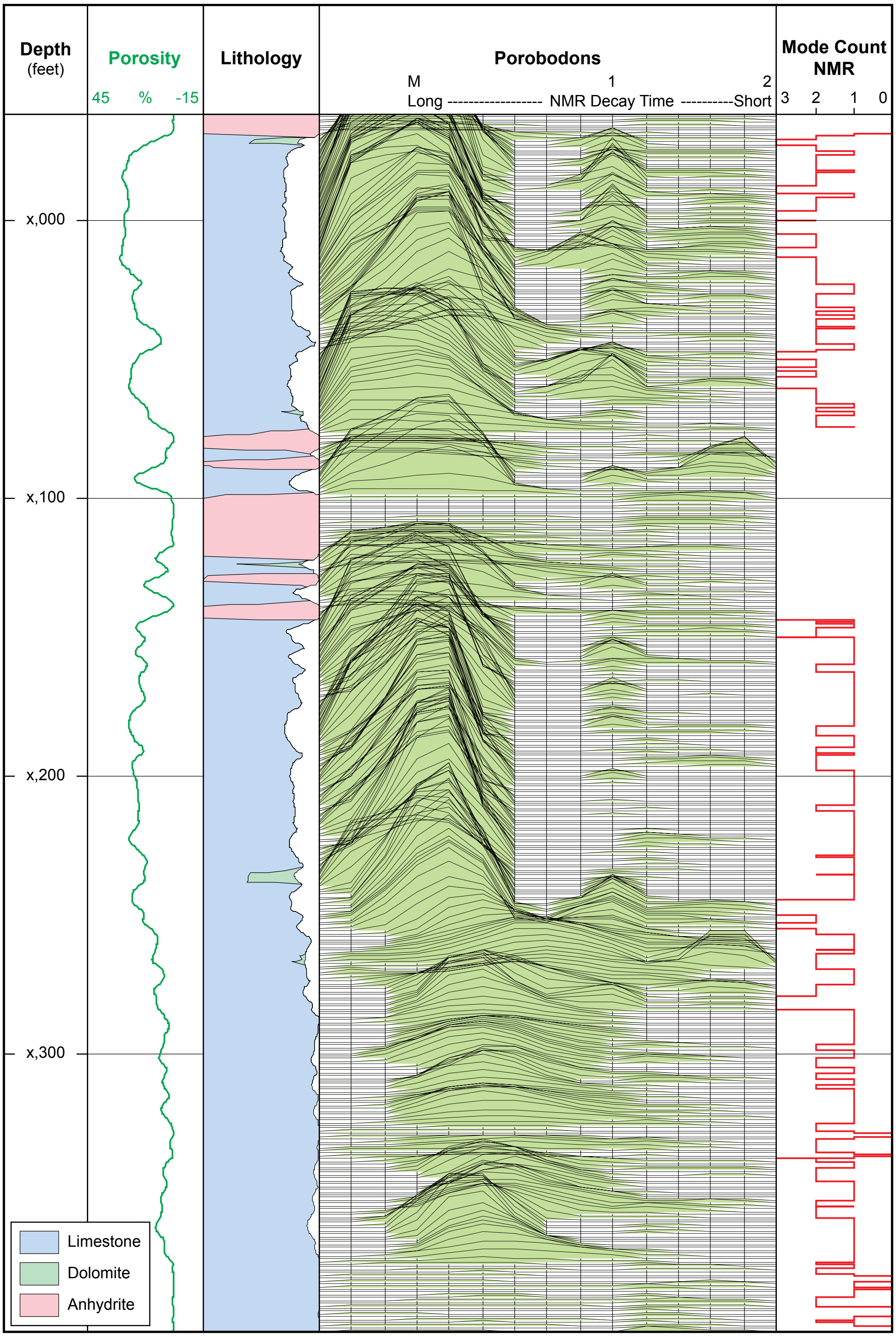

Figure 25: An Arab D NMR log section shown with multimodal NMR spectral data processed to deliver a mode count in Track 4. Track 1 shows the porosity information, Track 2 the lithology, Track 3 the spectral NMR data with large pore bodies on the left and smaller pore bodies to the right (sedimentological orientation) and in Track 4 are the results from the mode counting computation. When viewed at a glancing angle, the NMR spectral signals lie in three distinct vertical time decay domains. The Type 3 microporosity is estimated to decay too rapidly to be observed with the NMR run in the current tool operating mode. The pore volume associated with Type 3 microporosity is very small.

Using the Rosetta Stone analogy, this study was designed and executed as a three language decoding exercise, which enabled a strong connection to be made between data in the domains: geological facies, pore systems and reservoir-flow properties. The overall workflow and analysis processes as demonstrated for the Arab D limestones can most likely be applied to other multimodal carbonate pore systems and reservoirs when the appropriate data are collected.

APPENDIX 1: THOMEER HYPERBOLA METHOD

Thomeer (1960) developed a method for the analysis of mercury injection capillary pressure (MICP) data, which was used primarily within Shell (Thomeer, 1983; Smith, 1992; Hawkins et al., 1993). He observed that the data from the MICP experiment, for simple rock types, could be represented by a hyperbola when plotted on Log-Log graph paper. The data are: (1) volume of mercury injected, and (2) applied pressure between the wetting (air) and non-wetting phases (mercury) as mercury intrudes into the pore space fraction. For the rock sample, the bulk volume is known, so that the volume of mercury injected can be re-expressed as a fraction of the total sample bulk volume, B_v. To fit the hyperbola to the data, the value of two asymptotes, B^∞, P_d, are required. The Thomeer Hyperbola is shown in Figure A1, and can be expressed as:

$$\text{Log}\ (B_v/B^\infty) \times \text{Log}\ (P_c/P_d) = K, \text{ where K is a hyperbola shape factor} \qquad \text{(A1)}$$

The asymptotes are: B^∞ is the percent bulk volume occupied by mercury at infinite applied pressure and P_d, the displacement pressure required to first intrude mercury into the largest pore-throat. Thomeer chose to express constant K = Log [exp (- G)] such that Equation A1 becomes:

$$B_v / B^\infty = \exp\ [-G/\text{Log}\ (P_c/P_d)] \qquad \text{(A2)}$$

where G is the *Pore Geometrical Factor* and determines the shape of the hyperbola (Figures A1 and A2). In practice, B_v and P_c data from the MICP experiment are fit by equation (A2) to determine P_d, B^∞ and G, for individual samples.

Thomeer (1983), using a weighted regression on data from 279 rock samples, found a relationship between the three parameters and air permeability (K_a):

$$K_a = 3.8068 \times G^{-1.3334}\ (B^\infty/P_d)^2 \qquad \text{(A3)}$$

This equation reproduces the measured permeability to within a multiplicative uncertainty of 1.82 (Figure A3 and Table A1). With this result, Thomeer demonstrated why permeability-porosity crossplots fail, especially in carbonates, because important details about the pore network are missing in the relationship.

Spreadsheet Implementation

Unlike the plastic overlays that were originally used to implement this technique, today the Thomeer analysis method can be implemented in an Excel™ spreadsheet, available from many of the MICP data providers (Clerke and Martin, 2004). Hyperbolas are fit using the *Solver* function to minimize the error signal derived from the difference of the actual versus predicted capillary pressure curve. Both the data and its derivative can be used to fit the Thomeer Hyperbola, analogous with type curve matching in Pressure Transient Analysis. Superposition of Thomeer Hyperbolas for multiple pore systems is carried out by parsing the pore system in the pressure domain. All of this is implemented in a highly interactive way. The Thomeer permeability is continuously generated for comparison to the measured permeability. The result for the 125 MICP Arab D Ghawar Hagerty and Cantrell (1990, unpublished report) samples is shown in Figure A4.

A basic result from the Thomeer analysis of the MICP data is a record of the number of Thomeer Hyperbolas (used here as equivalent to 'pore system') required to match the data. We call this integer the "pore system modality". The minimum would be one and the maximum encountered in our study was three. To limit trivial occurrences of pore system multimodality, we add to the Thomeer MICP fitting process the requirement that a volume of at least one unit of porosity be present for a significant second or even third pore system.

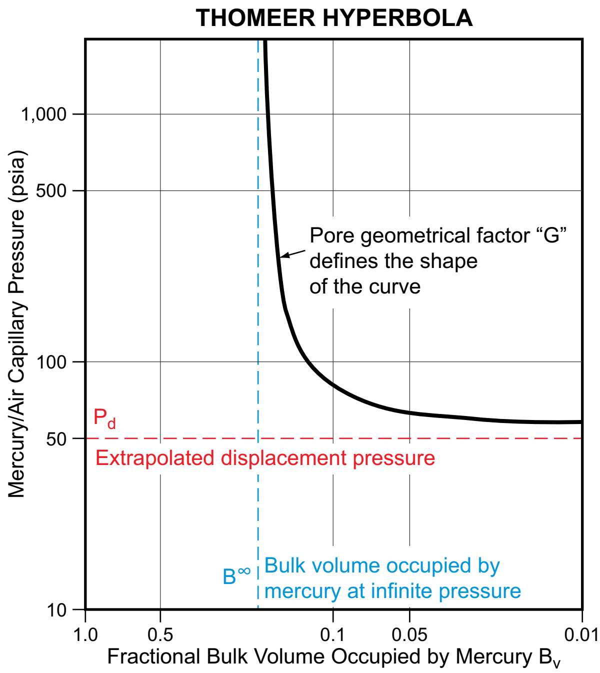

Figure A1: Thomeer Hyperbola is determined by three parameters (two asymptotes): (1) P_d, the displacement pressure required to first intrude mercury into the largest pore-throat; (2) G, the Pore Geometrical Factor, and (3) B∞, the percent bulk volume occupied by mercury at infinite pressure (Thomeer, 1960; reproduced by permission of SPE).

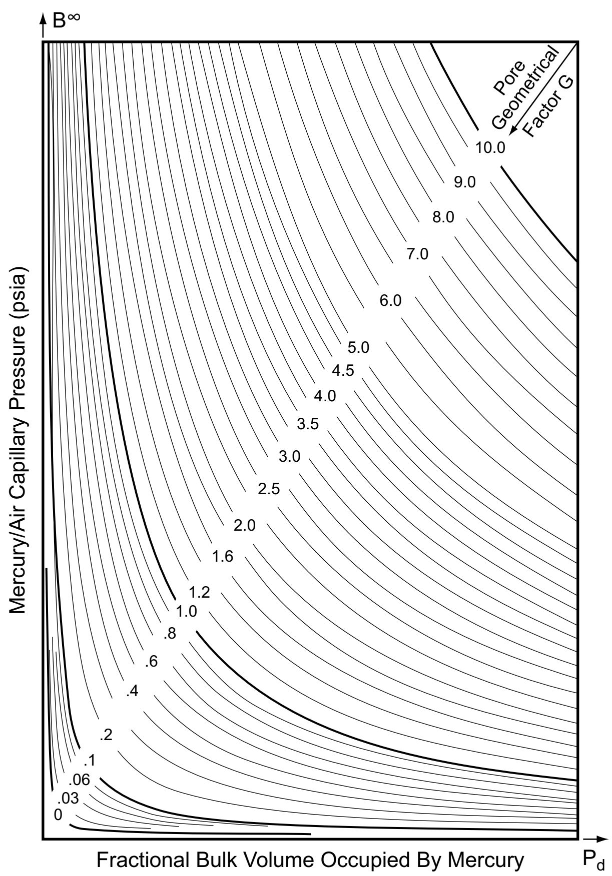

Figure A2: Thomeer Hyperbolas for various values of the *Pore Geometrical Factor G*, which determines the shape of the hyperbola (after Thomeer, 1960; reproduced by permission of SPE).

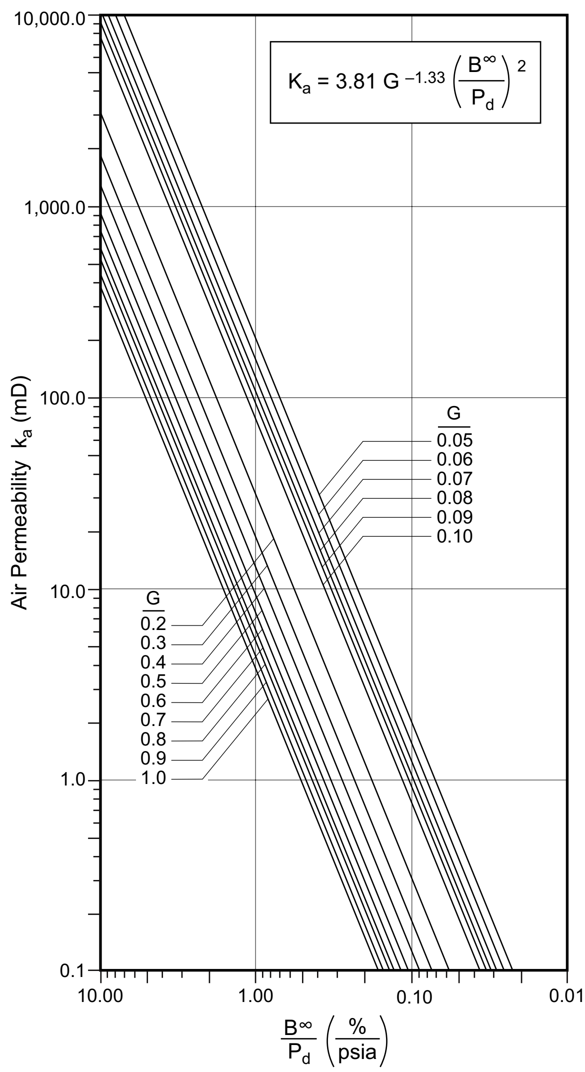

Figure A3: Air permeability as a function of G, P_d, and B∞. See Figure A1 for notation (after Thomeer, 1983; reproduced by permission of SPE).

Table A1:
An example of different permeabilities for the same porosity

Porosity * ø (%)	G	Largest Pore-Throat Diameter (microns)	Equivalent P_d (psia)	Calculated k_a (mD)
20	0.1	1	214.0	0.7
20	0.1	5	42.8	17.9
20	0.1	20	10.7	286.6
20	0.3	1	214.0	0.2
20	0.3	5	42.8	4.1
20	0.3	20	10.7	66.2
* Assumed that ø = B∞				

An example of different permeabilities for the same porosity (after Thomeer, 1983; reproduced by permission of SPE).

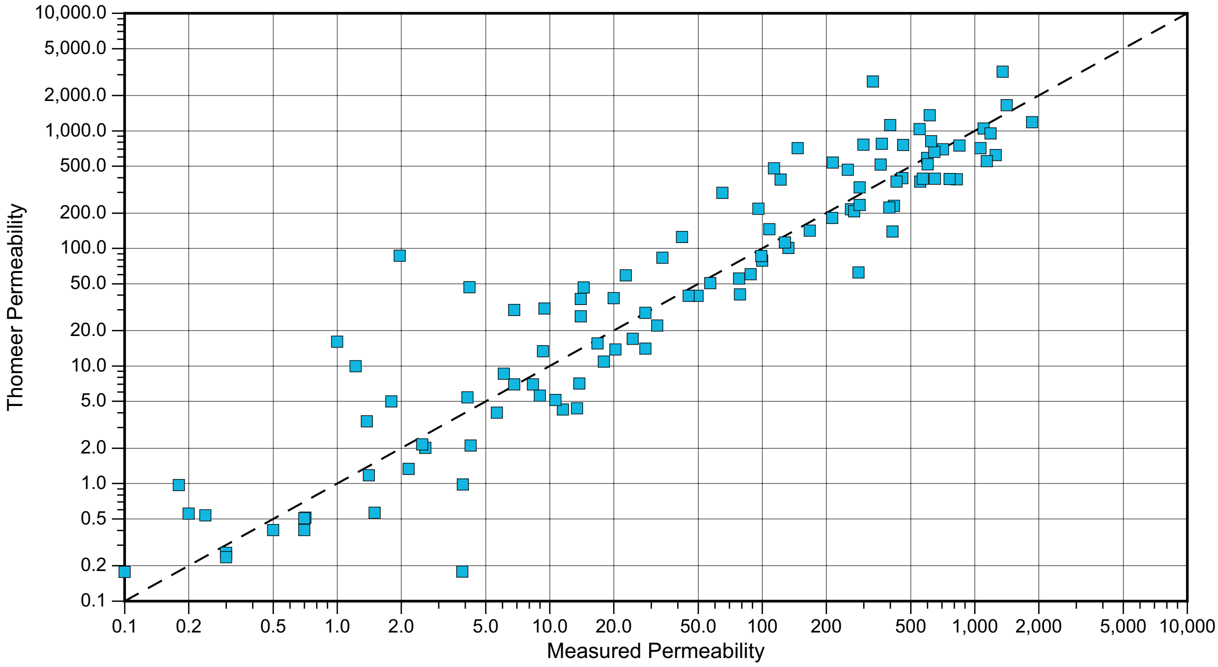

Figure A4: The computed Thomeer permeability versus the measured permeability for the Arab D Reservoir MICP Data (125 samples) set of Hagerty and Cantrell (1990, unpublished report).

Closure Correction

In the process of obtaining a core-plug or rock-chip sample, an artificial boundary is placed into the pore geometry – the cylindrical or outer-plug surface. The plug saw cannot cleave grains of the sample and so leaves a rough outer surface where grains may have been removed. If the sample contains very large pores, these can be dissected by the sample/plug surface in ways not representative of the formation. These surface irregularities and pore-body dissections create an initial storage of mercury that must be filled before the normal pore-system geometry is encountered by the mercury. This volume artifact requires a *closure correction*, and is one of the most troublesome issues in the analysis of MICP data, particularly since a small relative volume change in the large pore-throats strongly affects the permeability calculation. This effect and its correction are illustrated for sample 30 (Hagerty and Cantrell 1990, unpublished report), which also exhibits a dual-pore system at about 1,000 psi (Figure A5).

An important feature of the interactive Thomeer spreadsheet is the ability to pick and revise the closure correction to iteratively solve for the Thomeer parameters while comparing the computed and measured permeability. The spreadsheet also incorporates the ability to select the closure correction

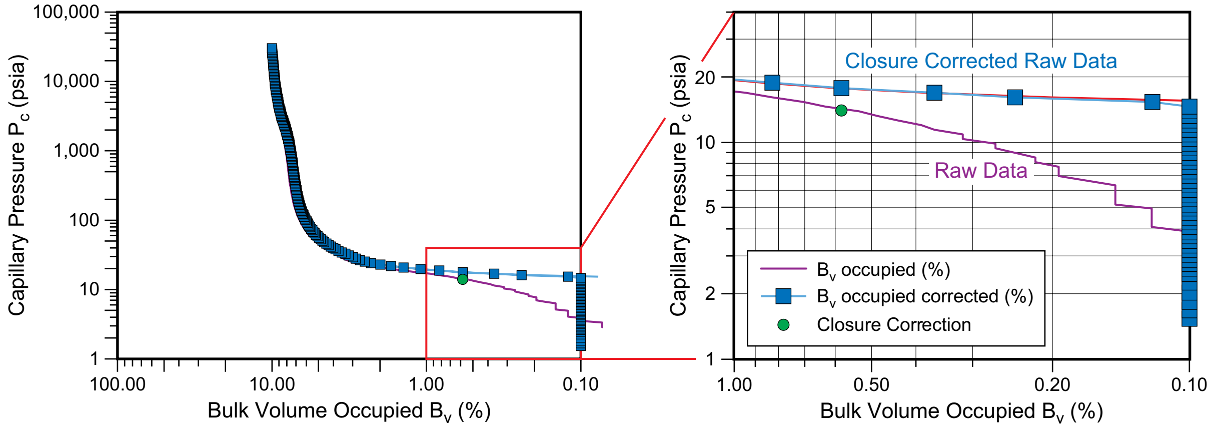

Figure A5: The Thomeer spreadsheet enables rapid and visual interaction with the user's choice of closure correction and determination of the three Thomeer parameters.

and visualize the corrected data and the hyperbola in the derivative or Pore-Throat Size Distribution space. The selection of a closure correction volume (red bar) is illustrated for a bimodal sample on the Pore-Throat Diameter (derivative) plot in Figure A6. Data is in black, Thomeer hyperbola in red.

Application of Thomeer Analysis

The use of the Thomeer method for the Arab D Reservoir at Ghawar is focused on three issues: (1) facies-dependent saturation-height modeling; (2) free-water level determination; and (3) facies-dependent recovery estimation. The general process of defining petrophysical rock types based on Thomeer analysis of capillary pressure behavior is illustrated in Figure A7. Fitting of the MICP data is done for all samples and the resulting parameters are statistically analyzed, PRT's are defined and then forward modeled.

The result of the process shown in Figure A7 is displayed in Figure A8, which shows five clusters (PRT's) in the Thomeer parameter space (not the Arab D) and the forward model of each cluster's average Thomeer parameters. This application is a specific branch of the broader range of applications of MICP and capillary pressure data; namely: (1) facies-dependent saturation-height modeling; (2) conductive minerals; (3) fresh or varying formation water salinity; (4) very low porosity; (5) complex pore systems – fractured, vuggy, microporous; thin sands; (6) determination of depth to water contacts; (7) evaluation of downdip potential; and (8) predictions in the absence of or poor resistivity logs.

Properties of Thomeer Hyperbolas

A single pore system can be represented by one Thomeer Hyperbola and is characterized by three parameters: P_d, B^∞ and G, each of which has measurable errors to characterize uncertainty. This is in contrast to other methods (e.g. Leverett J Function, see next page) that are based on MICP data, but introduce additional uncertainties when scaling the data to measured permeability and porosity. The Thomeer parameters are intuitive: largest pore-throats, sorting of pore-throats, and total amount of porosity. They describe the pore system in a similar manner to grain system: i.e. largest grains to largest pore-throats, sorting of grains (e.g. Trask sorting), and sorting of pore-throats (G).

Petrophysical Rock Type (PRT) can be defined as an object in the Thomeer parameter space (P_d, B^∞ and G), i.e. a similar pore system. The parameters for PRTs can be operated on statistically (mean and standard deviation) to create average capillary pressure curves and their error bounds. Estimates of recoverable hydrocarbon can be guided by the knowledge of a complex composite pore system and hence by PRT.

Air permeability can be computed and predicted from the pore network parameters, P_d, B^∞ and G, to within a multiplicative uncertainty of 1.8, and this can be compared to a measured permeability. A Thomeer forward-modeled capillary pressure curve can be generated from insight into the generating

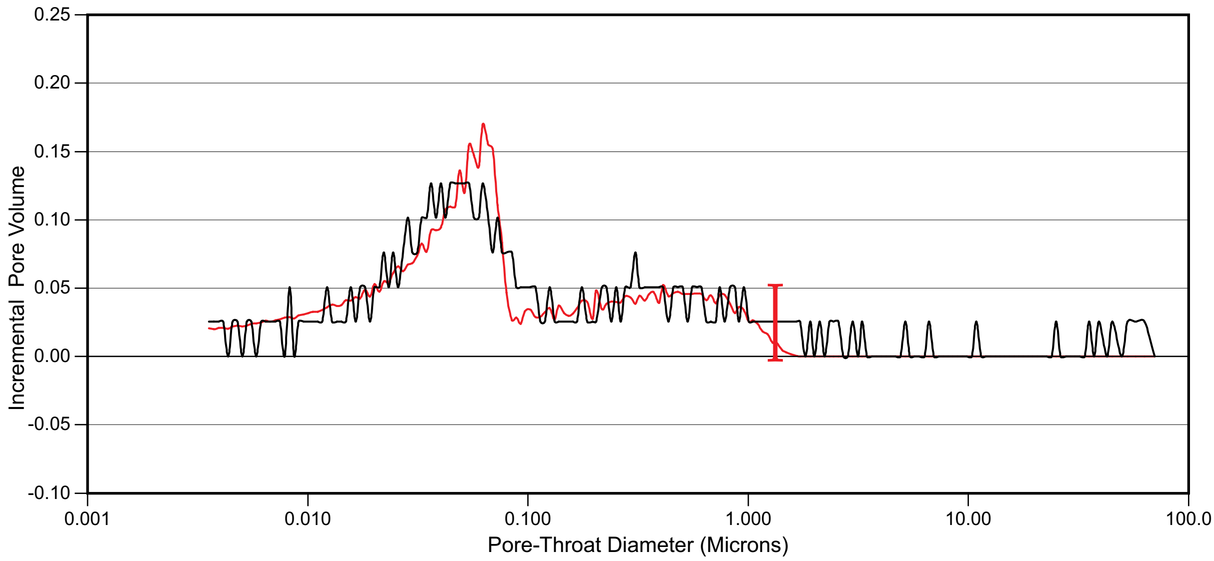

Figure A6: An Arab D sample exhibiting a bimodal pore system shown with the closure correction (red bar) indicated on the pore-throat frequency plot.

parameters that can come from a variety of sources of rock data, from cores to cuttings and the *Shell Rock Catalog* (Thomas et al., 1995).

Thomeer Hyperbolas parameterize the process of filling the pore space with mercury (nonwetting phase) while displacing air (wetting phase), a drainage process. Suitable adjustments can be made to convert this behavior to other fluid systems in drainage (oil-water, gas-water).

Thomeer Hyperbolas can be combined or superposed to quantify complex pore systems. Superposition can be used to quantify porosity types and entry pressures, i.e. microporosity. The Thomeer function parameterization of MICP data has been shown to upscale (Buiting, 2007).

Square Root K/Ø Methods: Leverett J Function and Flow Zone Indicator (FZI) Technique

Whereas the Thomeer method has been used for many years in Shell, in other companies the Leverett J Function method (Leverett, 1941) and the related *FZI technique* (Amafuele et al., 1993) have been more extensively used. Here we discuss and compare these methods. The Leverett J Function characterization of a capillary pressure curve is defined by:

$$J(S_W) = (0.217\ Pc/\sigma) \times \sqrt{(K/\text{ø})} \qquad \text{(A4)}$$

where S_w is water saturation, K is permeability, ø is porosity, P_c is the capillary pressure and σ the interfacial tension between the wetting and non-wetting fluids. The rock's pore system is characterized by K/ø, and its square root is termed the *pore system speed* as it is the ratio of the flow parameter to the storage parameter. The Leverett method seeks to reduce the mathematical complexity of the complete behavior of many capillary functions by finding a scaling relationship among them. It is important to note that the use of this parameter to characterize the whole pore system in a complex pore system (mixture of macro, meso and micro pores) is incomplete, because the flow behavior of the pore system is strongly dominated by the large pores (low capillary pressure).

The FZI and Leverett J Function techniques are related in that they both use the √(K/ø) parameter, but in the former the height dependence is removed and replaced by a fixed value. The Reservoir Quality Index (RQI):

$$RQI = 0.0314 \times \sqrt{(K/\text{ø})}, \text{ which is } J(S_W) \text{ when } (0.217 \times P_c)/\text{sigma} = 0.0314 \qquad \text{(A5)}$$

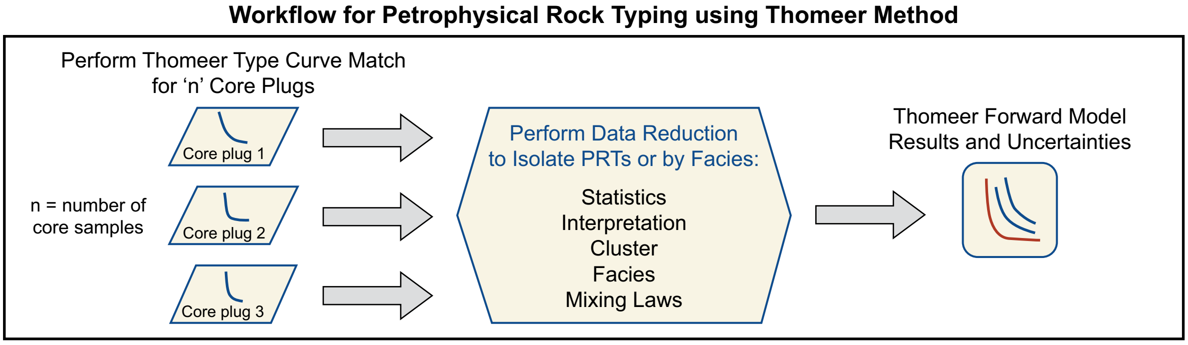

Figure A7: Workflow process diagram for the determination and analysis of multiple petrophysical rock types by using Thomeer type curve matching to the MICP data.

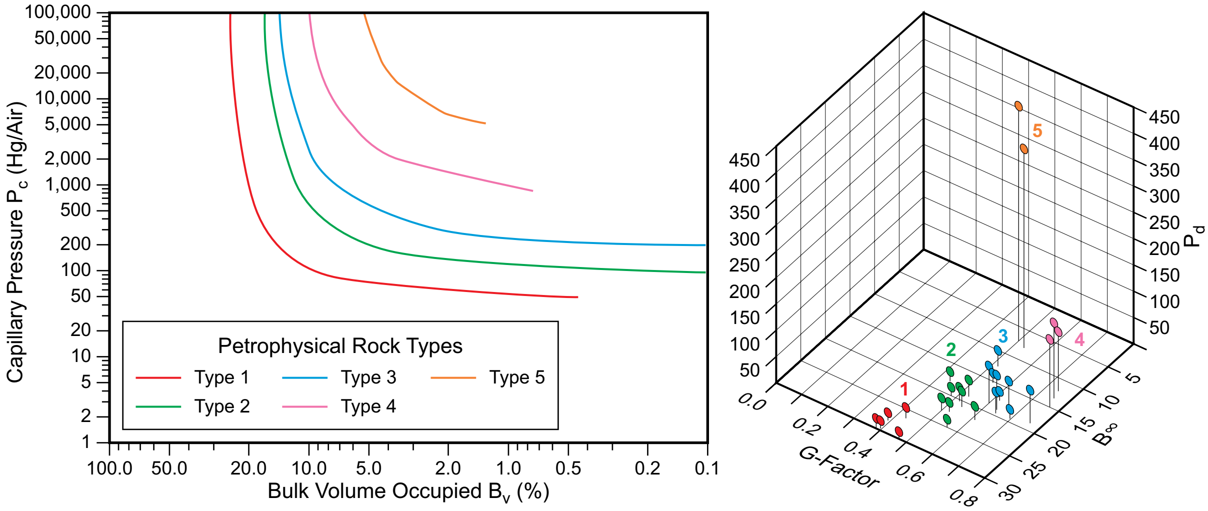

Figure A8: Clusters in the 3-D Thomeer space for this reservoir indicate five petrophysical rock types. The average capillary pressure curve for each PRT is shown.

or when P_c = 4.5 psi (again low capillary pressure). The FZI method invokes the use of a constant RQI versus NPI (Normalized Porosity Index) slope.

This ratio, FZI, measures to what extent it is true that when we increase porosity by replacing matrix by pores, we do this by adding pore systems of the same speed $\sqrt{(K/ø)}$, and thereby keep FZI constant. Here we make contact with the capillary bundle model of Purcell, because when pore systems of the same speed are added, it is equivalent to adding one or more tubes of the same type to the bundle.

$$NPI = ø / (1 - ø) \text{, and } FZI = RQI / NPI \quad \text{(A6)}$$

Square Root K/ø methods have several limitations. They cannot be superposed and do not completely characterize the high-pressure behavior, nor microporosity issues. Hence, recovery issues associated with multimodality are not well-represented. The Leverett J Function is dependent on two laboratory variables, k and ø; their individual uncertainties are compounded. It is not rock-texturally intuitive, does not provide a prediction of the permeability and hence does not provide a quality-control cross-check on the permeability data and measurement. Further, the clustering and inclusion of high-pressure behavior are a subjective visual process not leading to statistical measures. Finally, the approach does not lead to a method for determining the average capillary pressure curves and their uncertainty bands from laboratory data. Ekrann (1999) stated that "The true effective capillary pressure curve is not proportional to the rock Leverett J Function."

APPENDIX 2: ARAB D FACIES

Lithofacies	Skeletal Oolitic Above Sequence Boundary	*Cladocoropsis*	Stromatoporoid-Red Algae-Coral	Skeletal Oolitic Below Sequence Boundary
Hadley, K., J.C. Wendte, EPR.68ES.77 Mitchell_EPR.26PS.85 text in blue modified or added by Clerke (2004)	Grainstones and packstones with less than 15% micrite matrix. Primary rock constituents include abundant micritized skeletal grains and in certain horizons superficial oolites and composite-aggregate grains. Lime grainstones and packstones with primary interparticle porosity modified only slightly by calcite cementation make up most the of the highly permeable 2A zone.	These are packstones and minor boundstones, wackestones and grainstones with generally high porosity and permeability. Important pore types include primary interparticle and intra-particle voids and secondary grain-moldic and micro-leached grain and matrix pores. These limestones are a major component of reservoir zone 2B.	Grainstones, packstones and minor wackestones with greater than 10% *Cladocoropsis* (including their contained pores). The finer-grained matrix contains abundant micritized skeletal grains. These limestones generally have high primary porosities and permeabilities.	Grainstones and packstones with less than 15% micrite matrix. Primary rock constituents include abundant micritized skeletal grains and in certain horizons superficial oolites and composite-aggregate grains. Lime grainstones and packstones with primary interparticle porosity modified only slightly by calcite cementation make up most of the highly permeable 2A zone.
Depositional Texture	Grainstone, Mud-lean Packstone, Packstone	Mud-lean Packstone, Grainstone, Packstone	Mud-lean Packstone, Grainstone, Packstone, Boundstone	Grainstone, Mud-lean Packstone, Packstone
Major Grain Types	Micritized Grains, Foraminifers (Including Miliolids), Dasycladacean Algae, Ooids, Bivalves	Micritized Grains, *Cladoco-ropsis*, Dasycladacean Algae, Foraminifers (Including Miliolids)	Micritized Grains, Stromatoporoids, Corals, Foraminifers (Including Miliolids)	Micritized Grains, Foraminifers (Including Miliolids), Dasycladacean Algae, Ooids, Bivalves
Minor Grain Types	Echinoderms, Stroma-toporoids, Corals, *Cladoco-ropsis*, Gastropods, Composite Grains, Intraclasts, Ostracodes, Red Algae, Brachiopods	Stromatoporoids, Echino-derms, Bivalves, Corals, Ooids, Gastropods, Brachiopods, Composite Grains, Red Algae	*Cladocoropsis*, Bivalves, Echinoderms, Dasycla-dacean Algae, Intraclasts, Coated Grains, Composite Grains, Gastropods	Echinoderms, Stroma-toporoids, Corals, *Cladoco-ropsis*, Gastropods, Composite Grains, Intraclasts, Ostracodes, Red Algae, Brachiopods
Sedimentary Structures	Cross Bedding, Burrows, Hardgrounds, Fining-upward Graded Beds, Borings, Horz Laminae	Burrows, Hardgrounds, Cross-bedding, Horz Laminae	Burrows, Borings, Hard-grounds, Fining-upward Graded Beds, Cross-bedding	Cross Bedding, Burrows, Hardgrounds, Fining-upward Graded Beds, Borings, Horz Laminae
Pore Types	Interparticle, Moldic, Intraparticle, Intercrystalline, Fracture	Interparticle, Intraparticle, Moldic, Intercrystalline	Interparticle, Moldic, Intraparticle, Intercrystalline, Fracture	Interparticle, Moldic, Intraparticle, Intercrystalline, Fracture
Plug Porosity Range (%)	0.8 - 33.9	4.2 - 31.0	9.0 - 31.4	0.8 - 33.9
Full Core Porosity Range (%)	0.5 - 33.5	9.9 - 31.2	10.2 - 27.7	0.5 - 33.5
Plug Permeability Range (md)	Kh 0.003 - 3743 Kv 0.01 - 2269	Kh 1 - 1515 Kv 0.6 - 1489	Kh 0.3 - 5505 Kv 0.1 - 3535	Kh 0.003 - 3743 Kv 0.01 - 2269
Full Core Permeability Range (md)	Kh 0.01 - 1451 Kv 0.01 - 3368	Kh 0.1 - 1461 Kv 0.01 - 987	Kh 1.2 - 2498 Kv 0.01 - 2152	Kh 0.01 - 1451 Kv 0.01 - 3368
Diagenetic Modification	Leaching and recrystal-lization, isopachous bladed calcite cement, dolomiti-zation,physical compaction, stylolitization, equant calcite cement, kaolinite emplace-ment, anhydrite emplace-ment/replacement, silicification	Leaching and recrystal-lization, dolomitization, equant calcite cement, stylolitization, anhydrite emplacement, silicification	Leaching and recrystal-lization, dolomitization, anhydrite emplacement, stylolitization, isopachous bladed calcite cement, equant calcite cement, pyrite, dedolomitization	Leaching and recrystal-lization, isopachous bladed calcite cement, dolomitization, physical compaction, stylolitization, equant calcite cement, kaolinite emplacement, anhydrite emplacement/ replacement, silicification

See next page for continuation.

APPENDIX 2: ARAB D FACIES

Lithofacies	Bivalve-Coated Grain-Intraclast	Micrite	Burrowed Micrite	Dolomite
Hadley, K., J.C. Wendte, EPR.68ES.77 Mitchell_EPR.26PS.85 text in blue modified or added by Clerke (2004)	These are grainstones and packstones with normally high interparticle porosity and permeability. They occur most commonly in beds up to 5-feet-thick interstratified with finer micritic limestones and dolomites in reservoir zone 3. These limestones generally have erosional bases but transitional upper contacts.	These are mudstones with more than 15% micrite. Secondary leaching of micrite has created moderate porosities and permeabilities in reservoir zone 2. Clerke (2004) separates the micrite from the burrowed micrite. Unburrowed micrite is found about 6' below the following tempestite - Bivalve-Coated Grain-Intraclast.	Extensively burrowed mudstones, wackestones and packstones with more than 15% micrite. Clerke separates the micrite from the burrowed micrite. Burrowed - usually vertically with Thalassinoides burrows. Thalassinoides burrows are commonly filled with subsequent Bivalve-Coated Grain-Intraclast storm deposit material as burrow fill. Hence this facies is a mechanical composite of Bivalve-Coated Grain-Intraclast and Micrite.	Dolomite seen in the Arab-D reservoir of Ghawar field has little if any preserved textural information. Hence, these beds are assumed to have been more micritic than the beds adjacent. Dolomite from Zone 1(a small percentage of the dolomite in the field) is typically very-fine crystalline and mimetically replaces skeletal packstones. Locally dolomite replaces *Cladocoropsis* packstone, leaving a low permeability matrix with large and commonly touching molds. Note that the limestone data in this paper comes only from parts of the reservoir with less than 50% dolomite.
Depositional Texture	Packstone, Mud-lean Packstone, Grainstone, Wackestone	Mudstone	Wackestone, Mudstone, Packstone	Indeterminate
Major Grain Types	Micritized Grains, Bivalves, Coated Grains, Intraclasts, Foraminifers	Micritized Grains	Micritized Grains, Bivalves, Foraminifers (Including Kurnubia), Intraclasts; Composite of micritized grains and other burrow fills (vertical) -mostly from adjacent Bivalve-Coated Grain-Intraclast layers above	Anhedral to Euhedral Dolomite Rhombs
Minor Grain Types	Miliolid Foraminifers, Corals, Stromatoporoids, Dasycladacean Algae, Echinoderms, Gastropods, *Cladocoropsis*		Coated Grains, Miliolid Foraminifers, Dasycladacean Algae, Intraclasts, Ostracodes, Echinoderms, Gastropods, Stromatoporoids, Corals	Relict and Leached Bivalves, *Cladocoropsis*, Stromatoporoids, Intraclasts, Echinoderms, Indeterminate Grains
Sedimentary Structures	Burrows, Hardgrounds, Boring, Fining-upward Graded Beds, Cross-bedding	Wavy Laminae, Horz Laminae	Burrows, Hardgrounds, Wavy Laminae, Horz Laminae, Fining-upward Graded Beds	Relict Burrows?, Hardgrounds?, Carbonaceous?, Laminae
Pore Types	Interparticle, Moldic, Intraparticle, Intercrystalline, Fracture	Interparticle, Intercrystalline, Fracture, Vug?	Interparticle (within burrow fills), Intraparticle, Moldic, Intercrystalline, Fracture, Vug?	Intercrystalline, Moldic, Fracture
Plug Porosity Range (%)	2.2 - 31.4	2.3 - 10.2	0.2 - 18.5 Primary porosities and permeabilities in most of these rocks are very low.	1.0 - 29.7
Full Core Porosity Range (%)	2.1 - 23.3		0.9 - 14.7	1.0 - 28.3
Plug Permeability Range (md)	Kh 0.04 - 1064 Kv 0.04 - 793	Kh avg 0.11	Kh 0.001 - 30 Kv 0.001 - 120	Kh 0.002 - 6682 Kv 0.002 - 5276
Full Core Permeability Range (md)	Kh 0.03 - 1990 Kv 0.01 - 453		Kh 0.01 - 38 Kv 0.01 - 2.7 Kv is greatly enhanced by vertical burrows if filled with Bivalve-Coated Grain-Intraclast	Kh 0.01 - 2938 Kv 0.01 - 3774
Diagenetic Modification	Leaching and recrystallization, dolomitization, stylolitization, equant calcite cement, anhydrite emplacement, isopachous bladed calcite cement, pyrite	Leaching and recrystallization, dolomitization, stylolitization, anhydrite emplacement, pyrite, silicification, equant calcite cement, kaolinite	Leaching and recrystallization, dolomitization, stylolitization, anhydrite emplacement, pyrite, silicification, equant calcite cement, kaolinite	Dolomitization, leaching, anhydrite emplacement, equant calcite cement, stylolitization, kaolinite, dedolomitization

(Continued).

APPENDIX 3: DATA BASE (Excel Spreadsheet available from the author)

Well	Permeability to Air (md)	Helium Porosity (%)	Grain Density (g/cm³)	Facies Limestone Unless Noted	Archie Rock Type	Lucia Rock Type	Phi	Permeability Klinkenberg	Thomeer Permeability	G1	P_d1	B_v1	G2	P_d2	B_v2	G3	P_d3	B_v3	B_v Total	Closure Correction
A	3185.11	28.1	2.729	*Cladocoropsis*	IIIC-C7D20	yLS17T	28.1	3169	2675.508	0.48	1.56	25.12	0.53	197.3	3.97				29.08	0.60
A	2034.60	26.0	2.702	*Cladocoropsis*	IIIC-C6D17	yLS16T	26	2022	2740.217	0.53	1.16	20.42	0.65	120.0	5.26				25.68	0.00
A	1965.95	25.5	2.698	*Cladocoropsis*	IIIC-C8D14	yLS15T	25.5	1954	2431.215	0.64	1.34	25.22	0.50	130.0	2.77				27.99	0.14
A	1896.58	23.3	2.754	*Cladocoropsis*	IIIC-C15D6	yLS15T	23.3	1885	1470.815	0.37	1.76	17.93	0.70	100.0	6.28				24.21	0.17
A	1884.77	25.3	2.703	Skeletal Oolitic Below Sequence Boundary	IIIC-C18D5(80%) IIIC-C3D1(20%)	yLS5T(80%) yLS3(20%)	25.3	1885	1739.683	0.14	2.50	14.40	0.16	230.0	10.59				24.99	0.40
A	1796.96	22.0	2.703	Skeletal Oolitic Below Sequence Boundary	IIIC-C17D3	yLS5T	22	1797	2007.795	0.12	2.40	13.40	0.30	210.0	8.64				22.04	0.30
A	1420.75	27.9	2.724	*Cladocoropsis*	IIIC-C20D4	yLS13T	27.9	1411	1145.819	0.33	2.71	22.25	0.49	97.7	6.54				28.79	0.80
A	1147.01	23.4	2.701	Skeletal Oolitic Below Sequence Boundary	IIIC-C18D3	yLS3	23.4	1147	1053.698	0.14	2.90	13.00	0.16	210.0	12.01				25.01	0.35
A	878.57	20.9	2.702	Bivalve-Coated Grain-Intraclast	IIIC-C8D10	yLS10T	20.9	879	844.812	0.52	2.14	20.59	0.15	1085.3	1.27				21.86	0.50
A	812.05	28.5	2.707	*Cladocoropsis*	IIIMC-C20D5	YLS8T	28.5	805	763.827	0.44	3.39	27.60	0.43	130.0	4.33				31.92	0.70
A	810.94	26.7	2.702	Skeletal Oolitic Below Sequence Boundary	IIIC-C12D10	yLS10T	26.7	811	838.239	0.94	1.58	22.50	0.11	280.0	5.40				27.90	0.49
A	782.92	27.5	2.696	*Cladocoropsis*	IIIC-C10D7	yLS13T	27.5	776	798.113	0.57	2.40	23.99	0.90	36.0	7.40				31.39	1.17
A	317.79	29.2	2.700	*Cladocoropsis*	IIIMC-C10D7	yLS10T	29.2	314	290.982	0.42	6.12	29.99	0.20	140.0	1.26				31.25	1.80
A	246.81	24.8	2.748	Stromatoporoid-Red Algae-Coral	IIIC-C10D5	yLS12	24.8	243	93.720	0.50	5.60	17.50	0.15	175.0	6.80				24.30	1.50
A	171.81	26.4	2.841	Skeletal Oolitic Above Sequence Boundary Dolomite	III-IC16D3	nLS15	26.4	169	242.144	0.19	9.43	25.28							25.28	1.45
A	166.71	24.2	2.715	Stromatoporoid-Red Algae-Coral	II-C1D5 IIIC-C8D5	nMS2 (30%) yLS5T(70%)	24.2	164	118.569	0.55	4.99	18.69	0.16	172.7	6.60				25.29	1.38
A	160.78	25.1	2.849	Skeletal Oolitic Above Sequence Boundary Dolomite	(III-I)-C11D3	nLS10T	25.1	158	218.909	0.26	8.37	25.68	1.00	3600.0	2.31				28.00	1.50
A	156.75	25.9	2.841	Skeletal Oolitic Above Sequence Boundary Dolomite	(III-I)-C13D3	nLS12	25.9	154	223.005	0.18	10.12	24.86							24.86	1.27
A	145.38	29.5	2.704	*Cladocoropsis*	IIIMC-C10D15	yLS8T	29.5	143	128.927	0.57	7.00	28.00	0.80	40.0	5.00	0.40	130	2.00	35.00	0.80
A	143.31	25.4	2.848	Skeletal Oolitic Above Sequence Boundary Dolomite	(III-I)-C11D3	nLS10T	25.4	141	223.782	0.27	8.97	28.65	1.00	3400.0	1.70				30.35	1.50
A	94.62	24.8	2.845	Skeletal Oolitic Above Sequence Boundary Dolomite	(III-I)-C8D2	nLS8	24.8	92.6	106.821	0.32	10.32	25.45	1.00	3800.0	1.82				27.27	1.06
A	79.97	23.9	2.718	Stromatoporoid-Red Algae-Coral	II-IIIMC-C4D11	yLS7	23.9	78	90.673	0.57	3.40	11.41	0.10	145.0	12.19				23.60	0.70
A	73.17	21.9	2.840	Skeletal Oolitic Above Sequence Boundary Dolomite	I-C11D3	nLS13	21.9	71.5	87.315	0.25	11.91	22.77							22.77	1.36
A	53.29	21.9	2.864	Skeletal Oolitic Above Sequence Boundary Dolomite	I-C9D3	nLS12	21.9	51.8	88.836	0.14	15.11	20.08							20.08	2.05
A	44.73	17.1	2.738	Stromatoporoid-Red Algae-Coral	IIIMC-C4D7	yLS5T	17.1	43.4	6.942	0.88	5.00	6.20	0.09	240.0	10.24				16.44	1.00
A	44.31	23.0	2.702	Bivalve-Coated Grain-Intraclast	IIIC-C12D7	yLS3	23	44.3	26.850	0.35	13.50	17.80	0.14	280.0	6.64				24.44	0.70
A	26.38	16.8	2.880	Skeletal Oolitic Above Sequence Boundary Dolomite	I-C7D2	nLS9	16.8	25.4	29.713	0.29	11.36	13.80							13.80	2.00
A	21.68	20.7	2.710	Stromatoporoid-Red Algae-Coral	II-C2D10	nLS7	20.7	20.8	49.964	0.90	2.58	8.71	0.50	55.0	6.20	0.10	172	7.84	22.75	0.58
A	18.33	23.2	2.704	Skeletal Oolitic Below Sequence Boundary	IIIM-C10	yL0	23.2	18.3	6.941	0.30	20.50	12.40	0.16	210.0	12.09				24.49	1.20
A	12.88	23.7	2.708	Stromatoporoid-Red Algae-Coral	II-IIIMC-C3D6	nMS8	23.7	12.3	6.885	0.44	10.60	8.25	0.15	154.0	15.80				24.05	0.90
A	8.71	23.8	2.714	Stromatoporoid-Red Algae-Coral	II-C2D4	nMS3	23.8	8.19	1.104	0.35	40.00	10.69	0.07	191.3	13.55				24.24	1.60
A	7.34	21.4	2.721	Stromatoporoid-Red Algae-Coral	IIIMC-C5D1	nMLS3	21.4	6.85	1.083	0.35	40.00	10.50	0.15	155.0	12.00				22.50	1.65
A	4.78	3.5	2.693	Bivalve-Coated Grain-Intraclast	IIIF-B1	nMS1	3.5	4.78	0.000	0.20	5431.21	2.10							2.10	0.11
A	0.49	16.2	2.708	Skeletal Oolitic Below Sequence Boundary	IIIM-B2C2	yLS2	16.2	0.491	0.210	0.24	181.12	16.42							16.42	0.40
A	0.25	6.8	2.738	Micrite	IIIF-A	nFL0	6.8	0.249	0.001	0.04	2200.00	3.10							3.10	0.40

A	0.18	6.8	2.740	Skeletal Oolitic Below Sequence Boundary	IIIM-A (90%) IIIM-B1C7D2(10%)	nL0(90%) yLS2(10%)	6.8	0.182	0.083	0.30	12.55	0.84	0.12	310.0	5.08				5.92	0.30
A	0.03	7.4	2.726	Micrite	IIIF-A	nL0	7.4	0.031	0.001	0.12	1600.00	5.40							5.40	0.52
A	0.03	9.1	2.710	Micrite	IIIF-A	nFL0	9.1	0.026	0.001	0.12	1671.81	4.88							4.88	0.62
A	0.02	6.2	2.710	Bivalve-Coated Grain-Intraclast	IC-C4D1	nLS4	6.2	0.02	0.083	0.64	31.00	3.40	0.14	4100.0	0.71				4.11	0.44
A	0.02	8.2	2.711	Micrite	IIIF-A	nL0	8.2	0.017	0.011	0.40	181.91	5.21	0.27	780.0	2.45				7.66	0.23
A	0.00	4.9	2.666	Bivalve-Coated Grain-Intraclast	IIIC-A	nL0	4.9	0.004	0.000	0.65	240.00	2.00	0.28	2567.2	1.19				3.19	0.50
A	0.00	6.4	2.713	Micrite	IIIF-A	nL0	6.4	0.003	0.001	0.15	1190.39	5.59							5.59	0.36
A	0.00	4.5	2.708	Bivalve-Coated Grain-Intraclast	III(F-C)-A	nL0	4.5	0.002	0.000	0.21	964.88	3.19							3.19	0.42
A	0.00	5.2	2.742	Micrite	IIIF-A	nL0	5.2	0.002	0.001	0.07	1715.20	3.31							3.31	0.26
A	0.00	5.9	2.753	Micrite	IIIF-A	nL0	5.9	0.001	0.000	0.08	2382.07	1.96							1.96	0.22
A	0.00	2.2	2.682	Bivalve-Coated Grain-Intraclast	IIIC-A	nL0	2.2	0.000	0.000	0.05	12000.00	0.12							0.12	0.19
A	0.00	1.5	2.711	Micrite	IIIF-A	nL0	1.5	0.000	0.000	0.54	7852.33	0.73							0.73	0.13
A	0.00	2.0	2.734	Micrite	I(F-C)-A	nL0	2	0.000	0.000	0.12	11400.00	0.25							0.25	0.18
B	-	19.1	2.709	Skeletal Oolitic Below Sequence Boundary	IIIC-C17D4	yLS6T	19.1	N\A	357.884	0.60	2.01	13.85	0.32	225.0	3.00	0.45	640	2.80	19.65	0.60
B	4142.95	20.6	2.706	Skeletal Oolitic Below Sequence Boundary	IIIC-C11D8	yLS8T	20.6	4053	2863.946	0.10	2.10	12.40	0.26	180.0	5.64	0.14	1400	2.50	20.54	0.60
B	3700.23	20.3	2.705	Skeletal Oolitic Below Sequence Boundary	IIIC-C12D6	yLS10T	20.3	3681	1523.725	0.30	1.50	13.44	0.80	145.0	5.00	0.62	820	3.89	22.33	0.00
B	3291.47	21.9	2.705	Skeletal Oolitic Below Sequence Boundary	IIIC-C10D7	yLS7T	21.9	3212	2281.382	0.16	1.90	13.70	0.51	150.0	6.27	0.19	1100	2.90	22.87	0.45
B	3250.11	21.8	2.700	Skeletal Oolitic Below Sequence Boundary	IIIC-C10D7	yLS7T	21.81	3171	2461.301	0.12	2.20	13.60	0.56	110.0	7.61	0.28	1000	1.89	23.10	0.80
B	3108.61	20.6	2.706	Bivalve-Coated Grain-Intraclast	IIIC-C10D7	yLS7T	20.57	3032	2281.382	0.16	1.90	13.70	0.30	170.0	5.49	0.11	1800	1.65	20.84	0.26
B	2630.98	21.1	2.707	Skeletal Oolitic Below Sequence Boundary	IIIC-C14D5	yLS8T	21.1	2616	1250.627	0.23	2.18	14.85	1.00	90.0	7.00	0.40	740	2.07	23.92	0.70
B	2332.89	20.8	2.705	Skeletal Oolitic Below Sequence Boundary	IIIC-B1C10D7	yLS7T	20.8	2271	1251.083	0.14	2.60	12.70	0.27	117.4	6.00	0.06	2500	2.04	20.74	0.80
B	2206.47	21.8	2.705	Skeletal Oolitic Below Sequence Boundary	IIIC-C15D4	yLS5T	21.8	2193	1695.254	0.29	1.64	15.21	0.70	55.0	5.06	0.55	580	3.50	23.76	0.13
B	2179.32	21.6	2.705	Skeletal Oolitic Below Sequence Boundary	IIIC-C17D2	yLS6T	21.6	2166	1641.490	0.26	1.67	14.08	1.00	80.0	6.60	0.70	620	3.00	23.68	0.16
B	2169.43	21.7	2.705	Skeletal Oolitic Below Sequence Boundary	IIIC-C15D4	yLS4T	21.7	2169.43	1585.246	0.29	1.99	17.73	0.48	177.0	3.47	0.51	798	3.20	24.40	0.06
B	1729.41	28.0	2.708	Stromatoporoid-Red Algae-Coral	IIIMC-C20D8	yLS8T	28	1719	1595.143	0.43	2.10	24.48	0.76	65.0	6.55				31.04	0.80
B	1651.93	27.4	2.715	*Cladocoropsis*	IIIC-C15D10	yLS10T	27.4	1641	2667.980	0.45	1.49	23.07	0.36	178.0	5.04				28.11	0.16
B	1544.64	20.8	2.708	Skeletal Oolitic Below Sequence Boundary	IIIC-C15D3	yLS4T	20.8	1534	840.404	0.22	2.31	12.41	0.60	150.0	5.50	0.70	570	3.00	20.91	0.60
B	1246.41	18.8	2.698	Skeletal Oolitic Below Sequence Boundary	III(M-C) - B1C10D6	yLS6T	18.77	1203	965.619	0.16	2.71	12.70	0.40	740.0	6.30				19.00	0.80
B	1208.54	20.2	2.713	Skeletal Oolitic Below Sequence Boundary	IIIC-B1C9D6	yLS6T	20.2	1165	651.006	0.11	2.80	8.40	0.56	70.0	9.99	0.09	1400	1.53	19.92	1.20
B	858.31	26.1	2.749	*Cladocoropsis*	IIIC-C20D7	yLS9T	26.1	851	1874.399	0.72	1.47	26.17	0.20	150.0	1.02				27.18	0.19
B	696.44	19.1	2.702	Skeletal Oolitic Below Sequence Boundary	IIIC-C10D5	yLS5T	19.1	690	785.423	0.58	1.76	17.52	0.80	100.0	4.00	1.00	700	4.00	25.52	0.07
B	520.99	30.7	2.709	*Cladocoropsis*	IIIMC-C18D8	yLS8T	30.7	515	668.136	0.74	3.37	36.51							36.51	1.40
B	398.77	20.3	2.712	Bivalve-Coated Grain-Intraclast	IIIC-C-C9D7	yLS9T	20.3	399	472.477	0.39	3.09	18.21	0.16	1157.2	1.42				19.63	1.29
B	382.38	16.8	2.711	Skeletal Oolitic Below Sequence Boundary	III(M-C)-B3C7D2(70%) III(M-C)-B3C1(30%)	yLS2(70%) nLS1(30%)	16.78	377	119.610	0.22	5.29	10.80	0.60	400.0	6.60				17.40	0.64
B	298.20	29.3	2.714	*Cladocoropsis*	IIIMC-C18D7	yLS7T	29.3	294	566.345	0.54	3.88	31.37	0.20	225.0	2.32				33.69	1.50
B	218.36	24.0	2.711	Stromatoporoid-Red Algae-Coral	I-D3 IIIM-C15D5	nFS2 (20%) yLS5T (80%)	24	215	332.817	0.62	3.40	23.08	0.33	169.0	5.83				28.91	0.82
B	186.93	20.0	2.702	Bivalve-Coated Grain-Intraclast	IIIC-B2C10D3	yLS3	20.04	183	201.975	1.40	2.40	21.88	0.10	300.0	2.20				24.09	1.60
B	182.54	32.8	2.718	*Cladocoropsis*	IIIM-C18D5	yLS5T	32.8	180	147.600	0.47	7.80	29.35	0.18	215.5	4.28				33.63	1.80
B	128.42	28.1	2.716	*Cladocoropsis*	II-D5 IIIMC-C17D5	nFS5 (25%) yLS5T (75%)	28.1	126	333.783	0.42	4.00	21.00	0.30	44.4	7.00	0.15	210	4.50	32.50	0.34
B	111.25	27.6	2.707	*Cladocoropsis*	IIIM-C15D3	yLS3T	27.6	109	68.778	0.36	9.30	20.00	0.43	28.0	4.00	0.28	175	4.80	28.80	1.20
B	83.59	14.6	2.698	Bivalve-Coated Grain-Intraclast	IIIC-C10D3 (70%) IIIC-B2(30%)	yLS10(70%) nLS2(30%)	14.6	83.6	62.306	0.62	3.83	11.26	0.18	2331.6	2.07				13.32	0.40
B	75.86	27.9	2.706	Stromatoporoid-Red Algae-Coral	(II-III)-C7D12	yLS7T	27.9	74.1	44.845	0.60	11.00	26.85	0.30	190.0	4.63				31.49	2.80
B	67.54	14.3	2.709	Bivalve-Coated Grain-Intraclast	IIIC-C7D3	yLS4	14.3	67.5	49.982	0.83	4.00	12.80	0.19	1000.0	1.76				14.56	0.74
B	59.12	29.2	2.710	Stromatoporoid-Red Algae-Coral	IIIMC-C10D12	yLS10T	29.2	57.6	533.833	1.38	0.94	13.78	0.40	35.0	22.00				35.78	0.20
B	38.73	23.9	2.715	Stromatoporoid-Red Algae-Coral	(II-III)-C7D9	nFS3 (40%) yLS7T (60%)	23.9	37.5	20.853	0.20	18.00	3.49	0.52	30.0	24.00	0.20	140	2.00	29.49	2.20
B	30.77	18.2	2.707	Bivalve-Coated Grain-Intraclast	IIIC-C7D4	yLS7	18.2	30.8	4.092	0.59	4.50	3.30	0.80	18.0	9.50	0.32	115	6.50	19.30	0.70

Well	Permeability to Air (md)	Helium Porosity (%)	Grain Density (g/cm³)	Facies Limestone Unless Noted	Archie Rock Type	Lucia Rock Type	Phi	Permeability Klinkenberg	Thomeer Permeability	G1	P_d1	B_v1	G2	P_d2	B_v2	G3	P_d3	B_v3	B_v Total	Closure Correction
B	30.36	16.9	2.717	Skeletal Oolitic Below Sequence Boundary	II-D3 IIIC-C9D5	nFS2 (20%) yLS5T (80%)	16.9	29.3	68.066	0.20	2.80	4.04	1.20	25.0	14.00	0.63	170	4.00	22.04	0.36
B	28.25	11.0	2.710	Bivalve-Coated Grain-Intraclast	IIIC-C7D2(70%) IIIC-B3(30%)	yLS2(70%) nFS3(30%)	11	28.2	36.443	1.28	2.99	10.90	0.15	550.0	0.82	0.12	4000	1.20	12.92	0.20
B	11.62	23.6	2.710	Skeletal Oolitic Below Sequence Boundary	(II-III) C-C3D3	yLS4	23.6	11	3.986	0.26	60.00	25.00							25.00	1.60
B	8.06	25.2	2.721	Stromatoporoid-Red Algae-Coral	II-C5D1	nMS3	25.2	7.56	4.217	0.12	107.25	26.90							26.90	0.73
B	7.37	17.5	2.781	Bivalve-Coated Grain-Intraclast	IIIMC-B5C4D5	yLS5	17.5	7.37	4.067	0.70	6.50	5.30	0.35	100.0	11.70				17.00	0.89
B	3.04	17.8	2.741	Stromatoporoid-Red Algae-Coral	II-C3	nMS2	17.8	2.75	1.598	0.15	100.00	17.89							17.89	0.62
B	0.00	3.6	2.694	Micrite	IIIVF-A	nMLO	3.6	0.002	0.000	0.20	6022.99	1.51							1.51	0.21
B	0.00	3.3	2.728	Micrite	IIIVF-A	nLO	3.3	0.001	0.000	0.14	3561.59	1.60							1.60	0.32
B	0.00	3.2	2.763	Micrite	IIIVF-A (80%) IIIF-B1(20%)	nFM0(80%) yL0(20%)	3.2	0.001	0.000	0.13	2034.63	0.40	0.14	6271.2	1.18				1.58	0.37
B	0.00	3.6	2.791	Micrite	IIIF-A	nLO	3.6	0.001	0.000	0.09	2400.00	2.40							2.40	0.21
B	0.00	2.8	2.725	Micrite	IIIVF-A	nLO	2.8	0.001	0.000	0.15	3385.75	1.41							1.41	0.11
B	0.00	3.5	2.728	Micrite	IIIVF-A	nMLO	3.5	0.001	0.000	0.25	5925.67	1.52							1.52	0.08
B	0.00	2.7	2.738	Micrite	IIIVF-A	nLO	2.7	0.001	0.000	0.14	3244.60	1.55							1.55	0.30
B	0.00	2.1	2.705	Micrite	IIIVF-A	nFMO	2.1	0.001	0.000	0.34	11661.41	0.40							0.40	0.21
B	0.00	1.9	2.715	Micrite	IIIVF-A	nFMO	1.9	0.001	0.000	0.23	15007.86	0.37							0.37	0.11
C	1522.10	18.9	2.710	Skeletal Oolitic Below Sequence Boundary	IIIC-C10D6	yLS6T	18.9	1522	1002.172	0.31	1.66	12.20	0.35	80.0	3.55	0.03	2500	2.35	18.10	0.00
C	1493.00	30.3	2.717	Skeletal Oolitic Above Sequence Boundary	IIIC-C14D10	yLS8T	30.3	1479	1566.965	0.48	2.32	28.82	0.16	140.0	3.75				32.57	0.08
C	1168.80	21.9	2.730	Skeletal Oolitic Below Sequence Boundary	IIIC-C15D5	yLS7T	21.9	1169	789.092	0.18	2.62	12.00	0.50	140.0	6.00	0.80	400	4.00	22.00	0.70
C	1027.37	18.4	2.730	Bivalve-Coated Grain-Intraclast	IIIC-C3D13	yLS13T	18.4	1027	244.565	0.44	2.50	11.59	0.25	1400.0	1.70				13.28	1.80
C	1007.00	23.9	2.701	Stromatoporoid-Red Algae-Coral	IIIC-C10D10	yLS12T	23.9	993	1518.116	1.02	1.10	22.29	0.45	120.0	4.98				27.27	0.23
C	1005.00	21.6	2.730	Skeletal Oolitic Below Sequence Boundary	IIIC-C14D5	yLS7T	21.6	1005	673.368	0.30	1.94	11.50	0.30	120.0	6.38	0.80	400	4.67	22.55	0.50
C	935.00	25.2	2.705	*Cladocoropsis*	IIIC-C15D9	yLS10T	25.2	921	1551.072	0.85	1.37	24.80	0.32	130.0	5.65				30.45	0.06
C	903.00	28.1	2.703	Skeletal Oolitic Above Sequence Boundary	IIIC-C10D7	yLS3	28.1	889	824.078	0.30	3.83	25.34	0.30	120.0	7.80				33.13	0.80
C	887.00	28.8	2.729	Stromatoporoid-Red Algae-Coral	IIIC-C10D11	yLS9T	28.8	873	1053.904	0.79	2.11	29.97	0.09	160.0	3.27				33.24	0.80
C	714.00	25.2	2.699	Skeletal Oolitic Above Sequence Boundary	IIIC-C8 D12	yLS7T *Cladocoropsis?*	25.2	701	936.885	0.65	2.36	27.91	0.12	200.0	2.00				29.91	0.40
C	606.00	26.5	2.697	Skeletal Oolitic Above Sequence Boundary	IIIC-C10D6	yLS5T	26.5	593	814.488	0.53	2.56	24.55	0.22	165.0	4.63				29.19	0.38
C	521.00	25.5	2.707	*Cladocoropsis*	IIIC-C14D3	yLS7	25.5	509	822.587	0.69	2.34	26.93	0.09	175.0	2.49				29.42	0.47
C	512.60	18.3	2.740	Skeletal Oolitic Below Sequence Boundary	IIIC-C12D3	yLS4T	18.3	513	452.731	0.31	1.76	8.80	0.20	100.0	6.29	0.32	991	2.78	17.88	0.00
C	460.00	21.4	2.708	Stromatoporoid-Red Algae-Coral	IIIC-C8D12	yLS15T	21.4	449	1238.471	0.94	1.30	22.50	0.08	1200.0	2.10				24.60	0.18
C	328.00	30.4	2.699	*Cladocoropsis*	IIIC-C17D5	yLS7T	30.4	319	424.932	0.52	4.33	29.60	0.09	190.0	4.41				34.01	0.54
C	328.00	26.9	2.711	Stromatoporoid-Red Algae-Coral	IIIC-C8D8	yLS8T	26.9	319	908.928	0.94	1.57	23.23	0.18	530.0	2.48				25.71	0.60
C	185.52	18.4	2.710	Bivalve-Coated Grain-Intraclast	IIIC-C10D5	yLS6T	18.4	186	192.777	0.35	3.39	11.97	0.18	110.0	3.00	0.25	550	4.27	19.25	0.43
C	168.00	25.7	2.709	*Cladocoropsis*	IIIC-C8D12	yLS9T	25.7	163	222.297	0.60	4.80	26.20	0.03	270.0	1.60				27.80	2.16
C	140.19	23.3	2.710	Bivalve-Coated Grain-Intraclast	IIIMC-C10D5	yLS5T	23.3	140	259.801	1.20	2.00	18.66	0.19	140.0	8.04	0.20	500	0.76	27.46	0.75
C	88.00	29.5	2.703	Skeletal Oolitic Above Sequence Boundary	IIIM-B2C7D1	yLS2	29.5	84.7	82.050	0.35	11.68	26.91	0.13	160.0	6.33				33.24	0.57
C	87.77	21.0	2.710	Bivalve-Coated Grain-Intraclast	IIIC-C6D10	yLS10T	21	87.8	56.795	0.50	5.20	12.65	0.15	150.0	1.94	0.18	340	5.00	19.59	2.00
C	80.00	26.9	2.706	*Cladocoropsis*	IIIMC-C10D1	yLS3	26.9	76.9	56.231	0.42	11.04	23.80	0.19	140.0	5.65				29.45	0.94
C	36.20	28.8	2.711	*Cladocoropsis*	IIIMC-C5D2	yLS4	28.8	34.5	28.087	0.38	15.00	21.37	0.10	180.0	9.50				30.87	1.20
C	23.50	28.1	2.716	Skeletal Oolitic Above Sequence Boundary	IIIM-B2C5	yLS2	28.1	22.2	15.940	0.28	22.05	19.30	0.12	160.0	10.83				30.13	0.70
C	16.18	13.0	2.710	Skeletal Oolitic Below Sequence Boundary	IIIC-C6D3	yLS3	13	16.2	15.867	0.48	7.80	9.76	0.30	800.0	3.30				13.06	0.30
C	15.10	26.3	2.720	Skeletal Oolitic Above Sequence Boundary	IIIM-B2C2	yLS1	26.3	14.1	7.448	0.20	40.36	19.30	0.10	195.0	8.98				28.28	0.60

C	9.71	15.6	2.710	Bivalve-Coated Grain-Intraclast	IIIC-C1D10	yLS10	15.6	9.71	50.592	0.90	3.85	13.08	0.09	850.0	2.15				15.24	1.80
C	7.83	16.6	2.714	Stromatoporoid-Red Algae-Coral	IIIC-C4D3	yLS5	16.6	7.1	3.034	0.81	21.85	17.00	0.40	400.0	1.40				18.40	2.10
C	5.42	18.5	2.740	Skeletal Oolitic Below Sequence Boundary	IIIFM-C7D2	yLS3	18.5	5.42	1.859	0.23	70.76	18.70							18.70	1.30
C	0.48	10.5	2.760	Skeletal Oolitic Below Sequence Boundary	IIIF-C3	yLS1	10.5	0.475	0.146	0.20	152.24	10.29							10.29	0.80
C	0.26	3.3	2.710	Micrite	I-A	nF0	3.3	0.257	0.000	0.09	7572.84	2.22							2.22	0.18
C	0.15	7.7	2.740	Bivalve-Coated Grain-Intraclast	IIIC-C3D3(70%) IIIM-C4D1(30%)	yLS3	7.7	0.148	0.350	0.52	35.18	6.90	0.33	682.6	2.00				8.90	1.40
C	0.04	7.5	2.710	Bivalve-Coated Grain-Intraclast	IIIM-B4C2(70%) IA (30%)	yMLS1(70%) nF0(30%)	7.5	0.038	0.014	0.76	77.30	3.84	0.24	853.8	1.04	0.14	6300	0.52	5.40	0.40
C	0.03	6.0	2.710	Micrite	I-A	nF0	6	0.034	0.000	0.10	5995.03	2.30							2.30	0.24
C	0.01	1.7	2.730	Micrite	I-A	nF0	1.7	0.008	0.000	0.02	7800.00	0.20							0.20	0.32
C	0.01	4.1	2.780	Micrite	IIIFM-A	nL0	4.1	0.005	0.003	0.05	820.19	3.22							3.22	0.13
C	0.00	4.8	2.770	Micrite	IIIFM-B1	nMLS1	4.8	0.005	0.001	0.13	892.10	3.93							3.93	0.40
C	0.00	4.8	2.780	Micrite	IIIFM-A	nL0	4.8	0.004	0.001	0.06	1522.94	3.56							3.56	0.58
C	0.00	4.5	2.760	Micrite	(I-III)-A	nM0	4.5	0.003	0.000	0.07	5814.59	2.25							2.25	0.29
C	0.00	4.7	2.760	Micrite	IIIFM-A	nL0	4.7	0.002	0.001	0.10	1500.00	3.82							3.82	0.16
C	0.00	5.3	2.730	Micrite	IIIF-A	nML0	5.3	0.001	0.000	0.14	1540.23	1.83	0.04	4400.0	1.78				3.61	0.13
D	1066.98	30.7	2.705	Skeletal Oolitic Above Sequence Boundary	IIIC-C20 D5	YLS5T	30.7	1047	1005.623	0.37	2.87	23.83	0.07	180.0	8.12				31.95	0.70
D	969.65	23.9	2.704	Stromatoporoid-Red Algae-Coral	IIIC-C7D14	yLS14T	23.9	948	755.636	0.75	1.33	15.50	0.20	220.0	4.79	0.20	800	1.00	21.29	0.27
D	687.92	24.9	2.704	Stromatoporoid-Red Algae-Coral	IIIC-C7D14	yLS12T	24.9	671	1216.396	0.98	1.17	20.60	0.12	200.0	6.60				27.20	0.19
D	645.24	23.8	2.713	*Cladocoropsis*	IIIIC-C15D4	yLS10T	23.8	630	621.844	0.45	2.47	18.50	0.15	170.0	6.55				25.05	0.80
D	645.18	27.9	2.704	Skeletal Oolitic Above Sequence Boundary	IIIC-C12D7	YLS7T	27.9	630	703.466	0.63	2.72	27.33	0.04	220.0	3.61				30.93	0.78
D	640.81	27.9	2.716	Skeletal Oolitic Above Sequence Boundary	IIIMC-C16	yLS5	27.9	626	388.227	0.41	4.08	22.57	0.10	200.0	7.43				30.00	0.60
D	540.30	21.2	2.691	*Cladocoropsis*	IIIC-C14D4	yLS8T	21.2	526	340.023	0.45	3.10	17.20	0.08	240.0	3.36				20.56	1.20
D	503.78	25.9	2.705	Stromatoporoid-Red Algae-Coral	IIIC-C7D11	yLS10T	25.9	490	860.772	0.72	1.90	22.93	0.06	240.0	4.06				26.99	0.70
D	461.04	21.0	2.825	Skeletal Oolitic Below Sequence Boundary Dolomite	IIIM-C15D1	yLS1	21	461	975.249	0.10	5.11	17.62							17.62	0.50
D	453.85	16.2	2.715	Skeletal Oolitic Below Sequence Boundary	IIIC-C11D	yLS3T	16.2	454	322.176	0.49	2.29	13.16	0.50	80.0	3.23				16.38	0.09
D	432.20	24.9	2.700	Skeletal Oolitic Above Sequence Boundary	IIIMC-C14	yLS2	24.9	420	339.575	0.53	4.46	27.45							27.45	0.60
D	409.69	23.0	2.705	Bivalve-Coated Grain-Intraclast	IIIC-C13D7	yLS5	23	398	262.175	0.35	3.85	15.81	0.21	170.0	7.50				23.31	0.83
D	346.40	21.6	2.711	*Cladocoropsis*	IIIC-C10D7	yLS7	21.6	335	346.962	0.57	2.79	18.21	0.10	220.0	4.69				22.90	0.67
D	311.27	20.4	2.706	*Cladocoropsis*	IIIC-C10D4	yLS6	20.4	301	231.773	0.41	3.55	15.30	0.12	180.0	5.50				20.80	0.85
D	296.46	26.9	2.700	Skeletal Oolitic Above Sequence Boundary	IIIMC-C14	yLS2	26.9	287	174.019	0.23	7.01	17.95	0.15	180.0	10.50				28.45	0.60
D	268.84	29.4	2.704	Skeletal Oolitic Above Sequence Boundary	IIIMC-C13	yLS4	29.4	260	149.334	0.45	7.10	26.09	0.10	220.0	4.70				30.79	0.68
D	216.94	27.8	2.709	*Cladocoropsis*	IIIMC-C7D15	yLS15	27.8	209	80.219	1.10	3.80	18.59	0.06	170.0	11.59				30.17	2.50
D	211.12	21.2	2.708	*Cladocoropsis*	IIIC-C8D4	yLS4	21.2	203	117.461	0.51	4.50	16.00	0.12	180.0	5.59				21.59	0.93
D	203.09	23.3	2.707	Stromatoporoid-Red Algae-Coral	IIIC-C7D9	yLS10T	23.3	195	145.186	0.69	3.59	17.24	0.50	170.0	3.00	0.35	700	1.50	21.74	2.20
D	158.14	17.6	2.822	Skeletal Oolitic Below Sequence Boundary Dolomite	IIIM-C8D5	yLS5	17.6	158	145.904	0.35	3.60	11.00	0.30	28.0	5.83				16.83	1.36
D	135.16	25.2	2.678	*Cladocoropsis*	IIIMC-C9D2	yLS3	25.2	129	78.976	0.38	8.37	20.00	0.02	240.0	6.20				26.20	1.30
D	132.48	25.1	2.709	Stromatoporoid-Red Algae-Coral	IIIC-C3D17	yLS15	25.1	126	457.501	1.09	1.80	20.92	0.20	214.7	1.52	0.20	800	1.50	23.94	1.50
D	128.95	18.0	2.710	Skeletal Oolitic Below Sequence Boundary	IIIC-C7D7	yLS7	18	129	109.863	0.42	3.60	10.81	0.25	180.0	5.61	0.30	1000	1.00	17.42	0.80
D	115.85	25.1	2.705	*Cladocoropsis*	IIIMC-C8D6	yLS4	25.1	110	72.281	0.65	5.20	17.00	0.06	95.0	4.00				21.00	1.20
D	113.79	25.8	2.706	Stromatoporoid-Red Algae-Coral	IIIMC-C7D7	yLS7T	25.8	108	161.489	0.53	5.42	23.10	0.04	210.0	5.55				28.65	0.95
D	108.87	16.0	2.708	Bivalve-Coated Grain-Intraclast	IIIC-C7D3	yLS3T	16	109	121.393	0.59	3.00	11.94	0.44	135.7	2.50	0.30	1200	1.50	15.94	0.72
D	105.24	25.8	2.701	Stromatoporoid-Red Algae-Coral	IIIMC-C7D9	yLS9T	25.8	100	120.400	0.60	6.70	26.80	0.08	260.0	1.60				28.40	2.50
D	57.51	13.4	2.711	Skeletal Oolitic Below Sequence Boundary	IIIC-C5D3	yLS3	13.4	57.5	46.696	0.45	4.56	9.32	0.45	700.0	2.60				11.92	0.91
D	45.86	14.2	2.702	Bivalve-Coated Grain-Intraclast	IIIC-C5D6	yLS6	14.2	45.9	45.204	0.28	1.71	2.53	0.59	4.1	8.53	0.32	1300	2.40	13.46	0.05
D	28.13	26.6	2.699	Skeletal Oolitic Above Sequence Boundary	IIIMC-B5C10(70%) IIA(30%)	yLS2 (70%) nMO (30%)	26.6	25.7	13.489	0.49	16.50	19.30	0.05	240.0	9.00				28.30	0.90
D	25.68	17.6	2.714	*Cladocoropsis*	IIIC-C7	yLS2	17.6	23.4	5.617	0.55	23.00	18.75							18.75	1.40
D	24.16	15.8	2.697	Bivalve-Coated Grain-Intraclast	IIIC-C3D8	yLS8	15.8	24.2	19.374	0.34	3.33	3.66	1.11	7.2	11.27	0.06	3400	0.90	15.83	0.38

Well	Permeability to Air (md)	Helium Porosity (%)	Grain Density (g/cm³)	Facies Limestone Unless Noted	Archie Rock Type	Lucia Rock Type	Phi	Permeability Klinkenberg	Thomeer Permeability	G1	P_d1	B_v1	G2	P_d2	B_v2	G3	P_d3	B_v3	B_v Total	Closure Correction
D	13.20	23.9	2.711	Stromatoporoid-Red Algae-Coral	(II-III)MC-C5D5	yLS2	23.9	11.7	4.540	0.45	14.00	9.00	0.08	220.0	15.30				24.30	1.10
D	11.84	16.9	2.707	Skeletal Oolitic Below Sequence Boundary	IIIC-C7D2	yLS2	16.9	11.8	3.627	0.55	12.75	8.36	0.16	180.0	8.87				17.22	1.05
D	9.77	19.8	2.702	Stromatoporoid-Red Algae-Coral	IIIC-C2D15	nLS15	19.8	8.48	15.110	1.12	7.38	15.86	0.12	1200.0	1.70				17.56	2.66
D	0.37	9.8	2.823	Skeletal Oolitic Below Sequence Boundary Dolomite	IIIM-C4D1	yLS1	9.8	0.368	1.072	0.65	13.82	5.50	0.28	140.0	2.20				7.70	0.94
D	0.25	11.9	2.710	Skeletal Oolitic Above Sequence Boundary	(II-III) - A	nMO	11.9	0.15	0.074	0.16	267.90	11.13							11.13	0.17
D	0.04	10.1	2.708	Bivalve-Coated Grain-Intraclast	IIIC-B2C3	yLS2	10.1	0.041	0.043	0.56	102.93	7.43	0.14	1600.0	1.45				8.88	1.24
D	0.04	4.6	2.755	Micrite	IVF-A	nF0	4.6	0.037	0.000	0.08	4834.92	2.22							2.22	0.32
D	0.02	8.7	2.704	Bivalve-Coated Grain-Intraclast	IIIC-B2C2	nLS2	8.7	0.017	0.030	0.85	67.08	5.30	0.08	3800.0	3.06				8.36	0.37
D	0.01	8.3	2.716	Micrite	(I-III)C-B2	nLS1	8.3	0.012	0.003	0.12	960.30	6.20							6.20	0.90
D	0.01	4.5	2.710	Bivalve-Coated Grain-Intraclast	(I-III)C-B1	nL0	4.5	0.006	0.000	0.36	1770.90	2.03							2.03	0.75
D	0.01	4.6	2.709	Bivalve-Coated Grain-Intraclast	(I-III)C-B1	nF0	4.6	0.005	0.000	0.65	328.98	2.70	0.18	3400.0	0.84				3.53	0.60
D	0.01	6.6	2.722	Micrite	IVF-A	nF0	6.6	0.005	0.002	0.06	1395.84	5.10							5.10	0.23
D	0.00	7.3	2.714	Micrite	IVF-A	nF0	7.3	0.005	0.002	0.05	1654.86	4.94							4.94	0.18
D	0.00	6.5	2.722	Micrite	IVF-A	nF0	6.5	0.004	0.003	0.05	1389.10	4.91							4.91	0.13
D	0.00	5.3	2.722	Micrite	IVF-A	nF0	5.3	0.003	0.001	0.06	1699.18	4.53							4.53	0.15
D	0.00	5.8	2.721	Micrite	IVF-A	nF0	5.8	0.002	0.000	0.20	4798.08	2.72							2.72	0.25
D	0.00	3.9	2.706	Micrite	IVF-A	nF0	3.9	0.002	0.000	0.25	5100.00	2.77							2.77	0.26
D	0.00	3.5	2.703	Micrite	IVF-A	nF0	3.5	0.001	0.000	0.10	7156.41	1.92							1.92	0.16
E	665.03	28.6	2.704	Skeletal Oolitic Above Sequence Boundary	IIIC-C13D10	yLS9T	28.6	650	607.089	0.37	3.51	22.86	0.12	175.0	7.81				30.68	0.41
E	535.39	21.3	2.711	*Cladocoropsis*	IIIC-C10D15	yLS12T	21.3	520	1111.777	0.70	1.32	17.77	0.50	100.0	5.24				23.01	0.18
E	371.19	23.3	2.708	*Cladocoropsis*	IIIC-C13D7	yLS6T	23.3	360	274.037	0.35	3.63	15.25	1.05	21.0	12.33				27.58	0.60
E	352.50	22.6	2.698	Skeletal Oolitic Below Sequence Boundary	III(M-C) - C12D5	yLS5T	22.6	352.5	358.581	0.32	3.35	15.20	0.35	210.0	9.60				24.80	0.69
E	341.05	26.6	2.714	*Cladocoropsis*	IIIC-C11D10	yLS8T	26.6	331	399.004	0.69	3.26	26.09	0.13	170.0	4.55				30.64	0.79
E	325.21	25.9	2.710	Skeletal Oolitic Above Sequence Boundary	IIIC-C9D10	yLS10T	25.9	314	534.044	0.55	3.00	23.94	0.15	155.0	4.01				27.95	0.76
E	268.30	28.5	2.701	Skeletal Oolitic Above Sequence Boundary	IIIC-C10D7	yLS7T	28.5	259	391.510	0.40	4.20	23.13	0.08	190.0	7.05				30.19	0.70
E	124.29	19.9	2.696	Stromatoporoid-Red Algae-Coral	IIIC-C2D7	yLS7T	19.9	118	242.247	0.57	1.88	10.30	1.06	12.0	11.07	0.28	700	1.43	22.80	0.60
E	117.70	27.6	2.699	*Cladocoropsis*	IIIC-C8D12	YLS8T	27.6	112	211.710	0.69	4.63	26.99	0.09	245.0	3.80				30.79	1.40
E	58.50	20.5	2.705	Stromatoporoid-Red Algae-Coral	IIIC-C3D10	yLS10T	20.5	54.7	39.242	0.85	5.28	15.19	0.20	1300.0	1.94				17.13	2.58
E	50.64	24.4	2.699	Stromatoporoid-Red Algae-Coral	IIIC-C4D15	nLS15T	24.4	47.1	187.776	0.86	3.30	20.99	0.33	850.0	2.34				23.33	1.80
E	44.77	20.6	2.708	Skeletal Oolitic Below Sequence Boundary	III(M-C) - C7D4	yLS4T	20.6	44.8	153.561	0.38	4.32	14.40	0.33	200.0	8.80				23.20	0.87
E	39.38	20.3	2.701	Bivalve-Coated Grain-Intraclast	III(M-C)-C5D10	yLS10T	20.3	39.4	95.209	0.93	3.40	16.20	0.20	290.0	6.63				22.83	0.60
E	36.90	20.5	2.718	*Cladocoropsis*	IIIC-C5D5	yLS5T	20.5	34.1	13.282	0.70	10.00	14.72	0.18	130.0	6.93				21.65	1.21
E	32.15	19.3	2.698	Skeletal Oolitic Below Sequence Boundary	III(M-C) - C5D9	yLS9T	19.3	32.2	35.328	0.26	3.50	4.39	0.56	7.4	11.38	0.13	1100	2.48	18.25	0.34
E	25.09	21.7	2.620	Skeletal Oolitic Above Sequence Boundary	IIIC-C6D5	yLS4	21.7	22.8	51.956	0.50	8.17	19.00	0.07	215.0	4.92				23.92	1.28
E	24.91	26.2	2.700	Skeletal Oolitic Above Sequence Boundary	IIIFM-B8C6	yMLS2	26.2	22.7	25.664	0.55	12.27	21.39	0.25	90.0	9.75				31.13	0.57
E	23.66	26.6	2.695	Skeletal Oolitic Above Sequence Boundary	IIIFM-B7C5D1	yMLS2	26.6	21.4	25.879	0.37	22.70	30.49							30.49	1.05
E	22.85	27.8	2.696	Skeletal Oolitic Above Sequence Boundary	IIIFM-B7C5	yMLS1	27.8	20.7	14.858	0.49	20.03	24.65	0.12	210.0	7.33				31.98	0.72
E	14.21	20.3	2.698	Stromatoporoid-Red Algae-Coral	IIIC-C2D12	nLS12	20.3	12.6	172.521	1.05	1.50	10.43	0.80	21.0	10.50	0.25	1200	1.47	22.40	0.37
E	14.09	23.5	2.713	*Cladocoropsis*	IIIMC-B6C5	IIIMC-B6C5	23.5	12.5	7.708	0.35	38.10	26.82							26.82	1.00
E	13.97	28.9	2.701	Skeletal Oolitic Above Sequence Boundary	IIIFM-B8C3	yMLO	28.9	12.3	5.821	0.25	48.00	23.55	0.10	200.0	7.00				30.55	0.80
E	13.87	26.0	2.696	Skeletal Oolitic Above Sequence Boundary	IIIFMB7C5	yMLO	26	12.3	18.262	0.58	17.00	25.89	0.16	220.0	6.67				32.56	0.85
E	11.64	17.5	2.699	Stromatoporoid-Red Algae-Coral	IIIC-C2D10	yLS10	17.5	10.1	44.455	0.94	4.88	16.00	0.10	1600.0	1.97				17.97	1.39
E	10.60	21.9	2.711	Skeletal Oolitic Below Sequence Boundary	IIIM - B5C3D1	yLS3	21.9	10.6	0.928	0.35	15.50	3.80	0.18	55.0	9.63	0.16	200	9.35	22.78	0.24

E	8.37	20.1	2.742	*Cladocoropsis*	IIIC-C3D1	yLS4	20.1	7.18	2.942	0.17	75.01	19.97							19.97	0.80
E	8.36	20.5	2.729	*Cladocoropsis*	IIIMC-C3D1	yLS2	20.5	7.14	2.455	0.37	48.34	19.85							19.85	2.29
E	6.65	19.6	2.703	Stromatoporoid-Red Algae-Coral	IIIC-C1D10	nLS10	19.6	5.61	7.611	1.35	9.50	16.41	0.33	210.0	8.24				24.65	1.50
E	5.76	21.2	2.714	Stromatoporoid-Red Algae-Coral	IIIMC-C4D2	yLS4	21.2	4.86	0.577	0.27	28.84	4.69	0.20	98.1	8.78	0.09	300	8.08	21.55	0.80
E	5.47	23.6	2.705	Skeletal Oolitic Below Sequence Boundary	III(F-M) - B5C2(70%) IIIF-C2(30%)	yLS1(70%) yMS2(30%)	23.6	5.473	0.991	0.42	34.00	9.73	0.12	190.0	14.60				24.33	0.40
E	4.86	20.4	2.718	Skeletal Oolitic Below Sequence Boundary	IIIM - B3C1	yL0	20.4	4.863	1.084	0.31	39.47	9.60	0.12	230.0	12.00				21.60	0.50
E	3.97	15.2	2.705	Bivalve-Coated Grain-Intraclast	IIIC - C3D8	yLS8	15.2	3.971	3.535	0.81	11.27	9.43	0.22	360.0	6.30				15.73	0.77
E	3.56	17.3	2.697	Bivalve-Coated Grain-Intraclast	IIIC - C2D10	yLS10T	17.3	3.562	20.960	0.80	6.92	14.00	0.12	1000.0	1.94				15.94	0.61
E	2.75	18.0	2.704	Stromatoporoid-Red Algae-Coral	IIIC-C1D2	nLS3	18	2.13	0.158	0.42	35.00	4.00	0.12	350.0	13.70				17.70	1.00
E	2.52	20.3	2.726	Skeletal Oolitic Below Sequence Boundary	IIIM - B3C1	yLS1	20.3	2.523	0.888	0.12	165.00	19.38							19.38	1.34
E	2.44	18.3	2.700	Stromatoporoid-Red Algae-Coral	IIIC-C1D2	nLS3	18.3	1.86	0.291	0.22	183.46	18.65							18.65	1.80
E	2.30	15.2	2.741	*Cladocoropsis*	IIIC-C1D1	nLS2	15.2	1.75	0.957	0.17	97.40	15.15							15.15	0.47
E	2.14	12.5	2.756	*Cladocoropsis*	IIIC-C2D5	yLS3	12.5	1.63	0.534	0.28	73.64	11.80							11.80	1.20
E	1.11	9.9	2.705	Bivalve-Coated Grain-Intraclast	IIIC - C2D4	yLS4	9.9	1.107	2.883	1.17	10.63	10.26	0.25	1300.0	0.99				11.24	0.61
E	0.53	15.4	2.701	Bivalve-Coated Grain-Intraclast	IIIC - C5D12	yLS12T	15.4	0.53	384.830	1.10	1.40	15.00	0.38	1000.0	2.64				17.64	0.25
E	0.29	14.9	2.719	Micrite	III(M-C) - B1C1	nLS1	14.9	0.29	0.075	0.24	235.00	12.71							12.71	0.65
E	0.14	8.3	2.797	Micrite	IIIM - B3	nL0	8.3	0.143	0.081	0.12	223.05	7.72							7.72	0.23
E	0.08	12.8	2.704	Micrite	III(F-M) - C4D2	nLS3	12.8	0.075	0.036	0.50	123.47	7.59	0.08	1000.0	4.84				12.43	1.20
E	0.06	8.4	2.724	Skeletal Oolitic Below Sequence Boundary	IIIM - B1C1	yL0	8.4	0.059	0.065	0.77	85.34	9.33							9.33	0.75
E	0.06	10.4	2.728	Micrite	III(M-C) - C1	nL0	10.4	0.055	0.024	0.13	456.33	9.45							9.45	0.54
E	0.03	9.1	2.747	Micrite	IIIM - A	nL0	9.1	0.026	0.007	0.10	666.30	5.84							5.84	0.31
E	0.03	10.6	2.732	Micrite	IIIM - A	nL0	10.6	0.025	0.011	0.07	807.53	7.39							7.39	0.25
E	0.02	4.0	2.701	Micrite	IIIM-A(60%) IIVF-A(40%)	nL0(100%)	4	0.016	0.000	0.22	6357.80	1.87							1.87	0.24
E	0.01	7.9	2.736	Bivalve-Coated Grain-Intraclast	IIIM - A	nL0	7.9	0.012	0.003	0.17	785.20	6.34							6.34	0.39
E	0.01	6.1	2.738	Micrite	IIIC - A	nL0	6.1	0.008	0.000	0.18	1200.00	4.19							4.19	0.29
E	0.00	2.9	2.748	Micrite	III(F-M) - A	nL0	2.9	0.003	0.000	0.07	4113.34	2.26							2.26	0.13
F	-	12.5	2.713	Stromatoporoid-Red Algae-Coral	II-A	nMO	12.5	N|A	0.083	0.36	175.00	13.00							13.00	1.80
F	-	20.0	2.714	Skeletal Oolitic Above Sequence Boundary	IIIMC-B2C2	yLS2	20	N\A	0.832	0.26	46.30	8.81	0.06	250.0	5.03				13.84	1.30
F	-	23.5	2.727	Skeletal Oolitic Above Sequence Boundary	IIIMC-B2C2D2	yLS3	23.5	N\A	3.227	0.30	37.78	15.58	0.04	240.0	8.56				24.14	1.60
F	903.18	23.4	2.701	Skeletal Oolitic Above Sequence Boundary	IIIC-C15D5	yLS5	23.4	885	677.801	0.17	4.20	17.32	0.32	160.0	8.16				25.48	0.55
F	900.04	28.5	2.719	*Cladocoropsis*	IIIC-C16D6	yLS11T	28.5	880	661.039	0.41	2.99	21.67	0.27	175.0	8.38				30.05	0.55
F	670.58	22.2	2.704	Stromatoporoid-Red Algae-Coral	IIIC-C9D11	yLS12T	22.2	655	1208.801	0.60	1.69	21.38	0.70	1100.0	3.00				24.38	0.22
F	603.77	27.0	2.704	Skeletal Oolitic Above Sequence Boundary	IIIC-C13D5	yLS10T	27	589	1344.516	0.45	2.34	25.74	0.15	245.0	4.20				29.93	0.36
F	395.53	25.0	2.701	*Cladocoropsis*	IIIC-C11D5	yLS7T	25	384	279.192	0.76	3.84	27.36	0.08	280.0	1.50				28.86	0.79
F	352.70	26.5	2.699	Bivalve-Coated Grain-Intraclast	IIIC-C9D6	yLS6T	26.7	209	241.136	0.55	4.76	25.32	0.24	180.0	3.79				29.11	0.85
F	276.65	25.0	2.700	Bivalve-Coated Grain-Intraclast	IIIMC-C11D4	yLS3T	25	266	215.808	0.55	4.82	24.36	0.13	210.0	3.74				28.10	0.80
F	246.90	28.4	2.707	Skeletal Oolitic Above Sequence Boundary	IIIC-C11D6	yLS6	28.4	238	423.251	0.69	3.43	28.12	0.09	145.0	5.07				33.19	0.80
F	223.71	25.4	2.704	*Cladocoropsis*	IIIMC-C9D2	yLS4	25.4	215	151.602	0.38	5.59	18.41	0.07	220.0	7.06				25.47	0.51
F	220.19	14.1	2.701	Stromatoporoid-Red Algae-Coral	III(M-C)–C8D3	yLS5T	14.1	220	28.094	0.20	14.00	13.00	0.57	130.0	4.54				17.54	0.35
F	217.01	26.7	2.699	*Cladocoropsis*	IIIMC-C9D2	yLS3	26.7	209	274.043	0.35	5.73	24.32	0.15	240.0	4.93				29.25	0.71
F	203.69	24.1	2.700	Stromatoporoid-Red Algae-Coral	IIIC-C10D5	yLS10T	24.1	197	265.683	1.02	2.20	18.62	0.13	155.0	10.30				28.92	0.29
F	198.29	22.1	2.699	Stromatoporoid-Red Algae-Coral	IIIC-C8D8	yLS9T	22.1	191	310.686	0.87	2.27	18.70	0.18	180.0	6.65				25.35	0.60
F	148.83	9.1	2.697	Bivalve-Coated Grain-Intraclast	III(M-C) - C4D10	yLS10T	19.1	149	281.205	0.69	2.42	16.21	0.81	130.0	2.00	0.60	800	2.00	20.21	0.89
F	145.25	20.2	2.714	*Cladocoropsis*	IIIC-CC8D7	YLS7T	20.2	139	120.412	0.30	4.43	11.12	0.44	80.0	11.19				22.31	1.00
F	106.41	25.6	2.699	Stromatoporoid-Red Algae-Coral	IIIC-C6D4	yLS3	25.6	101	136.787	0.56	5.89	24.13	0.08	250.0	2.88				27.01	0.92
F	70.10	19.0	2.744	Stromatoporoid-Red Algae-Coral	IIIM-C (20%) I-C10(80%)	nMS10	19	65.4	364.721	0.28	3.20	13.40	0.32	117.5	3.65				17.05	0.40
F	59.66	16.1	2.713	Skeletal Oolitic Below Sequence Boundary	IIIM – B7C4	yLS2	16.1	59.66	25.598	0.19	15.35	13.16	0.40	152.9	3.07	0.50	1000	1.00	17.23	0.50
F	59.11	16.4	2.696	Bivalve-Coated Grain-Intraclast	IIIC – C3D10	yLS10T	16.4	59.1	85.218	0.36	2.42	5.78	0.69	4.4	9.22	0.10	3600	0.69	15.69	0.37

Well	Permeability to Air (md)	Helium Porosity (%)	Grain Density (g/cm³)	Facies Limestone Unless Noted	Archie Rock Type	Lucia Rock Type	Phi	Permeability Klinkenberg	Thomeer Permeability	G1	P_d1	B_v1	G2	P_d2	B_v2	G3	P_d3	B_v3	B_v Total	Closure Correction
F	44.31	19.2	2.710	*Cladocoropsis*	IIIC-C6D3	yLS5	19.2	41.2	33.782	0.58	8.00	16.57	0.15	165.0	4.30				20.87	0.99
F	19.55	19.6	2.707	Skeletal Oolitic Above Sequence Boundary	IIIMC-C5D1	yLS2	19.6	17.6	7.069	0.45	11.00	8.80	0.22	54.7	6.83	0.08	240	4.58	20.22	0.66
F	18.24	14.4	2.712	Skeletal Oolitic Below Sequence Boundary	III(M-C) - C6D2(80%) IIIM-D4(20%)	yLS3(80%) nLS4(20%)	14.4	18.24	10.440	0.50	9.30	9.70	0.24	208.0	4.85				14.55	0.65
F	17.09	20.1	2.709	*Cladocoropsis*	IIIC-C	yLS2	20.1	15.2	9.829	0.70	15.00	19.00	0.10	210.0	3.90				22.90	0.80
F	16.61	21.8	2.726	Stromatoporoid-Red Algae-Coral	IIM-A (20%) IIIC-C5D3(80%)	nMS2(20%) yLS3 (80%)	21.8	14.8	5.825	0.55	13.50	11.21	0.04	240.0	9.02				20.23	1.87
F	13.36	19.8	2.726	Stromatoporoid-Red Algae-Coral	IIIMC-B2C2D5	yLS3	19.8	11.8	4.535	0.55	15.50	11.35	0.05	280.0	8.30				19.65	1.60
F	10.16	12.6	2.710	Skeletal Oolitic Below Sequence Boundary	IIIM – B6C4	yLS4	12.6	10.16	7.564	0.33	17.12	11.61	0.84	1274.1	1.15				12.76	0.29
F	6.69	19.5	2.742	*Cladocoropsis*	IIIMC-C3D1	yMLS2	19.5	5.67	2.434	0.10	110.00	18.30							18.30	1.50
F	6.29	20.8	2.725	Skeletal Oolitic Above Sequence Boundary	IIIFM-B3C1	nMS1	20.8	5.31	2.365	0.23	52.03	15.39	0.03	270.0	6.36				21.75	0.70
F	4.08	13.0	2.710	Skeletal Oolitic Below Sequence Boundary	IIIM-B5C2D1	yLS2stylo	13	4.075	13.078	0.51	8.24	9.69	0.58	35.9	4.07	0.16	1300	1.08	14.84	0.50
F	4.07	9.5	2.722	Skeletal Oolitic Below Sequence Boundary	III(F-M) – B4C2	yLS1	9.5	4.069	1.161	0.85	16.78	8.32	0.14	360.0	1.11	0.16	1147	1.07	10.50	0.40
F	3.88	15.4	2.734	Bivalve-Coated Grain-Intraclast	IIIC – B3D2	yLS4	15.4	3.875	1.431	0.40	23.32	7.79	0.10	194.6	7.99				15.79	1.30
F	3.82	15.7	2.709	Stromatoporoid-Red Algae-Coral	II-B3C1	nMS1	15.7	3.06	2.389	0.58	18.18	10.01	0.34	120.0	5.89	0.20	1150	1.40	17.30	1.60
F	3.75	16.2	2.718	Stromatoporoid-Red Algae-Coral	IIIC-C3D2	yLS3	16.2	3.01	0.370	0.50	27.00	5.30	0.12	170.0	11.50				16.80	0.82
F	2.07	16.5	2.725	Stromatoporoid-Red Algae-Coral	IIIM-A (60%) I-D10 (40%)	nLS5	16.5	1.57	0.317	0.20	150.00	14.80							14.80	2.64
F	1.22	12.3	2.708	Bivalve-Coated Grain-Intraclast	III(M-C) – B2C2D7	yLS7	12.3	1.216	0.340	0.84	49.05	13.00							13.00	1.30
F	0.87	10.3	2.744	Bivalve-Coated Grain-Intraclast	IIIC – C6D2(60%) IIIC-D2(40%)	yLS4(60%) nLS2(40%)	10.3	0.875	1.016	0.47	24.28	7.55	0.17	180.0	3.07				10.62	0.40
F	0.21	11.8	2.704	Micrite	IIIM – B4C1	nLS2	11.8	0.209	0.589	0.82	35.22	12.14	0.15	1444.4	1.00				13.14	0.30
F	0.14	9.0	2.705	Skeletal Oolitic Below Sequence BoundaryMicrite	IIIM – B3D1	nLS2	9	0.143	0.090	0.26	155.08	9.76	0.34	1200.0	1.20				10.96	0.32
F	0.04	8.5	2.706	Skeletal Oolitic Below Sequence BoundaryMicrite	IIIM – B1	nL0	8.5	0.04	0.017	0.27	271.79	7.53	0.11	1423.1	1.20				8.73	0.18
F	0.02	6.8	2.750	Micrite	III(F-M) – B1	nL0	6.8	0.024	0.010	0.06	800.00	6.30							6.30	0.26
F	0.01	4.5	2.754	Micrite	III(F-M) – A	nL0	4.5	0.006	0.003	0.04	1300.00	4.09							4.09	0.40
F	0.00	3.9	2.738	Micrite	III(F-M) – A	nL0	3.9	0.003	0.000	0.11	2309.95	3.27							3.27	0.26
F	0.00	5.4	2.698	Bivalve-Coated Grain-Intraclast	IIIM – B2	nLS1	5.4	0.003	0.000	0.06	3000.00	4.04							4.04	0.80
F	0.00	2.8	2.761	Micrite	IIIF – A	nL0	2.8	0.003	0.000	0.07	2467.04	2.07							2.07	0.13
G	2390.00	25.1	2.700	Skeletal Oolitic Above Sequence Boundary	IIIMC-C12D10	yLS1ST	25.1	2379	1829.704	0.22	2.76	22.32	1.04	110.0	6.99				29.32	0.34
G	1550.00	30.1	2.711	Stromatoporoid-Red Algae-Coral	IIIMC-C15D13	yLS23T	30.1	1543	2825.645	0.69	1.55	32.97							32.97	0.60
G	1170.00	18.2	2.693	Stromatoporoid-Red Algae-Coral	IIIC-C7D	yLS10T	18.2	1159	948.022	0.33	1.70	12.81	0.92	30.0	5.33	0.06	2800	1.29	19.42	0.11
G	1150.00	26.7	2.694	Skeletal Oolitic Above Sequence Boundary	IIIMC-C15D8	yLS12T	26.7	1142	1018.065	0.31	2.93	21.93	0.10	200.0	6.55				28.48	0.49
G	705.14	15.0	2.691	Skeletal Oolitic Below Sequence Boundary	IIIC – C10D3	yLS6	15	705	499.213	0.16	3.60	12.14	0.20	3300.0	2.10				14.24	0.60
G	393.00	19.1	2.689	Skeletal Oolitic Below Sequence Boundary	IIIC-C8D7	yLS12T	19.1	388	216.624	0.34	3.80	13.99	0.54	57.6	1.79	1.02	585	4.04	19.81	0.50
G	279.00	24.1	2.714	Skeletal Oolitic Above Sequence Boundary	IIIMC-C13D5	yLS10	24.1	275	211.313	0.35	4.27	15.80	0.10	250.0	10.93				26.73	0.83
G	234.00	22.1	2.707	Skeletal Oolitic Above Sequence Boundary	IIIMC-C10D5	yM-LS10	22.1	230	231.373	0.64	4.39	25.41							25.41	0.85
G	203.00	26.4	2.700	*Cladocoropsis*	IIIC-C7D10	yLS10T	26.4	200	249.042	1.12	3.14	27.40	0.10	200.0	2.20				29.60	2.10
G	105.00	25.5	2.684	*Cladocoropsis*	IIIMC-C10D2	yM-LS10	25.5	103	79.701	0.42	8.48	21.76	0.12	185.0	4.27				26.03	0.66
G	98.99	13.8	2.699	Skeletal Oolitic Below Sequence Boundary	IIIC-C5D5	yLS10	13.8	96.9	70.294	0.50	4.11	11.11	0.20	60.0	0.71	0.10	4200	1.20	13.02	0.58
G	97.84	26.6	2.684	*Cladocoropsis*	IIIM-C10	yMS5	26.2	97.5	58.267	0.35	11.46	22.27	0.15	160.0	5.63				27.89	0.84
G	95.34	26.2	2.693	Skeletal Oolitic Above Sequence Boundary	IIIM-C10D3	yM-LS6	26.2	93.3	99.089	0.33	10.27	25.00	0.14	200.0	5.36				30.36	0.85
G	85.10	14.0	2.694	Skeletal Oolitic Above Sequence Boundary	IIIMC-C5D3	yLS7	14	83.2	63.687	0.36	6.10	12.67	0.40	1100.0	2.45				15.12	0.91
G	66.04	21.6	2.686	Skeletal Oolitic Above Sequence Boundary	IIIMC-C10D2	yM-LS5	21.6	64.4	46.499	0.54	9.80	22.71	0.06	240.0	2.40				25.11	1.03

G	65.04	13.8	2.699	Skeletal Oolitic Below Sequence Boundary	IIIC – C6D2	yLS4	13.8	65	44.901	0.20	9.20	10.80	0.30	800.0	3.50				14.30	0.38
G	37.83	28.9	2.695	Skeletal Oolitic Above Sequence Boundary	IIIFM-C2(70%) IIIMC-C12D3(30%)	nM-LS2(70%) yLS5(30%)	28.9	36.7	11.414	0.38	26.65	24.20	0.05	250.0	6.76				30.96	2.10
G	36.48	26.8	2.700	Skeletal Oolitic Above Sequence Boundary	IIIFM-C5D1	yM-LS3	26.8	35.3	26.119	0.32	20.00	24.50	0.09	245.0	6.04				30.54	0.98
G	34.19	25.4	2.693	*Cladocoropsis*	IIIC-C15(60%) IIIMC-C2D2(40%)	yLS10T (60%) yM-LS5 (40%)	25.4	33.1	9.905	0.35	3.00	1.80	0.32	26.6	20.00	0.07	190	5.00	26.80	0.50
G	28.72	24.6	2.693	Stromatoporoid-Red Algae-Coral	IIIC-C5D7	nLS6T	24.6	27.7	36.817	0.73	11.21	28.38							28.38	2.50
G	27.75	19.6	2.698	UNCERTAIN	IIIC-C5D7	yLS7	19.6	26.8	59.077	1.00	3.30	13.00	0.10	140.0	7.20				20.20	1.60
G	26.10	32.0	2.691	*Cladocoropsis*	IIIM-C7D5	yM-LS9	32	25.2	24.750	0.38	20.14	27.01	0.03	280.0	5.92				32.94	1.21
G	25.16	25.1	2.698	Stromatoporoid-Red Algae-Coral	IIIM-C5D5	nM-LS5	25.1	24.2	11.810	0.80	10.00	15.18	0.10	150.0	12.00				27.18	1.60
G	9.81	23.4	2.697	Stromatoporoid-Red Algae-Coral	IIIM-C3D7	nLS8T	23.4	9.27	6.187	0.84	10.00	11.35	0.25	150.0	11.60	0.10	560	1.80	24.75	2.50
G	8.72	22.9	2.695	BAD	IIIC-C3D5	nLS5	22.9	8.17	0.000	0.41	9.37	0.00	0.20	55.5	18.66	0.20	600	1.00	19.66	6.00
G	8.52	8.8	2.650	Bivalve-Coated Grain-Intraclast	IIIC – C2D7	nLS7	8.8	8.52	10.470	0.56	6.85	7.69	0.27	5500.0	0.48				8.16	1.32
G	7.98	24.0	2.702	*Cladocoropsis*	IIIM-C5D1	nM-LS5	24	7.5	1.017	0.15	42.00	6.12	0.11	130.0	16.54				22.67	1.10
G	2.61	17.1	2.710	*Cladocoropsis*	IIIMC-C3D2	nLS3	17.1	2.36	0.662	0.35	75.16	15.54							15.54	2.20
G	2.12	13.9	2.712	Stromatoporoid-Red Algae-Coral	(III-I)MC-C5D2	nMS5	13.9	1.89	1.316	0.85	10.00	5.28	0.36	125.0	7.23	0.08	1700	1.30	13.80	1.00
G	1.29	14.0	2.696	Stromatoporoid-Red Algae-Coral	IIIMC-C2 (50%) IIIC-C2D4	nMS2(50%) yLS5	14	1.13	0.112	0.31	49.92	3.96	0.20	143.3	7.38	0.50	550	1.79	13.13	1.08
G	1.11	9.2	2.702	Bivalve-Coated Grain-Intraclast	IIIC – C1D5	yLS3	9.2	1.112	1.008	1.67	11.29	8.16	0.10	2100.0	1.62				9.78	0.60
G	1.10	17.5	2.697	Stromatoporoid-Red Algae-Coral	IIIM-C2D3	nM-LS2	17.5	0.953	0.283	0.23	62.00	6.34	0.21	165.0	7.71	0.30	625	2.37	16.42	1.80
G	0.71	5.0	2.689	Bivalve-Coated Grain-Intraclast	IIIC – C1D1	nLS1	5	0.709	0.096	0.75	26.00	3.40	0.15	3000.0	1.60				5.00	0.33
G	0.40	10.2	2.706	Micrite	IIIC – A	nL0	10.2	0.401	0.211	0.35	77.91	9.10	0.13	1400.0	1.29				10.39	0.55
G	0.11	7.3	2.694	Bivalve-Coated Grain-Intraclast	IIIC – D3	nLS3	7.3	0.111	0.000	0.37	750.00	1.81	0.05	12000.0	2.05				3.87	1.70
G	0.06	1.4	2.685	Micrite	IVF – A	nL0	1.4	0.062	0.000	0.22	10704.21	0.42							0.42	0.13
G	0.05	7.4	2.682	Bivalve-Coated Grain-Intraclast	IIIC – C3D2(20%) IVF-A(80%)	yLS2(20%) nF0(80%)	7.4	0.047	0.001	0.80	380.00	3.98	0.06	3400.0	2.10				6.08	1.20
G	0.02	4.1	2.678	Micrite	IIIM – A	nL0	4.1	0.022	0.000	0.93	620.25	1.03	0.08	8000.0	0.99				2.02	0.22
G	0.01	6.2	2.734	Skeletal Oolitic Below Sequence Boundary	IIIC – A	nL0	6.2	0.011	0.003	0.32	220.00	2.80	0.20	780.0	2.60				5.41	0.24
G	0.01	6.3	2.700	Bivalve-Coated Grain-Intraclast	IIIC – A	nL0	6.3	0.009	0.004	0.78	218.64	5.66							5.66	0.40
G	0.00	6.6	2.696	Micrite	IIIC – A	nL0	6.6	0.002	0.000	0.12	2200.00	5.20							5.20	1.00
G			2.716	Micrite	IVF – A	nF0	NA	NA	0.000	0.05	5000.00	2.75							2.75	0.80
G			2.688	Bivalve-Coated Grain-Intraclast	(IVF-IIIC) – D3	nFS3	NA	NA	0.088	0.87	36.46	5.05	0.10	5500.0	1.45				6.50	0.68
G			2.681	Bivalve-Coated Grain-Intraclast	IIIC – C5D12	yLS12	NA	NA	47.452	0.62	3.04	7.82	0.21	4600.0	1.02				8.84	0.30
G			2.696	Micrite	(I – III) – A	nL0	NA	NA	0.003	0.14	910.41	6.78							6.78	0.35
G			2.690	Micrite	IVF – A	nL0	NA	NA	0.000	0.12	2900.00	4.12							4.12	0.21
G			2.671	Micrite	IVF – A	nL0	NA	NA	0.000	0.20	10750.00	0.39							0.39	0.13
H	4800.00	25.8	2.680	Bivalve-Coated Grain-Intraclast	IIIC-C10D15	yLS20T	25.8	4800	3998.284	0.49	1.29	26.07							26.07	0.00
H	3600.00	22.8	2.691	Stromatoporoid-Red Algae-Coral	IIIC-C7D12	yLS15T	22.8	3570	1368.832	0.94	1.22	22.19	0.08	254.7	1.55	0.60	700	2.00	25.74	0.15
H	1999.27	17.0	2.673	Skeletal Oolitic Below Sequence Boundary	IIIC – C14D5	yLS9T	17	1999	985.624	0.20	2.00	11.00	0.24	65.0	4.91	0.08	4600	1.16	17.07	0.20
H	1812.30	13.7	2.674	Bivalve-Coated Grain-Intraclast	IIIC–C10D6(80%) IIIF-C1(20%)	yLS12T(80%) nFS1(20%)	13.7	1812	596.436	0.28	1.75	9.38	0.23	2169.9	2.27				11.65	0.10
H	1239.62	15.6	2.676	Skeletal Oolitic Below Sequence Boundary	IIIC–C12D3(80%) IIIC-D3(20%)	yLS4T(80%) nLS3(20%)	15.6	1240	639.223	0.22	2.50	11.80	0.26	90.0	1.48	0.06	5500	1.11	14.39	1.40
H	1186.00	28.2	2.700	*Cladocoropsis*	IIIMC-C15D10	yLS20T	28.2	1176	2537.378	0.75	1.39	29.44	0.15	180.0	2.00				31.44	0.00
H	1014.00	29.3	2.682	Stromatoporoid-Red Algae-Coral	IIIMC-C15D10	yLS17T	29.3	1006	878.031	0.48	3.10	28.75	0.08	245.0	2.48				31.23	1.30
H	526.00	23.6	2.701	Skeletal Oolitic Above Sequence Boundary	IIIMC-C12D8	yLS10	23.6	521	373.278	0.36	4.74	23.76	1.00	85.0	3.00				26.76	0.70
H	514.02	16.0	2.670	Skeletal Oolitic Below Sequence Boundary	IIIC – C11D5	yLS7T	16	514	600.179	0.12	3.80	11.60	0.20	220.0	2.69	0.31	1000	2.82	17.11	0.45
H	498.00	22.2	2.691	*Cladocoropsis*	IIIMC-C15D5	yL-S15T	22.2	492	249.577	0.50	3.63	18.50	0.10	260.0	4.18	0.10	3500	0.50	23.18	0.78
H	450.00	26.9	2.696	Stromatoporoid-Red Algae-Coral	IIIC-C5D15	yLS15T	26.9	445	556.350	0.71	2.74	26.36	0.10	209.8	3.74				30.10	1.60
H	421.00	23.8	2.695	Skeletal Oolitic Above Sequence Boundary	IIIC-C19D2	yLS17T	23.8	417	458.125	0.48	3.59	24.17	0.20	200.0	3.35				27.52	0.80
H	391.00	24.1	2.685	Stromatoporoid-Red Algae-Coral	IIIMC-C5D12	yLS17T	24.1	387	638.416	0.70	2.35	24.03	0.18	211.1	3.06				27.09	0.90
H	319.18	12.1	2.677	Bivalve-Coated Grain-Intraclast	IIIC–C4D10(60%) IIIF-C1D1(40%)	yLS10T(60%) nLS2(40%)	12.1	319	396.555	0.51	1.93	12.53	0.30	2500.0	0.90				13.43	0.21

Well	Permeability to Air (md)	Helium Porosity (%)	Grain Density (g/cm³)	Facies Limestone Unless Noted	Archie Rock Type	Lucia Rock Type	Phi	Permeability Klinkenberg	Thomeer Permeability	G1	P_d1	B_v1	G2	P_d2	B_v2	G3	P_d3	B_v3	B_v Total	Closure Correction
H	316.00	24.2	2.691	Skeletal Oolitic Above Sequence Boundary	IIIMC-C16D2	yLS15T	24.2	312	346.640	0.46	4.26	24.22	0.05	350.0	3.06				27.27	1.50
H	270.00	10.5	2.733	Stromatoporoid-Red Algae-Coral	(III-I)-BCD7	nMS7T	10.5	264	38.935	0.86	1.21	3.51	1.24	20.8	1.89	0.11	1500	1.26	6.65	0.00
H	146.00	24.3	2.694	*Cladocoropsis*	IIIMC-C13D10	yLS10T	24.3	143	128.742	0.73	5.60	26.40	0.10	240.0	2.67				29.07	1.80
H	125.00	23.0	2.690	*Cladocoropsis*	IIIMC-C15D2	yM-LS10T	23	123	103.530	0.85	5.30	24.80	0.08	250.0	1.72				26.52	0.66
H	78.10	24.4	2.693	*Cladocoropsis*	IIIMC-C15D5	yM-LS7	24.4	76.4	56.754	0.50	8.80	21.40	0.08	260.0	4.43				25.83	1.30
H	73.50	23.8	2.691	*Cladocoropsis*	IIIMC-C10D10	yLS7T	23.8	71.8	75.774	0.61	6.00	19.25	0.22	56.0	5.50	0.10	330	2.00	26.75	1.40
H	63.00	28.3	2.700	Stromatoporoid-Red Algae-Coral	IIIM-C3D15	nLS15	28.3	61.4	75.581	0.83	7.49	29.58							29.58	2.60
H	46.80	23.9	2.690	*Cladocoropsis*	IIIMC-C10D5	yM-LS10T	23.9	45.5	14.018	0.49	12.30	14.67	0.25	50.0	8.00	0.15	220	3.40	26.07	2.00
H	33.20	13.6	2.640	Bivalve-Coated Grain-Intraclast	III(M-C) – C4D2	yLS2	13.6	33.2	14.475	0.26	12.09	9.60	0.50	100.0	2.40	0.70	1000	1.97	13.97	0.19
H	31.70	24.9	2.702	Stromatoporoid-Red Algae-Coral	IIIMC-C5D10	nM-LS10	24.9	30.6	30.650	0.55	11.50	21.90	0.05	200.0	3.60				25.50	1.60
H	22.10	19.7	2.691	Skeletal Oolitic Above Sequence Boundary	IIIMC-C10D5	yLS7	19.7	21.2	11.257	0.75	12.50	17.74	0.05	210.0	4.49				22.23	1.30
H	18.60	25.0	2.690	*Cladocoropsis*	IIIMC-C10D5	yM-LS10	25	17.9	4.963	0.30	38.33	19.61	0.03	265.0	4.31				23.92	3.10
H	16.70	16.6	2.667	Skeletal Oolitic Below Sequence Boundary	IIIC – C5D2	yLS3	16.6	16.7	6.162	0.60	14.70	13.30	0.10	240.0	5.23	0.30	1000	1.00	19.53	0.91
H	15.10	23.8	2.714	*Cladocoropsis*	IIIMC-C10D3	yM-LS10	23.8	14.4	3.402	0.40	23.00	11.80	0.08	160.0	12.56				24.36	2.00
H	13.20	22.6	2.701	*Cladocoropsis*	IIIM-C10D1	yMS5	22.6	12.6	6.377	0.37	34.50	23.00	0.05	220.0	3.40				26.40	1.20
H	12.42	26.9	2.646	Skeletal Oolitic Below Sequence Boundary	(IIVF-IIIC) – C5D6	nFS11	26.9	12.4	1.371	0.14	75.11	12.15	0.05	220.0	15.13				27.28	2.60
H	11.41	9.5	2.682	Bivalve-Coated Grain-Intraclast	IIIC – C3D8	yLS8	9.5	11.4	50.719	1.09	2.49	9.62	0.18	2900.0	1.27				10.88	0.85
H	11.40	21.0	2.682	Stromatoporoid-Red Algae-Coral	IIIMC-C7D5	nM-LS10	21	10.8	8.840	0.67	15.00	17.50	0.08	260.0	3.63	0.20	1000	1.00	22.13	1.53
H	2.61	21.1	2.699	Skeletal Oolitic Above Sequence Boundary	IIIFM-C10	yM-LS5	21.1	2.36	1.131	0.27	94.89	21.50							21.50	1.75
H	2.22	20.8	2.715	Stromatoporoid-Red Algae-Coral	IIIMC-C3D3 (50%) II-C3D7(50%)	nM-LS7	20.8	1.99	0.901	0.08	185.00	16.70							16.70	3.60
H	2.15	15.6	2.725	Skeletal Oolitic Above Sequence Boundary	IIIM-BC8D1	yM-LS2	15.6	1.92	0.567	0.30	50.60	8.75	0.10	155.0	4.68				13.42	1.82
H	1.40	15.1	2.687	Skeletal Oolitic Below Sequence Boundary	IIIC – C1D4	nLS4	15.1	1.401	0.769	0.38	73.80	17.35							17.35	0.70
H	1.20	18.6	2.672	Micrite	(II-III)VF – A	nF0	18.6	1.2	0.604	0.19	153.25	20.39							20.39	0.75
H	0.81	17.6	2.680	Micrite	(II-III)VF – A	nF0	17.6	0.814	0.462	0.20	165.35	19.45							19.45	0.50
H	0.79	17.5	2.680	Micrite	(II-III)VF – C1D1	nFS2	17.5	0.794	0.360	0.19	183.25	18.67							18.67	0.56
H	0.63	16.2	2.695	Skeletal Oolitic Above Sequence Boundary	IIIFM-C5	yM-LS3	16.2	0.537	0.899	0.30	59.67	12.92	0.15	269.2	2.51	0.30	1200	1.50	16.94	0.40
H	0.31	8.5	2.688	Skeletal Oolitic Below Sequence Boundary	III(M-C) – D1	nLS2	8.5	0.314	0.058	0.38	120.00	7.80	0.22	1100.0	1.27				9.07	0.90
H	0.11	6.1	2.683	Micrite	IVF – D1	nF0	6.1	0.109	0.001	0.08	1972.70	4.20							4.20	0.75
H	0.08	7.7	2.703	Bivalve-Coated Grain-Intraclast	IIIC – C2D1	yLS1	7.7	0.079	3.161	0.51	12.79	7.44	0.10	320.0	0.95	0.44	1100	0.82	9.21	0.30
H	0.04	8.5	2.686	Skeletal Oolitic Below Sequence Boundary	III(M-C) – D1	nLS1	8.5	0.037	0.014	0.14	360.00	5.80	0.24	1500.0	2.51				8.31	0.70
H	0.02	7.3	2.699	Micrite	IIIM – D1	nLS1	7.3	0.023	0.015	0.06	420.00	4.04	0.30	1150.0	2.73				6.77	0.90
H	0.00	4.2	2.709	Micrite	III(M-C) – A	nL0	4.2	0.002	0.000	0.25	1289.59	1.60	0.06	4700.0	1.41				3.01	0.38
H	0.00	3.3	2.707	Bivalve-Coated Grain-Intraclast	IF – A	nF0	3.3	0.002	0.000	0.36	1000.00	3.06							3.06	0.50
H	0.00	3.7	2.705	Micrite	IVF – A	nF0	3.7	0.000	0.000	0.10	4294.44	3.23							3.23	0.40
H	0.00	3.6	2.728	Micrite	III(F-M) – A	nL0	3.6	0.000	0.000	0.08	3786.73	2.53							2.53	0.27
H	0.00	2.1	2.717	Micrite	IVF – A	nF0	2.1	0.000	0.000	0.25	8167.52	1.02							1.02	0.11
I	7837.33	26.1	2.698	UNCERTAIN	(II-III)-D18	nFS13T	26.1	7802	316.304	0.45	1.60	8.50	0.90	4.5	13.00	0.10	500	4.50	26.00	0.09
I	335.91	27.0	2.705	Skeletal Oolitic Above Sequence Boundary	IIIMC-B6C6D6	yLS10	27	332	247.523	0.35	6.33	25.17	0.19	220.0	3.83				29.01	0.62
I	321.87	24.3	2.698	Skeletal Oolitic Above Sequence Boundary	IIIMC-B10C5D2	yLS5	24.3	318	244.619	0.16	8.77	20.74	0.91	54.3	7.55				28.29	0.68
I	184.18	26.6	2.699	Skeletal Oolitic Above Sequence Boundary	IIIC-B4C5D5	yLS7	26.6	181	175.559	0.50	6.74	28.83	0.19	250.0	3.15				31.98	0.57
I	141.86	28.2	2.720	Stromatoporoid-Red Algae-Coral	I-C3D10	nFS5T	28.2	139	1050.658	0.21	3.43	20.35	0.18	130.0	4.04				24.39	0.63
I	72.89	20.2	2.703	*Cladocoropsis*	IIIMC-C10D3	yLS5T	20.2	71.2	55.564	0.48	6.34	14.84	0.19	175.0	6.71				21.55	0.91
I	58.90	12.3	2.707	Bivalve-Coated Grain-Intraclast	IIIC-C5D6	yLS6T	12.3	56.9	166.215	0.38	3.01	10.54	0.31	1452.6	1.57				12.11	0.22
I	57.80	12.5	2.714	Skeletal Oolitic Below Sequence Boundary	IIIC-B3C10D4	yLS4	12.5	55.8	54.253	0.26	4.97	7.66	1.10	24.6	3.94	0.25	2423	0.99	12.60	0.50

I	51.62	11.1	2.703	Skeletal Oolitic Below Sequence Boundary	IIIC-B3C7D5	yLS5	11.1	49.8	28.136	0.25	5.93	6.38	1.52	20.8	5.43	0.30	1000	1.00	12.81	0.32
I	46.55	23.9	2.735	Stromatoporoid-Red Algae-Coral	II-D10	nFS8	23.9	45.2	29.002	0.82	8.00	19.34	0.08	215.0	6.00				25.34	1.50
I	23.41	19.4	2.706	Bivalve-Coated Grain-Intraclast	III(M-C)-B2C2D6	yLS6	19.4	22.2	57.764	1.31	4.50	21.00	0.10	280.0	2.90	0.10	900	1.00	24.90	0.70
I	23.22	22.4	2.710	Stromatoporoid-Red Algae-Coral	(II-III)-C4D10	nFS10	22.4	22.3	18.806	0.70	7.42	13.00	0.26	77.5	5.44	0.11	740	3.24	21.68	2.02
I	18.39	26.9	2.701	*Cladocoropsis*	IIIMC-B4C4D8	yLS3	26.9	17.6	18.156	0.59	20.00	30.55	0.13	280.0	2.15				32.70	0.84
I	17.33	25.7	2.699	Skeletal Oolitic Above Sequence Boundary	IIIM-B3C2	nLS6	25.7	16.6	6.946	0.30	37.48	22.68	0.14	200.0	4.40				27.08	2.00
I	16.64	11.0	2.719	Bivalve-Coated Grain-Intraclast	IIIC - C3D5	yLS5T	11	15.7	117.278	0.45	1.70	5.55	0.55	5.6	3.44	0.45	990	1.12	10.11	0.05
I	15.61	23.1	2.712	Stromatoporoid-Red Algae-Coral	II-C3D6	nFS5	23.1	14.9	22.986	0.50	4.20	6.50	0.75	16.0	12.80	0.10	280	6.41	25.71	0.80
I	12.33	18.5	2.703	*Cladocoropsis*	IIIC-C5D3	yLS4	18.5	11.7	9.092	0.67	12.25	14.50	0.20	240.0	6.10				20.60	0.97
I	11.70	15.7	2.762	*Cladocoropsis*	(I-II)VF-C7D3	nF-LS10	15.7	11.1	144.446	1.05	1.10	7.00	0.07	115.0	9.20				16.20	0.09
I	8.13	21.3	2.757	*Cladocoropsis*	(II-III)-C1D3	nFS4	21.3	7.64	2.646	0.08	140.00	21.65							21.65	1.60
I	6.69	24.0	2.705	Stromatoporoid-Red Algae-Coral	IIVF-C4D4	nFS8	24	6.23	1.302	0.26	42.00	10.00	0.10	220.0	14.50				24.50	1.03
I	6.17	18.3	2.780	Stromatoporoid-Red Algae-Coral	(II-III)VF-B4C3D3	nFS8	18.3	5.76	17.592	0.40	3.60	4.20	0.10	84.7	14.50				18.70	0.39
I	6.13	17.2	2.703	Skeletal Oolitic Above Sequence Boundary	IIIM-B1C3	nLS2	17.2	5.72	5.719	0.33	32.06	18.78							18.78	0.56
I	5.50	19.9	2.778	Skeletal Oolitic Below Sequence Boundary	III(F-M)-B10C10D2(20%) II-III(VF-M)-B3C3(80%)	yLS2(20%) n(F-L)S3(80%)	19.9	4.99	3.290	0.08	105.00	18.11							18.11	0.95
I	5.45	20.2	2.757	Skeletal Oolitic Below Sequence Boundary	(II-III)VF-M-B3C2D2	n(F-L)S2	20.2	4.95	3.500	0.06	140.00	20.56							20.56	1.50
I	5.33	19.6	2.742	*Cladocoropsis*	(I-II)-D9	nFS9	19.6	4.94	1.990	0.06	150.00	16.61							16.61	1.90
I	4.77	23.4	2.699	Skeletal Oolitic Above Sequence Boundary	IIIM-B1C2	nLS3	23.4	4.38	4.069	0.41	41.83	23.70	0.12	295.0	2.74				26.45	0.25
I	4.70	20.1	2.735	Stromatoporoid-Red Algae-Coral	II-C1D5	nFS3	20.1	4.35	2.789	0.06	150.00	19.66							19.66	1.27
I	4.52	9.2	2.703	Bivalve-Coated Grain-Intraclast	IIIC-B2C6D1	yLS1	9.2	4.07	1.239	0.30	18.00	4.60	0.56	164.1	3.91	0.26	1415	1.10	9.61	0.40
I	4.17	19.9	2.726	*Cladocoropsis*	IIVF-C1D4	nF-L	19.9	3.82	1.222	0.32	85.00	22.52							22.52	0.80
I	4.04	18.0	2.732	Skeletal Oolitic Below Sequence Boundary	(II-III)VF-M - B3C2D3	n(F-L)S3	18	3.53	1.342	0.10	135.00	17.26							17.26	1.31
I	3.45	19.4	2.699	Skeletal Oolitic Above Sequence Boundary	IIIM-B1C1	nLS2	19.4	3.14	3.282	0.34	47.60	21.32							21.32	0.68
I	3.09	22.4	2.686	Skeletal Oolitic Above Sequence Boundary	IIIM-B1C1	nLS1	22.4	2.79	1.076	0.21	98.77	18.50	0.16	225.3	6.04				24.54	0.54
I	2.62	19.9	2.746	Micrite	(II-III)VF-M-B1D1	n(F-L)S1	19.9	2.3	1.286	0.07	191.49	18.41							18.41	1.10
I	2.19	18.0	2.698	Skeletal Oolitic Above Sequence Boundary	IIIM-B1C1	nLS2	18	1.96	2.615	0.34	47.51	19.04	0.25	1150.0	0.83				19.87	0.56
I	2.05	21.3	2.737	*Cladocoropsis*	IIVF-A	nF-L	21.3	1.83	1.367	0.09	158.59	18.80							18.80	0.70
I	0.36	12.6	2.717	Skeletal Oolitic Below Sequence Boundary	IIIF - B2	nM0	12.6	0.279	0.071	0.27	218.79	12.51	0.30	1100.0	1.00				13.51	1.00
I	0.27	9.6	2.706	Skeletal Oolitic Below Sequence Boundary	IIIC-B2C3	yL0	9.6	0.201	2.783	0.60	9.47	5.76	0.38	365.0	5.16				10.92	0.42
I	0.23	9.8	2.730	Bivalve-Coated Grain-Intraclast	II-III(VF-C)-B2	nL0	9.8	0.171	0.062	0.11	352.47	10.34							10.34	0.61
I	0.22	8.8	2.709	Skeletal Oolitic Below Sequence Boundary	III(M-C) - B2	nL0	8.8	0.167	0.015	0.16	360.00	6.60	0.15	1549.9	1.34				7.94	1.20
I	0.19	7.4	2.767	Micrite	(IIVF-IIIM) - A	nL0	7.4	0.14	0.110	0.04	360.93	7.31							7.31	0.26
I	0.16	10.2	2.708	Micrite	(IIVF-IIIM-C)-D2	nLS2	10.2	0.116	0.023	0.16	442.87	10.07							10.07	0.90
I	0.07	7.1	2.716	Bivalve-Coated Grain-Intraclast	(IIVF-IIIM)-D4(60%) IIIC-B2C2(40%)	nLS3	7.1	0.043	0.141	0.63	33.01	4.66	0.31	308.6	1.70	0.04	2200	1.35	7.71	1.15
I	0.02	8.0	2.723	Micrite	(IIVF-IIIF)-A	nM0	8	0.013	0.011	0.07	756.19	6.95							6.95	0.20
I	0.02	5.3	2.787	Micrite	(IIVF-IIIM)-A	nL0	5.3	0.008	0.023	0.05	481.79	5.15							5.15	0.24
I	0.02	4.3	2.787	Micrite	(IIVF-IIIM)-A	nL0	4.3	0.008	0.003	0.09	610.32	3.63							3.63	0.19
I	0.01	6.4	2.768	Micrite	IIVF-IIIM)-A	nL0	6.4	0.003	0.003	0.09	1000.00	5.80							5.80	0.63
I	0.00	6.0	2.722	Micrite	(IIVF-IIIM)-A	nM0	6	0.001	0.000	0.10	3104.12	3.94							3.94	0.00
I	0.00	2.3	2.742	Micrite	(IIVF-IIIF)-A	nM0	2.3	0.001	0.000	0.07	3817.05	2.06							2.06	0.21
J	1272.78	16.1	2.709	Skeletal Oolitic Below Sequence Boundary	IIIC-C12D2	yLS2	16.1	1262	888.818	0.10	3.80	12.50	0.25	2500.0	3.28				15.78	0.45
J	1072.44	14.8	2.703	Bivalve-Coated Grain-Intraclast	IIIC-C8D2(90%) IIIC-D3(10%)	yLS2	14.8	1033	687.305	0.12	2.48	8.10	0.35	65.0	4.04	0.10	5200	1.10	13.24	0.05
J	885.18	14.7	2.703	Skeletal Oolitic Below Sequence Boundary	IIIC-C10	yL0	14.7	876	672.578	0.10	4.09	11.70	0.25	2500.0	2.90				14.60	0.19
J	392.00	21.3	2.705	Skeletal Oolitic Above Sequence Boundary	IIIC-C12D5	yLS10T	21.3	382	358.321	0.33	4.33	20.05	0.90	90.0	3.83				23.88	0.80
J	196.82	10.8	2.699	Skeletal Oolitic Below Sequence Boundary	IIIC-C7	yL0	10.8	193	106.470	0.16	5.20	8.10	0.29	2000.0	1.19				9.29	0.65
J	195.00	21.1	2.711	*Cladocoropsis*	IIIC-C13D2	yLS8T	21.1	189	152.911	0.58	3.50	15.42	0.34	160.0	6.08				21.51	1.00
J	189.00	21.8	2.710	*Cladocoropsis*	IIIC-C13D1	yLS4T	21.8	183	192.884	0.78	3.71	22.37	0.13	250.0	3.84				26.21	0.81
J	115.00	20.5	2.717	Stromatoporoid-Red Algae-Coral	IIIC-C7D12	yLS10T	20.5	111	87.201	1.05	2.76	13.64	0.30	140.0	8.00				21.64	1.50

Well	Permeability to Air (md)	Helium Porosity (%)	Grain Density (g/cm³)	Facies Limestone Unless Noted	Archie Rock Type	Lucia Rock Type	Phi	Permeability Klinkenberg	Thomeer Permeability	G1	P_d1	B_v1	G2	P_d2	B_v2	G3	P_d3	B_v3	B_v Total	Closure Correction
J	99.30	26.2	2.706	BAD	IIIC-C7D17	yLS15T	26.2	95.7	862.479	1.10	1.81	29.08	0.09	300.0	2.43				31.51	0.08
J	98.60	32.4	2.707	Stromatoporoid-Red Algae-Coral	IIIC-C13D10	yLS5T	32.4	95	568.115	0.75	2.40	24.20	0.30	24.0	7.00	0.05	350	3.00	34.20	3.00
J	76.48	24.9	2.710	Skeletal Oolitic Above Sequence Boundary	IIIMC-B3C10D2	yLS7	24.9	73.5	85.012	0.55	7.87	24.96	0.12	215.0	5.69				30.66	0.70
J	63.90	26.5	2.703	*Cladocoropsis*	IIIC-C10D5	yLS7T	26.5	61.3	71.785	0.65	8.36	27.23	0.05	310.0	3.80				31.03	1.20
J	57.70	26.0	2.731	*Cladocoropsis*	IIIMC-B3C5	yLS2	26	55.3	1.509	0.15	132.30	23.50							23.50	0.68
J	47.56	18.4	2.699	Skeletal Oolitic Below Sequence Boundary	IIIM-B5C11	yL0	18.4	45.8	31.196	0.14	16.59	12.80	0.84	99.5	6.70				19.50	0.36
J	41.25	17.9	2.693	Skeletal Oolitic Below Sequence Boundary	IIIM-B5C10	yL0	17.9	39.6	33.756	0.24	13.40	15.40	0.85	120.0	5.44				20.84	0.33
J	33.90	23.3	2.702	*Cladocoropsis*	IIIC-C5D5	yLS5	23.3	32.3	22.507	0.56	10.72	17.70	0.60	56.1	6.00	0.10	270	2.70	26.40	1.00
J	28.60	24.9	2.710	*Cladocoropsis*	IIIC-C2D7 IIIC-C15D5	yLS7 (50%) yLS10T (50%)	24.9	27.2	98.023	0.54	3.91	13.13	0.39	25.4	7.92	0.05	330	8.43	29.48	0.63
J	25.90	23.0	2.706	Stromatoporoid-Red Algae-Coral	IIIC-C7D3	yLS6T	23	24.6	28.025	0.60	5.70	11.00	0.50	30.0	6.50	0.15	250	5.00	22.50	1.40
J	25.40	16.3	2.709	Skeletal Oolitic Above Sequence Boundary	IIIMC-C5	yLS5	16.3	24.1	17.232	0.36	14.90	16.04	0.16	1750.0	1.64				17.68	0.96
J	21.80	24.9	2.723	Stromatoporoid-Red Algae-Coral	IIIMC-B4C4D2	yLS4	24.9	20.6	12.157	0.47	15.00	16.20	0.10	220.0	10.00				26.20	1.20
J	21.34	12.4	2.704	Bivalve-Coated Grain-Intraclast	IIIC-C4D5	yLS5	12.4	20.2	22.362	0.72	5.36	10.48	0.72	154.7	3.51				13.99	0.45
J	16.50	22.2	2.724	Stromatoporoid-Red Algae-Coral	IIIMC-B4C5D2	yLS4 Strom Piece	22.2	15.5	22.351	0.75	7.00	14.00	0.15	200.0	6.60				20.60	1.00
J	13.10	23.7	2.707	Stromatoporoid-Red Algae-Coral	IIIC-C5D3	yLS3	23.7	12.2	11.077	0.48	13.87	14.50	0.20	75.0	6.00	0.11	260	6.00	26.50	1.50
J	12.30	23.6	2.719	*Cladocoropsis*	IIIMC-B4C3D1	yLS3	23.6	11.4	10.730	1.30	4.00	8.00	0.10	85.5	11.15	0.10	200	7.00	26.15	0.70
J	9.40	23.5	2.692	Skeletal Oolitic Above Sequence Boundary	IIIM-B5C3	yLS10T	23.5	8.62	9.099	0.27	38.53	25.00							25.00	0.52
J	8.99	22.1	2.722	Stromatoporoid-Red Algae-Coral	IIIMC-B4C2D1	yLS3	22.1	8.22	1.646	0.70	20.00	10.37	0.13	175.0	13.57				23.93	1.00
J	7.46	22.1	2.711	Skeletal Oolitic Above Sequence Boundary	IIIM-B5C2	yLS2	22.1	6.75	5.391	0.43	32.71	22.00	0.30	145.0	3.50				25.50	0.52
J	6.91	22.9	2.725	Stromatoporoid-Red Algae-Coral	IIIMC-B4C2	yLS2	22.9	6.21	8.708	1.05	8.00	12.50	0.06	200.0	10.50				23.00	1.30
J	5.89	22.1	2.718	*Cladocoropsis*	IIIMC-B4C2	yLS1	22.1	5.23	1.161	0.60	28.00	11.00	0.13	175.0	13.00				24.00	1.00
J	5.82	22.1	2.712	Stromatoporoid-Red Algae-Coral	IIIMC-B4C2	yLS1	22.1	5.16	1.152	0.62	30.00	12.00	0.08	190.0	12.00				24.00	1.20
J	5.02	21.3	2.706	Skeletal Oolitic Above Sequence Boundary	IIIM-B4C2	yLS2	21.3	4.39	6.089	0.45	25.00	18.56	0.52	140.0	8.00				26.56	0.80
J	3.34	18.7	2.707	*Cladocoropsis*	IIIMC-B4C3	yLS1	18.7	2.77	4.677	0.74	19.30	17.50	0.06	380.0	1.60				19.10	0.43
J	1.58	17.4	2.726	Skeletal Oolitic Above Sequence Boundary	IIIMC-B3C1	yLS1	17.4	1.06	0.942	0.19	114.00	18.67							18.67	0.70
J	1.14	14.5	2.727	Skeletal Oolitic Above Sequence Boundary	IIIMC-B3C1	yLS1	14.5	0.65	0.464	0.53	55.00	12.57	0.10	280.0	3.05				15.61	1.00
J	0.63	5.3	2.704	Bivalve-Coated Grain-Intraclast	IIIC-C2D1	nLS1	5.3	0.538	0.000	0.47	378.67	2.21	0.05	3500.0	2.09				4.30	0.61
J	0.60	10.1	2.701	Skeletal Oolitic Below Sequence Boundary	III(M-C)-B2C1	nLS1	10.1	0.495	0.086	0.36	120.00	9.10	0.36	960.0	1.00				10.10	0.75
J	0.42	10.8	2.708	Skeletal Oolitic Below Sequence Boundary	IIIC-B2C1D3	nLS3	10.8	0.338	0.051	0.28	188.31	9.33							9.33	1.90
J	0.22	9.3	2.698	Bivalve-Coated Grain-Intraclast	IIIC-C3D3	nLS3	9.3	0.166	0.005	0.18	338.48	3.90	0.17	1650.0	2.45				6.35	1.80
J	0.20	10.6	2.704	Skeletal Oolitic Below Sequence Boundary	III(M-C)-B2C2	nLS2	10.6	0.146	0.134	0.32	127.75	11.20							11.20	0.40
J	0.16	8.2	2.713	Micrite	IIIM-B4C1	nLS1	8.2	0.116	0.018	0.31	230.00	7.35							7.35	0.85
J	0.11	9.7	2.689	Bivalve-Coated Grain-Intraclast	III(F-M)-C3D1	nMS1	9.7	0.076	0.048	0.23	240.53	10.19							10.19	0.49
J	0.09	11.7	2.696	Skeletal Oolitic Above Sequence Boundary	I-B1C1	nLS1	11.7	0.01	0.140	0.39	122.52	12.46							12.46	0.50
J	0.06	6.5	2.696	Micrite	IIIF-A	nM0	6.5	0.035	0.006	0.04	1306.20	5.91							5.91	0.13
J	0.05	9.6	2.694	Micrite	(II-IIIC)-C1	nFS1	9.6	0.031	0.007	0.04	1400.00	7.26							7.26	2.00
J	0.04	7.3	2.714	Bivalve-Coated Grain-Intraclast	III(M-C)-B2	nL0	7.3	0.027	0.014	0.08	450.00	5.00	0.26	1400.0	1.30				6.30	0.90
J	0.03	7.1	2.700	Micrite	(II-IIIC)-C1	nFS1	7.1	0.013	0.002	0.05	1850.00	6.10							6.10	1.60
J	0.02	4.1	2.730	Micrite	IIIF-A	nM0	4.1	0.007	0.001	0.09	1660.49	4.12							4.12	0.16
J	0.01	4.1	2.692	Micrite	(II-IIIC)-C1	nLS1	4.1	0.003	0.000	0.03	3250.00	3.40							3.40	0.90
J	0.01	4.5	2.702	Micrite	IIIF-A	nM0	4.5	0.003	0.001	0.06	2150.22	4.18							4.18	0.16
J	0.01	4.3	2.694	Micrite	(II-IIIC)-C1	nLS1	4.3	0.002	0.000	0.06	3100.00	3.23							3.23	1.20
J	0.00	2.9	2.718	Micrite	IIIF-A	nM0	2.9	0.002	0.000	0.11	3805.47	2.78							2.78	0.60

ACKNOWLEDGEMENTS

We thank the many colleagues who have contributed to this work from the Saudi Aramco Reservoir Characterization Department and the Reservoir Management Department, from Saudi Aramco management to the Saudi Aramco core warehouse. In particular, we acknowledge John Neasham of PoroTechnologies for excellent Mercury Injection Capillary Pressure Measurements and Dave Cantrell and Abdulkader Afifi for reviews and comments. We also thank the Ministry of Petroleum for permission to publish the paper and the careful and thoughtful work of the GeoArabia reviewers and editors and constructive suggestions from Gretchen Gillis. The authors also acknowledge Richard Koepnick for encouragement. The final design of the paper by Arnold Egdane is appreciated.

REFERENCES

Ahr, W.M., D. Allen, A. Boyd, H.N. Bachman, T. Smithson, E.A. Clerke, K.B.M. Gzara, J.K. Hassall, C.R.K. Murty, H. Zubari and R. Ramamoorthy 2005. Confronting the carbonate conundrum. Oilfield Review, Spring, v. 17, no. 1, p. 18-29.

Al-Husseini, M.I. 1997. Jurassic sequence stratigraphy of the western and southern Arabian Gulf. GeoArabia, v. 2, no. 4, p. 361-382.

Amaefule, J.O., M. Altunbay, D. Tiab, D.G. Kersey and D.K. Keelan 1993. Enhanced reservoir description: Using core and log data to identify Hydraulic (Flow) Units and predict permeability in uncored intervals/wells. Presented at the 68th Annual Technical Conference and Exhibition, Houston, Texas, SPE 26436.

Archie, G.E. 1950. Introduction to petrophysics of reservoir rocks. American Association of Petroleum Geologists Bulletin, v. 34, no. 5, p. 943-961.

Bathurst, R.G.C. 1966. Boring algae, micrite envelope and lithification of molluscan biosparites. Geological Journal, v. 5, p. 15-32.

Buiting, J.J.M. 2007. Fully upscaled saturation-height functions for reservoir modeling based on Thomeer's method for analyzing capillary pressure measurements. Presented at the Middle East Oil and Gas Show, Bahrain, SPE 105139.

Buiting, J.J.M. and E.A. Clerke (in preparation). A generalized approach to permeability calculation for complex multimodal porous media.

Brunauer, S., P.H. Emmet and R. Teller 1938. The adsorption of gases in multi-molecular layers. Journal of American Chemical Society, v. 60, p. 309-316.

Cantrell, D.L. and R.M. Hagerty 1999. Microporosity in Arab Formation Carbonates, Saudi Arabia. GeoArabia, v. 4, no. 2, p. 129-154.

Cantrell, D.L. and R.M. Hagerty 2003. Reservoir rock classification, Arab-D reservoir, Ghawar Field, Saudi Arabia. GeoArabia, v. 8, no. 3, p. 435-462.

Choquette, P.W. and L.C. Pray 1970. Geological nomenclature and classification of porosity in sedimentary carbonates. American Association of Petroleum Geologists Bulletin, v. 54, no. 2, p. 207-250.

Clerke, E.A. 2003. Beyond porosity-permeability relationships: Determining pore network parameters for the Ghawar Arab-D using the Thomeer method. GeoFrontier, September, v. 1, no. 3, p. 12-17.

Clerke, E.A. 2004. Beyond porosity-permeability relationships: Determining pore network parameters for the Ghawar Arab-D using the Thomeer method. 6th Middle East Geosciences Conference, GEO 2004. GeoArabia, Abstract, v. 9, no. 1, p. 55.

Clerke, E.A. 2007. Permeability and microscopic displacement efficiency of M-1 bimodal pore systems in Arab-D Limestone. Presented at the Middle East Oil and Gas Show, Bahrain, SPE 105259.

Clerke, E.A. and P.R. Martin 2004. Thomeer Swanson excel spreadsheet and FAQ's and user comments. Presented and distributed at the SPWLA 2004 Carbonate Workshop, Noordwijk.

Clerke, E.A. and H.W. Mueller, III 2006. The Rosetta Stone Project – I: Spectral analysis of pore geometries and their relationships to depositional facies for the Arab D limestones. 7th Middle East Geosciences Conference, GEO 2006. GeoArabia, Abstract, v. 12, no. 1, p. 157.

Delfiner, P. 2007. Three statistical pitfalls of Phi-K Transforms. SPE reservoir evaluation and engineering, December, p. 609-617.

Dunham, R.J. 1962. Classification of carbonate rocks according to depositional texture. In, W.E. Ham

(Ed.), Classification of Carbonate Rocks, A Symposium. American Association of Petroleum Geologists Memoir, no. 1, p. 108-121.

Ekrann, S. 1999. Water saturation modeling: An upscaling point of view. SPE ATCE, Houston, Texas, October 3-6, SPE 56559.

Hadley, K. and J.C. Wendte 1977. Internal Aramco report.

Hagerty, R.M. and D.L. Cantrell 1990. Reservoir rock classification, Arab-D reservoir, Ghawar Field, Saudi Arabia. EPRCO, Aramco Project EPR.74PS.90 (unpublished report).

Hawkins, J.M., D.L. Luffel and T.G. Harris 1993. Capillary pressure model predicts distance to gas/water, oil/water contact. Oil and Gas Journal, January 18, p. 39-43.

Herling, D. 1968. Microporosity in carbonate rocks. In, G.M. Friedman and G. Muller (Eds.), Recent Developments in Carbonate Sedimentology-Central Europe. Springer, p. 98-105.

Leverett, M.C. 1941. Capillary behavior in porous solids. Petroleum Transactions, AIME, v. 142, p. 152-168.

Lindsay, R.F., D.L. Cantrell, G.W. Hughes, T.H. Keith, H.W. Mueller III and S.D. Russell 2006. Ghawar Arab-D reservoir: Widespread porosity in shoaling-upward carbonate cycles, Saudi Arabia. In, P.M. Harris and L.J. Weber (Eds.), Giant Hydrocarbon Reservoirs of the World: From Rocks to Reservoir Characterization and Modeling. American Association of Petroleum Geologists, Memoir 88/SEPM Miscellaneous Publication, no. 8, p. 97-137.

Lucia, F.J. 1995. Rock fabric/petrophysical classification of carbonate pore space for reservoir characterization. American Association of Petroleum Geologists Bulletin, v. 79, no. 9, p. 1275-1300.

Lucia, F.J. 1983. Petrophysical parameters estimated from visual descriptions of carbonate rocks: A field classification of carbonate pore space. Journal of Petroleum Technology, v. 35, p. 629-637.

Mitchell, J.C. 1985. Internal Aramco Report.

Mitchell, J.C., P.J. Lehmann, D.L. Cantrell, I.A. Al-Jallal and M.A.R. Al-Thagafy 1988. Lithofacies, diagenesis and depositional sequence; Arab-D Member, Ghawar field, Saudi Arabia. In, A.J. Lomando and P.M. Harris (Eds.), Giant Oil and Gas Fields - A Core Workshop. Society of Economic Paleontologists and Mineralogists, Core Workshop no. 12, p. 459-514.

Pittman, E.D. 1971. Microporosity in carbonate rocks. American Association of Petroleum Geologists Bulletin, v. 55, no. 10, p. 1873-1881.

Powers, R.W. 1968. Lexique stratigraphique international. Volume III, Asie, Fas. 10 b1, Arabia Saoudite. Centre Nationale de la Recherche Scientifique, Paris, 177 p.

Russell, S.D., R.K. Sadler, W. Weihua, P. Richter, R. Eyvazzadeh and E.A. Clerke 2004. Applications of image log analyses to reservoir characterization, Ghawar and Shaybah fields, Saudi Arabia. 6th Middle East Geosciences Conference, GEO 2004. GeoArabia, Abstract, v. 9, no. 1, p. 125.

Smith, D. 1992. How to predict down dip water level. World Oil, May, p. 85-88.

Stenger, B., T. Pham, N. Al-Afaleg and P. Lawrence 2003. Tilted original oil/water contact in the Arab-D reservoir, Ghawar field, Saudi Arabia. GeoArabia v. 8, no. 1, p. 9-42.

Swanson, B.F. 1985. Microporosity in reservoir rocks: Its measurement and influence on electrical resistivity. The Log Analyst, p. 42-52.

Thomas, E.C., R.M. Sneider, J.W. Neasham and H.J. Vinegar 1995. A catalog of petrophysical and geological properties of typical reservoir rocks. Update Published as Technical Progress Report BTC 12-95, September, Shell E&P Technology Company.

Thomeer, J.H.M. 1983. Air permeability as a function of three pore-network parameters. Journal of Petroleum Technology, April, p. 809-814.

Thomeer, J.H.M. 1960. Introduction of a pore geometrical factor defined by a capillary pressure curve. Petroleum Transactions, AIME, v. 219, T.N. 2057, p. 354-358.

Thompson, A.H., A.J. Katz and C.E. Krohn 1987. The microgeometry and transport properties of sedimentary rock. Advances in Physics, v. 36, no. 5, p. 625-694.

ABOUT THE AUTHORS

Edward A. (Ed) Clerke *is a Geological Consultant in the Geological Modelling Division/Reservoir Characterization Department of Saudi Aramco. Previously, he held the positions: Head of Petrophysics – Petrophysical Advisor for Pennzoil, Senior Principal Petrophysicist with ARCO in Plano, Texas and Petrophysical Engineering and Research Positions with Shell Oil Co. USA. Ed received his PhD in Physics from the University of Maryland in 1982 and has published articles in Log Analyst, SPE Production Engineering, Physical Review, Physica and the Journal of Physical Chemistry and received the Best Paper Award at GEO 2004 and 2006 for work presented on Arab D Limestone Pore Systems and also received the 2006 Best Paper Award at the SPWLA Carbonate Permeability Topical Conference. Less recently, Ed received the 1993 Best Paper Award from the West Texas Geological Society for work in Permian Basin carbonates. He holds five patents, four for borehole televiewer technology.*

edward.clerke@aramco.com

Harry W. Mueller III *has been a Carbonate Specialist with Saudi Aramco for seven years, most of that time in the EXPEC-ARC Department. Prior to that, he worked in a similar capacity with ExxonMobil for 26 years, much of that time working on problems in Middle-Eastern carbonate geology. He has a PhD in Geology with emphasis on carbonate stratigraphy and sedimentology from the University of Texas at Austin and a BSc in Geology from Birmingham-Southern College.*

harry.mueller@aramco.com

Eugene Craig Phillips *is presently a Petrophysicist for Saudi Aramco located in Dhahran, Saudi Arabia working in Geologic Modeling. Since 1984 he has been primarily involved in core-log integration. He was formerly with Core Laboratories working in Technical Applications Development where he concentrated on core-log integration emphasizing core calibrated log analysis models. In 1994 Eugene joined Western Atlas in the Interpretation, Research and Advanced Development group where he developed NMR log and core applications.*

eugene.phillips@aramco.com

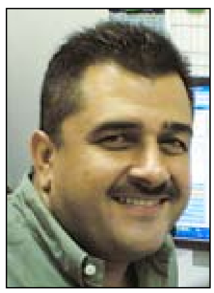

Ramsin Y. Eyvazzadeh *is a Petrophysical Specialist in the Petrophysical and Special Studies Unit, Reservoir Description Department in Saudi Aramco. Previously he has held several positions globally as Petrophysicist with Schlumberger and Numar Corporation. Ramsin has a BSc in Petroleum Engineering from the University of Southern California and a MS in Mechanical Engineering from the University of California at Berkeley.*

ramsin.eyvazzadeh@aramco.com

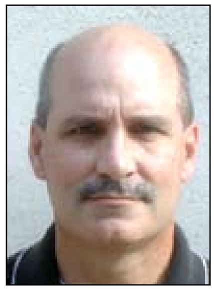

David H. Jones is a Reservoir Engineering Consultant for Quantum Reservoir Impact. He previously spent 13 years with Saudi Aramco's Reservoir Management Department. He led the multi-disciplinary GIANT project charged with developing and applying leading-edge technologies and methods to the determination of OIIP, ultimate oil recovery and the reservoir surveillance program for the Ghawar field - the largest oil field in the world. David is a recognized expert in reservoir management metrics and reservoir performance. His work in these areas led to the development of in-place systems at Saudi Aramco for tracking of all the companies' operating reservoirs. Prior to joining Saudi Aramco in 1993, David worked fifteen years at Chevron and Gulf covering a wide range of domestic and international reservoir projects. David received a BSc in Petroleum Engineering from the University of Kansas. He has participated as an invited speaker to corporate and professional forums and is the author of numerous corporate technical documents.

jones@leadingreservoirs.com

Raghu Ramamoorthy joined Schlumberger Wireline Services in 1982 and served as a Logging Engineer in Egypt and Iran, and later as a Log Analyst in Oman. He received an MSc in Petroleum Engineering from the University of Texas at Austin in 1994. He then spent an extended stint as Research Scientist (Petrophysicist) at Schlumberger-Doll Research in Ridgefield, Conn., where he worked on reservoir characterization and carbonate petrophysics. In 1997 Raghu returned to the field and served as Principal Petrophysicist in Australasia, East Asia and Saudi Arabia. Raghu is currently Petrophysics Advisor in the Schlumberger Carbonate Regional Technology Center based in Abu Dhabi.

raghu@abu-dhabi.oilfield.slb.com

Ashok Srivastava received his Bachelor of Technology in 1988 from the Indian Institute of Technology (Mumbai). He started his career in Schlumberger as a Field Engineer in 1988. Currently he is Director of Curriculum for Petrophysics for the Data and Consulting arm of Schlumberger. Prior to this he has been a Principal Petrophysicist and has worked extensively in the Middle East area. He has various publications in formation evaluation and reservoir monitoring. Ashok has two patents, one in carbonate petrophysics and another one on mathematical techniques.

asrivastava@abu-dhabi.oilfield.slb.com

Manuscript received August 25, 2006

Revised January 12, 2008

Accepted February 25, 2008

Press version proofread by authors June 23, 2008